博 士 学 位 論 文

Study on material removal mechanism
in rotary in-feed grinding

（ロータリーインフィード平面研削における
材料除去メカニズムに関する研究）

令和 3 年度 3 月

茨城大学大学院理工学研究科

複雑系システム専攻

陸　文通

Abstract

Rotary in-feed grinding is a most promising process with high efficiency, precision and controllability of wafer geometry including the thickness and flatness and thus has been widely used in manufacturing of monocrystal wafers, such as silicon, silicon carbide, sapphire, lithium tantalate and etc. In order to deeply understand the material removal mechanism in rotary in-feed grinding, the objectives of this research are:

1. Theoretical and experimental investigations on the wafer profile generation.

2. Theoretical and experimental investigations on the wafer topography generation.

3. Theoretical and experimental investigations on the grinding force and heat assessments.

The thesis consists of the following contents:

In Chapter 1, monocrystalline materials are briefly introduced together with their applications and manufacturing processes. The conventional manufacturing process such as lapping and polishing using free abrasive is no longer able to meet the requirements in cost, productivity and accuracy. The fixed abrasive process (or grinding) stands out as a most promising manufacturing technology to replace the conventional processes.

The rotary in-feed grinding dynamic originated for wafering process is relatively new and totally different from that of conventional grinding. This thesis provides a deeper insight view of mechanism of rotary in-feed grinding, from engineering perspectives of 1) wafer profile and geometry, 2) chip formation and wafer surface topography and 3) grinding statics and dynamics.

A detailed survey on the monocrystalline wafering process has been made in chapter 2. From accessible literature works, it is revealed that most of published researches are focusing on the three specific scoops including the total thickness variation (TTV), surface integrity and subsurface damage to evaluate the performance of rotary in-feed grinding. When the dynamics of rotary in-feed grinding is concerned, the grinding performances should be

assessed from the following aspects: (1) Kinematics and path control of each cutting edge which govern the wafer shape and profile; (2) Chip formation and protrusion distribution of cutting edge which govern the surface topography and integrity; (3) Grinding force and grinding heat which dominate the subsurface damage. Therefore, a full understanding of rotary in-feed grinding mechanisms become more essential.

The mathematical analysis and experiments for wafer profile generation are described in chapter 3, to obtain and optimize the grinding conditions for achieving great wafer geometry. First, the motion and path of cutting edge in rotary in-feed grinding are kinematically analyzed in three-dimensions, to address the behavior of each abrasive in generation of the wafer profile. The results mathematically reveal the effects of wheel specifications, grinding conditions and wheel/wafer configurations on the wafer geometry, particularly including offset distance between the axes of wheel and wafer, the tilt angles of wafer axis and the diameter of the wheel. Second, the effects of both cutting path density and machine stiffness on the wafer profile are assessed. The experimental results in Si wafer grinding demonstrate a solution using tilt angle to counterbalance the effects of machine stiffness and cutting path density on the wafer geometry.

In Chapter 4, the surface topography on the wafer surface is associated with the chip formation which highly depends on distribution of abrasive protrusion in height-wise. Both theoretical analysis and experiments results lead to a fact that the surface roughness becomes larger toward to the outer circumference of the wafer, but smaller as decreasing in the rotational speed ratio. In addition, influence of depth of cut has also been investigated. The mathematical analysis results suggest that inadequate depth of cut may not improve the surface roughness in rotary in-feed grinding due to the insufficient effective cutting edge involved in material removal.

The statics and dynamics in rotary in-feed grinding have been studied and discussed in chapter 5, in order to associate not only the grinding conditions but also the wheel specifications with the grinding force, grinding power and grinding heat. The grinding force exerted on an individual abrasive is first correlated to the chip cross section, and then extended to the grinding force on a single wheel segment and whole wafer. Meanwhile, a wireless thermo/dynamo-meter is designed, developed and applied to measure the grinding

force and grinding temperature simultaneously during the grinding process. Both theoretical analysis and experiment results tell that the grinding force on a wheel segment was proportional to the segment length, gradually grew along the wafer radial distance and rapidly dropped to zero when the wheel segment exited from the wafer fringe. Grinding force and consumed grinding power are proportional to the square of the wafer size. This fact suggests that grinding large diameter wafers requires high rigidity and the spindle power of the grinding machine.

Chapter 6 makes the summary of the achievements obtained in this study.

Contents

Chapter 1 Introduction

1.1 Introduction of functional monocrystal materials and their applications

A single-crystal or monocrystalline material is a crystal lattice that repeats itself periodically in three dimensions, with no grain boundaries [1]. It is the building block of the crystalline structure which displays translational symmetry along its principal axes [2]. Thus, the crystalline structure and symmetry of monocrystalline material play a critical role in determining unique physical properties in piezo-electrics, pyroelectrics and optics, which can also be anisotropic [3-5]. Such properties make the monocrystalline materials be widely
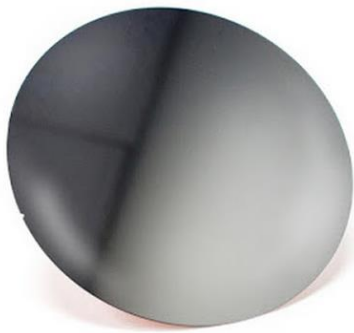
(a) Silicon
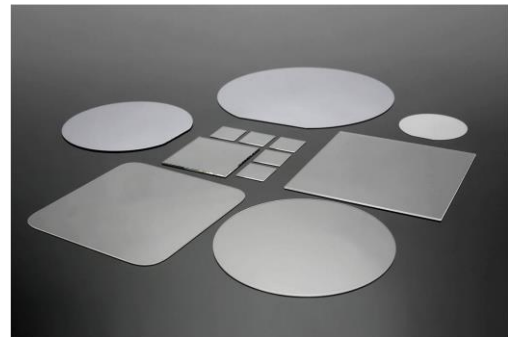
(b) Sapphire
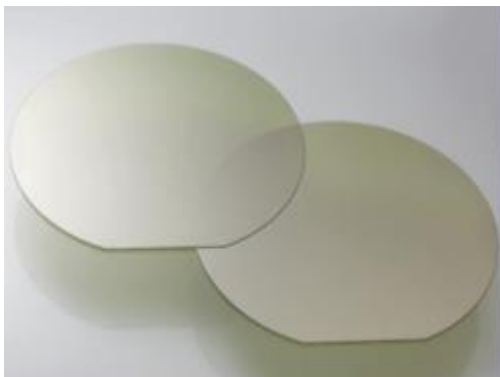
(c) Silicon carbide

(d) Lithium tantalate

Fig. 1.1 Functional monocrystal materials

utilized in numerous functional devices [1-5].

The monocrystalline materials, such as silicon (Si), sapphire (α-Al$_2$O$_3$), silicon carbide (SiC) and lithium tantalate (LiTaO$_3$) are frequently used in high-end semiconductor devices [6-9]. Most of those devices in our daily lives are built on the substrates or wafers of those monocrystalline materials as shown in Fig. 1.1 [10-13]. Crys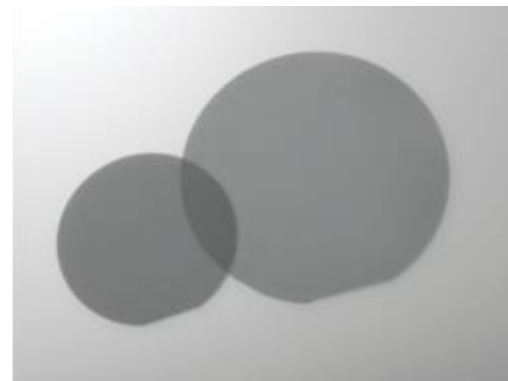talline silicon not only is one of the best-studied monocrystalline materials, but also is the dominant semiconductor materials in modern microelectronics. Thus, silicon substrate is mainly used for the integrated circuits in various potential applications, such as flash memory as shown in Fig. 1.2 (a) [14]. With excellent optical properties, sapphire substrate is mainly used for the growth of GaN epilayer in LEDs application, as shown in Fig. 1.2 (b) [15]. Silicon carbide substrate is unusually used in insulated-gate bipolar transistor (IGBT) for high power semiconductor devices, as shown in Fig. 1.2 (c) [16]. Shown in the Fig. 1.2 (d) [17] is configuration of pyroelectric sensor which transforms heat into electric potential by using of
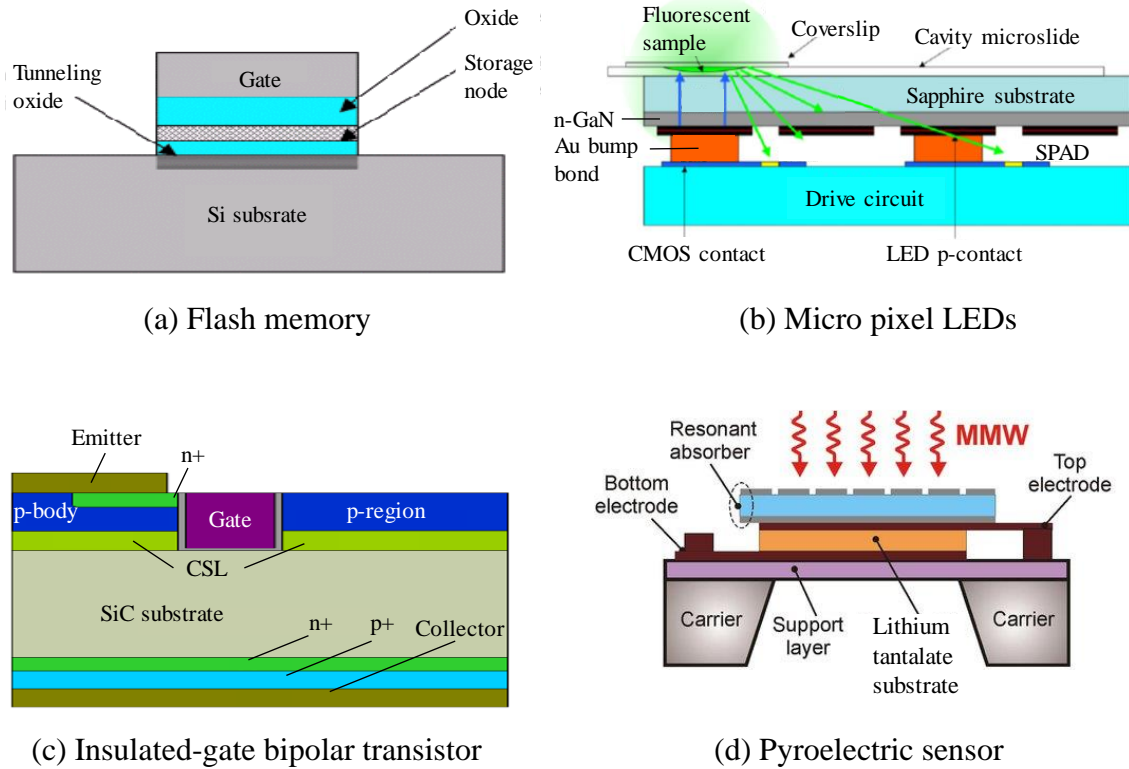

(a) Flash memory

(b) Micro pixel LEDs

(c) Insulated-gate bipolar transistor

(d) Pyroelectric sensor

Fig. 1.2 Application of functional materials

the pyroelectric effects of lithium tantalate substrate.

1.2 Wafer manufacturing processes

Before a semiconductor is built, the monocrystalline materials must be turned into a wafer substrate. Fig. 1.3 shows the traditional manufacturing flow of wafer substrate [6]. The manufacturing procedure of wafer substrate starts with the growth of a crystal ingot via the Czochralski (CZ) method [18]. In the CZ method, nuggets of polycrystalline are placed in a quartz crucible, which is set in a graphite crucible surrounded by graphite heaters in the crystal pulling chamber. These nuggets are melted by heating in an argon atmosphere under vacuum and then pulled slowly using a seed crystal. Once the ingot is fully-grown, the ingot has a notch or flat cut into it, in order to indicate its orientation. The ingot is then sliced into thin disc-shaped wafers with hard grain edge wire-saw. The lapping process begins after the thin disc-shaped wafers was obtained by slicing process. The wafers are set in a carrier, which spins between two rotating lapping plates. Both of wafer surfaces are lapped to remove saw marks and surface defects by use of the loose abrasive slurry in general. It is
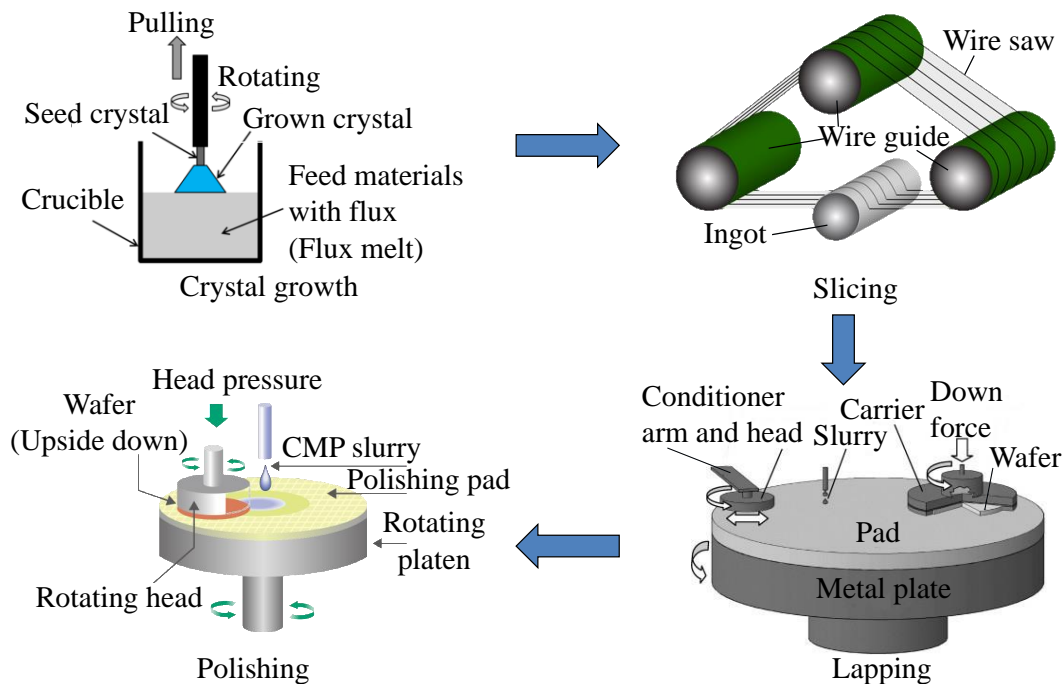

Fig. 1.3 Conventional processes for wafer manufacturing

3

also the popular process to thin the wafer and relieve stress accumulated during the slicing process [19]. Finally, the wafer is concerted to a damage free, specular surface by the polishing processes. With free abrasive methods, it is feasible to obtain better surface roughness only when smaller abrasives are utilized, and thus multiple equipments are required [20]. In addition, the process efficiency is extremely low when thinning hard and brittle materials such as monocrystal silicon, silicon carbide and sapphire by using the free abrasives [21]. Lapping and polishing with free abrasive to obtain the ultra-smooth and damage-free wafer surface account for about 80% of total cost in manufacturing process of monocrystalline wafers. The semiconductor industry requires to reduce the manufacturing cost of wafer thinning while meeting more stringent specifications since the demand of the wafer substrate is increasing year-over-year [21].

Nowadays, instead of the conventional manufacture flow using the loose abrasive, new sequence of wafer processes, Rotary in-feed Grinding and Chemo-Mechanical Grinding, are intensively researched [22, 23]. In the new processes as shown in Fig. 1.4, the surface of sliced substrate wafer is trimmed by coalescent diamond grinding and followed by chemo-mechanical grinding for finishing. Both processes use fixed abrasive wheels which are agglomerated into a solid-state or organic composite. In other words, the abrasives are bonded together by a bonding material to form a fixed abrasive cutting tool. The composite of fixed abrasives is manufactured into the shape of segment mounted on a cup-type wheel. If the grinding conditions are chosen appropriately, a self-dressing process will spontaneously occur during grinding process and significantly improved the cutting tool life [22].

The cup-type grinding wheel is down fed to the wafer with a constant in-feed rate while
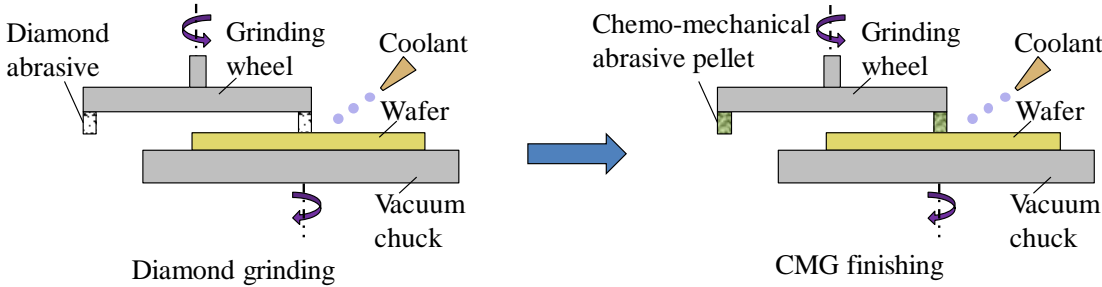

Fig. 1.4 New fixed abrasive processes; grinding and CMG

4

both grinding wheel and wafer rotate around their own axes simultaneously during the rotary in-feed grinding process. The fixed abrasive process provides the higher material removal rate (MRR) [24, 25]. In addition, the grinding wheel segment is in constant contact with the monocrystal wafer from the center to periphery and thereby to deliver a stable grinding performance. These characteristics make it capable of generating a flat surface with high accuracy and high surface integrity in a cost-effective way [21]. Thus, the fixed abrasive process is widely applied in monocrystal wafers manufacturing. When compared with loose abrasive process, the fixed abrasive process is becoming increasingly seductive because it not only is a controllable process but also has various nonnegligible advantages as listed in Table 1.1.
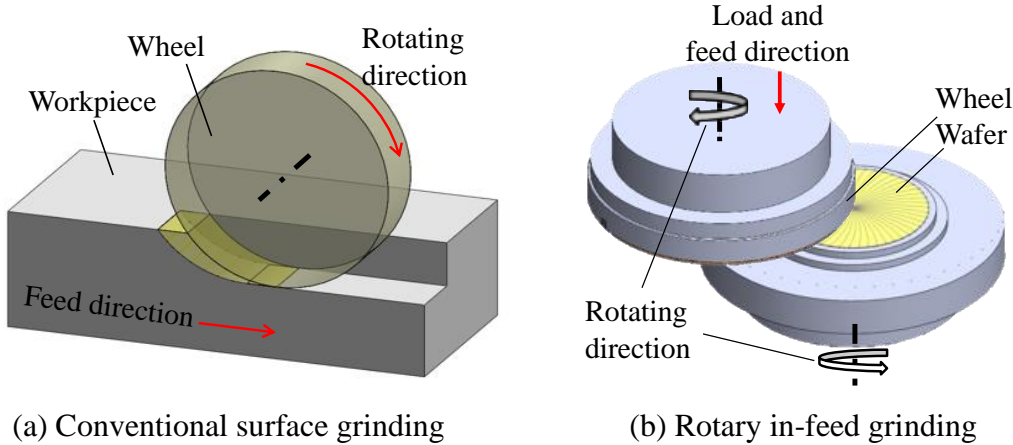
(a) Conventional surface grinding   (b) Rotary in-feed grinding

Fig. 1.5 Conventional surface grinding and rotary in-feed surface grinding

Table 1.1 The advantages of fixed abrasive processes

	Loose abrasive processes	Fixed abrasive processes
Cost	High	Low
Time consuming	High	Low
Environmental-friendly	Bad	Good
Geometry controllability	Low	High
Material removal rate	Low	High

Table 1.2 The differences between conventional grinding and rotary in-feed grinding

	Rotary in-feed grinding	Conventional surface grinding	
Equivalent wheel diameter	∞	$10^2 \sim 10^3$	[mm]
Abrasive cutting depth	$10^{-4} \sim 10^{-1}$	$10^0 \sim 10^2$	[μm]
Abrasive cutting length	$10^2 \sim$	$\sim 10^{-1}$	[mm]
Wheel/workpiece contact curvature different	0	10^{-2}	[mm^{-1}]
Cutting path density	Dense → Sparse (Center → Periphery)	Uniform	—

Surface grinding, in general, is a very complex material removal operation and thus several types of grinding dynamics have been developed to produce the corresponding products [19]. Fig. 1.5 shows the two types of surface grinding mechanism which are (a) conventional surface grinding and (b) rotary in-feed grinding. Over the past decades, many works concerning with the grinding process have been done to understand the metal material removal mechanism in conventional surface grinding process [26-28]. On the other hand, the dynamics of rotary in-feed grinding is relatively new and total different from that of the conventional surface grinding [29]. For clearly understanding the differences between rotary in-feed grinding and conventional surface grinding, the comparison of these two types of surface grinding is listed in Table 1.2.

In this thesis, the focus will be given to understand the removal mechanism in rotary in-feed grinding.

1.3 Research objectives

The distinct advantages of rotary in-feed grinding have made it become an attractive pre-finishing process for wafer manufacturing. It is the most promising process to ensure the

controllability of wafer thickness and flatness, and thus widely used to manufacture the monocrystal wafers. Hence, the complex material removal mechanism of rotary in-feed grinding needs to be studied clearly and deeply to improve the grinding performance. The objectives of this research are listed as below:

1. Theoretical analysis and experiments on the wafer total thickness variation by concerning the cutting path in 3D manner, and optimization of grinding conditions to produce the excellent flatness on wafers.

2. Theoretical analysis and experiments on the wafer surface integrity by considering the distribution of abrasive protrusion height-wise, and optimization of grinding conditions to generate the low and stable surface roughness.

3. Theoretical analysis and experiments on the grinding force and heat by correlation to the chip formation, and optimization of grinding conditions to reduce the surface and subsurface damage.

1.4 Thesis structure and strategy

In thesis, focusing on the material removal mechanism in rotary in-feed grinding process, the structure and strategy of this thesis are listed as below:

In Chapter 1, monocrystalline materials are briefly introduced together with their applications and manufacturing processes. The conventional manufacturing process such as lapping and polishing using free abrasive is no longer able to meet the requirements in cost, productivity and accuracy. The fixed abrasive process (or grinding) stands out as a most promising manufacturing technology to replace the conventional processes.

The rotary in-feed grinding dynamic originated for wafering process is relatively new and totally different from that of conventional grinding. This thesis provides a deeper insight view of mechanism of rotary in-feed grinding, from engineering perspectives of 1) wafer profile and geometry, 2) chip formation and wafer surface topography and 3) grinding statics and dynamics.

A detailed survey on the monocrystalline wafering process has been made in chapter 2.

From accessible literature works, it is revealed that most of published researches are focusing on the three specific scoops including the total thickness variation (TTV), surface integrity and subsurface damage to evaluate the performance of rotary in-feed grinding. When the dynamics of rotary in-feed grinding is concerned, the grinding performances should be assessed from the following aspects: (1) Kinematics and path control of each cutting edge which govern the wafer shape and profile; (2) Chip formation and protrusion distribution of cutting edge which govern the surface topography and integrity; (3) Grinding force and grinding heat which dominate the subsurface damage. Therefore, a full understanding of rotary in-feed grinding mechanisms become more essential.

The mathematical analysis and experiments for wafer profile generation are described in chapter 3, to obtain and optimize the grinding conditions for achieving great wafer geometry. First, the motion and path of cutting edge in rotary in-feed grinding are kinematically analyzed in three-dimensions, to address the behavior of each abrasive in generation of the wafer profile. The results mathematically reveal the effects of wheel specifications, grinding conditions and wheel/wafer configurations on the wafer geometry, particularly including offset distance between the axes of wheel and wafer, the tilt angles of wafer axis and the diameter of the wheel. Second, the effects of both cutting path density and machine stiffness on the wafer profile are assessed. The experimental results in Si wafer grinding demonstrate a solution using tilt angle to counterbalance the effects of machine stiffness and cutting path density on the wafer geometry.

In Chapter 4, the surface topography on the wafer surface is associated with the chip formation which highly depends on distribution of abrasive protrusion in height-wise. Both theoretical analysis and experiments results lead to a fact that the surface roughness becomes larger toward to the outer circumference of the wafer, but smaller as decreasing in the rotational speed ratio. In addition, influence of depth of cut has also been investigated. The mathematical analysis results suggest that inadequate depth of cut may not improve the surface roughness in rotary in-feed grinding due to the insufficient effective cutting edge involved in material removal.

The statics and dynamics in rotary in-feed grinding have been studied and discussed in chapter 5, in order to associate not only the grinding conditions but also the wheel

specifications with the grinding force, grinding power and grinding heat. The grinding force exerted on an individual abrasive is first correlated to the chip cross section, and then extended to the grinding force on a single wheel segment and whole wafer. Meanwhile, a wireless thermo/dynamo-meter is designed, developed and applied to measure the grinding force and grinding temperature simultaneously during the grinding process. Both theoretical analysis and experiment results tell that the grinding force on a wheel segment was proportional to the segment length, gradually grew along the wafer radial distance and rapidly dropped to zero when the wheel segment exited from the wafer fringe. Grinding force and consumed grinding power are proportional to the square of the wafer size. This fact suggests that grinding large diameter wafers requires high rigidity and the spindle power of the grinding machine.

Chapter 6 makes the summary of the achievements obtained in this study.

Reference

[1]   Gregory S. Rohrer, (2001), Structure and bonding in crystalline materials, Cambridge University Press.

[2]   Suwas S., Ray R., (2014), Crystallographic texture of materials, Springer–Verlag London.

[3]   Oana C., Benoit R.B., Nitin C., (2019) Plasticity-Danmage Couplings: From single crystal to polycrystalline materials, Springer.

[4]   Ye, Zuo Guange, (2008), Handbook of advanced dielectric, piezoelectric and ferroelectric materials, Woodhead Publishing Limited.

[5]   Safa K., Peter C., (2017), Handbook of electronic and photonic materials, Springer.

[6]   O'Mara W.C., Herring R.B., Hunt L.P., (1990), Handbook of semiconductor silicon technology, Noyes Publications.

[7]   Pishchik, V., Lytvynov, L.A., Dobrovinskaya, E.R. (2009), Material, Manufacturing, Applications, Springer.

[8]   Choyke W.J., Matsunami H., Pensl G., (1971), Silicon carbide, Springer.

[9]   Milek J.T., Neuberger M., (1972), Linear electrooptic modular materials, Plenum Press.

[10]   Information on: https://www.matterhackers.com/store/printer-accessories/silicon-wafer-print-bed-plate-200mm

[11]   Information on: https://www.indiamart.com/proddetail/sapphire-wafer-10205730448.html

[12]   Information on: https://www.ii-vi.com/product/sic-substrates/

[13]   Information on: https://www.koike-corp.co.jp/en/product

[14]   Cho, I., Park, B., Lee, J., Lee, J., (2003), Nano-scale SONOS memory with a double-gate MOSFET structure, Journal Korean physical society, Vol. 42, pp. 233-236.

[15]   Rae B.R., Griffin C., McKendry J., Girkin J.M., Zhang H.X., Gu E., Renshaw D., Charbon E., Dawson M.D. and Henderson R.K., (2008), CMOS Driven Micro-pixel LEDs Integrated with Single Photon Avalanche Diodes for Time Resolved Fluorescence Measurements, Journal of physics D: Applied physics, Vol. 41, No. 9, pp. 094011.

[16]   Wei J., Zhang M., Jiang H., To S., Kim S., Kim J., Chen K., (2018), SiC trench IGBT with diode-clamped p-shield for oxide protection and enhanced conductivity modulation, IEEE 30th International Symposium on Power Semiconductor Devices and ICs (ISPSD), pp. 411-414.

[17]   Sergei A.K., Andrey G.P., Miguel N.C., Andrey V. A., (2016), Selective pyroelectric detection of millimeter waves using ultra-thin metasurface absorbers, Scientific reports, 6, 21079.

[18]   Information on: https://en.wikipedia.org/wiki/Czochralski_method

[19]   King R.I., Hahn R.S., (1986), Handbook of modern grinding technology, Chapman and Hall.

[20]   Marinescu I.D., Uhlmann E., Doi T.K., (2006), Handbook of lapping and polishing, CRC Press.

[21]   Pei Z.J., Fisher G.R. and Liu J., (2008), Grinding of silicon wafers: A review from historical perspectives, International journal of machine tools & manufacture, Vol. 48, No. 12-13, pp.1297-1307.

[22]   Marinescu I.D., Doi T.K., Uhlmann E., (2015), Handbook of ceramics grinding and polishing, Elsevier.

[23]   Tomita Y., Eda H., (1996), A study of the ultra precision grinding process on a magnetic disk substrate-development of new bonding materials for fixed abrasives of grinding stone, Wear, Vol. 195, No. 1-2, pp. 74-80.

[24]   Jahanmir S., Ramulu M., Koshy P., (1999), Machining of ceramics and composites, New York.

[25]   Zhang B., Howes T.D., (1994), Material-Removal Mechanisms in Grinding ceramics, Annals of the CIRP, Vol. 43, No. 1, 305-308.

[26]   Younis M.A., Alawi H., (1984), Probabilistic analysis of the surface grinding process, Vol. 8, No. 4, 208-213.

[27]   Syoji K., (2004), Grinding engineering, Yokendo co. ltd, (in Japanese).

[28]   Ariura Y, Suzuki T, Onikura H, Semba T, Kurokawa S., (2007), Manufacturing Process II, Asakura Publishing Co., Ltd. (in Japanese).

[29]   Shaw M.C., (1996), Principles of abrasive processing, Oxford.

Chapter 2 Literature review on wafer process in rotary in-feed grinding

Conventionally, the monocrystalline wafers were manufactured by the face grinding or creep feed face grinding dynamics. In 1986, the first rotary in-feed grinding machine was developed in Japan by Nishiguchi M., Sekiguchi T., Miyoshi I., and Nishio K. for monocrystalline wafer back-grinding [1]. After Matsui S. [2] presented a wafer rotation grinding method in 1987 and reported that this dynamics provides better performance in wafer flatness, surface roughness and flatness of ground surface, a lot of efforts have then been invested to study the mechanism of the rotary in-feed grinding [3, 4]. Several investigations showed that the rotary in-feed grinding was capable of producing the better total thickness variation (TTV), consistent and low grinding force which helps to limit the subsurface damage and maintain a desired shape for ground wafers [2-4]. Therefore, the rotaty in-feed grinding becomes the most promising process and thus is successfully and widely utilized in the fabrication of monocrystalline wafers.

This chapter will present a general literature review of the rotary in-feed grinding for monocrystalline wafering process by focusing on three specific scoops: wafer geometry control, wafer surface integrity and wafer subsurface damage (SSD). When the dynamics of rotary in-feed grinding is concerned, the grinding performances could be mainly evaluated as below:

- Kinematics and path of each cutting edge which govern the wafer shape and profile.

- Chip formation and protrusion distribution of cutting edge which govern the surface topography and integrity.

- Grinding force and grinding heat which dominate the subsurface damage.

2.1 Wafer shape and profile

In general, the grinding is a fixed abrasive machining operation for heavy stock removal [5]. A common dynamic of the conventional rotary face grinding is shown in left panel of Fig. 2.1. The grinding wheel is self-rotating while the worktable traverses in horizontal reciprocally and the grinding wheel is fed vertically downward into the wafer. The engagement of the grinding wheel against the wafer is shown in right panel of Fig. 2.1. The contact length and edge angle keep changing during the wafer traveling. Due to changes in the contact length and angle, the grinding forces vary, which makes it difficult to generate a flat surface.

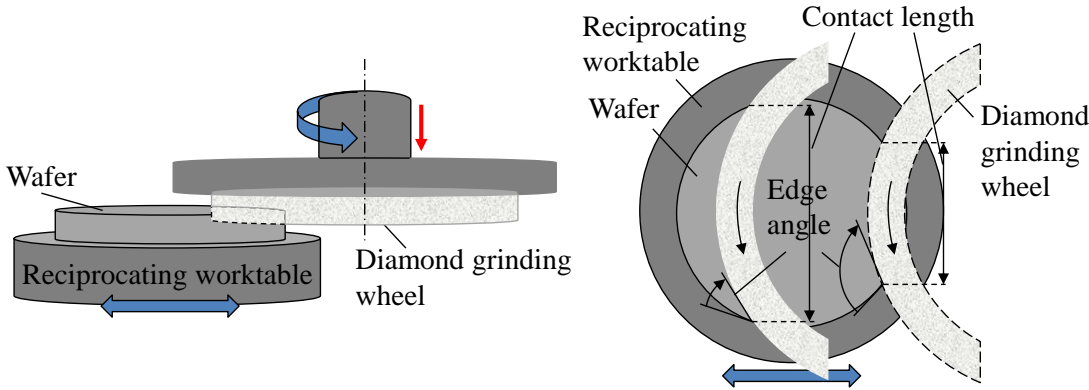In 1987, Matsui [2] has first reported the rotary in-feed grinding dynamics which

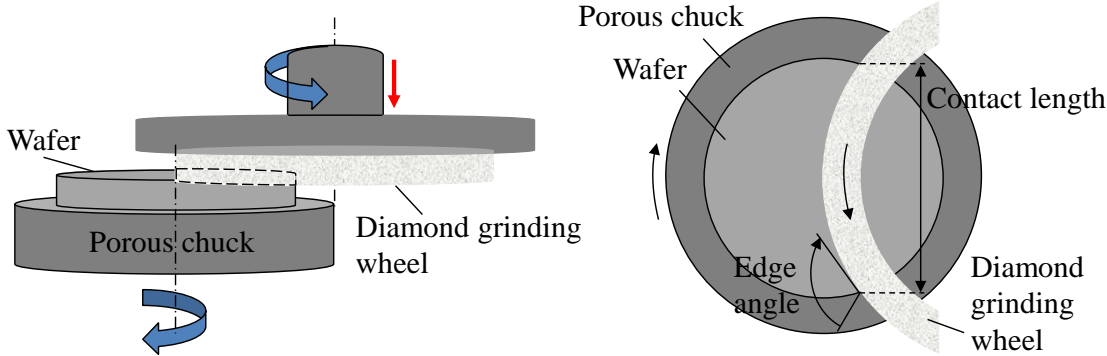Fig. 2.1 Conventional rotary face grinding dynamics

Fig. 2.2 Rotary in-feed grinding dynamics

13

generated a better wafer flatness. Fig. 2.2 illustrates the configuration of rotary in-feed grinding process. The wafer is mounted on a porous chuck and held by vacuum. The grinding wheel is offset by a distance of the wheel radius relative to the wafer rotation axis. The grinding wheel and wafer simultaneous rotate around their own axis while the grinding wheel is fed into the wafer during the grinding. Compared with conventional face grinding method, the contact length and edge angle are kept constant in rotary in-feed grinding process. Such in-feed grinding dynamics can deliver a much stable grinding performance throughout the grinding process. Thus, rotary in-feed grinding is widely applied into wafer back-grinding and wafer thinning where the flatness and profile accuracy of the wafer are critical.

In rotary in-feed grinding, the shape of the ceramic chuck is built with a very small angle in rotary in-feed grinding machine, as shown in Fig. 2.3 [6]. The wafer elastically deforms into the conic shape when the it is mounted on the chuck. Pei et al. in 1999 reported that the shape of the ground wafer can be controlled by adjusting the tilt angle between the wheel rotation axis and wafer rotation axis [7]. Tso and Teng in 2001 stated that the deviation of wheel spindle angle must be justified in order to obtain the best flatness of the ground wafer [8]. Via the kinematic analysis and experiments, the research shown that the inclination of grinding wheel axis must be set appropriately to improve the TTV. In the 2002, Zhou et al. developed an advanced manufacturing system for $\phi 300$ [mm] silicon wafer and kinematical analysis on wafer profiles has been made by changing the combination of tilt angles of wheel rotational axis and wafer rotational axis in 2D manner [9, 10]. They took one step further in 2003, addressed the cutting path of individual abrasive in 3D manner and effect on the wafer flatness [11]. This is a quite specific 3D kinematical analysis model which is able to address
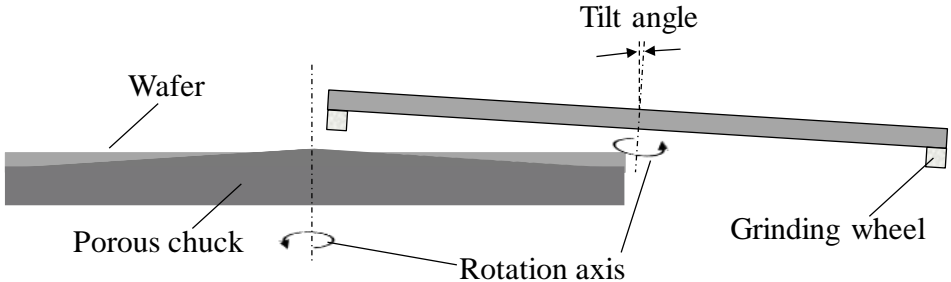

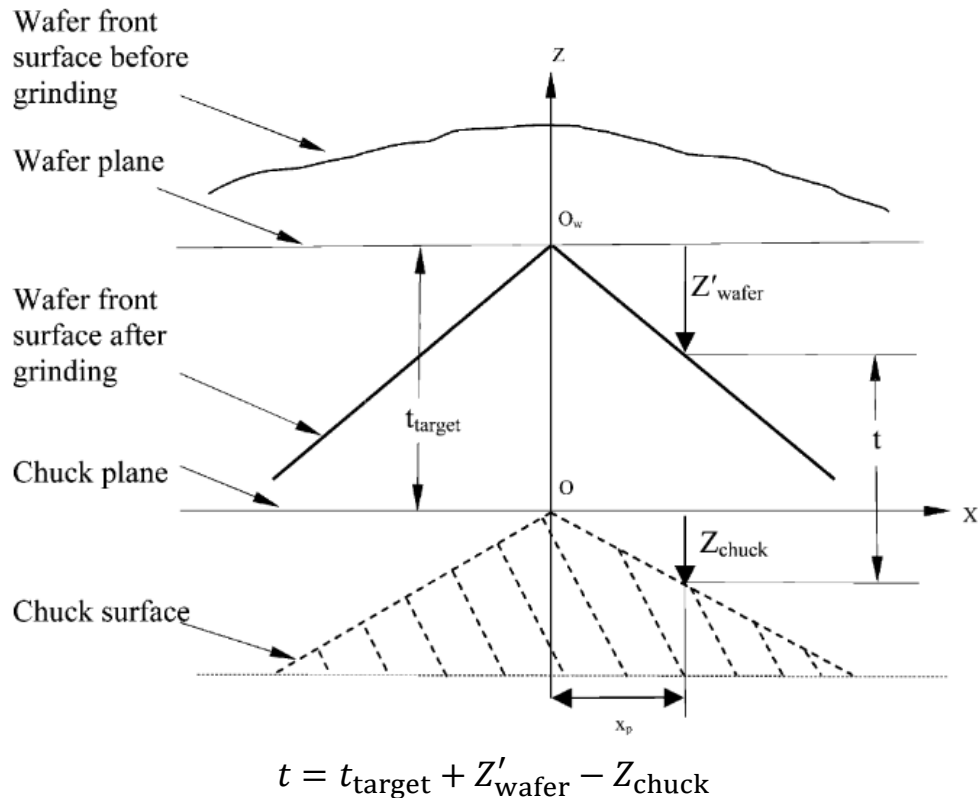Fig. 2.3 Wafer profile and tilt angle

Fig. 2.4 Illustration for wafer profile generation [12]

$$t = t_{\text{target}} + Z'_{\text{wafer}} - Z_{\text{chuck}}$$

the behavior of each abrasive in wafer profile generation. Sun et al. proposed a mathematical model for the wafer profile generation [12]. The results shown that the chuck shape significantly influenced on the wafer shape, as illustrated in Fig. 2.4. As a follow-up report, Sun et al. proposed the machine configurations for the spindle axis adjustments. An important criterion was given to tilt the wheel rotation axis relative to the wafer rotation axis. The experiment results were released in publication [13] and shown in Fig. 2.5 (a) and (b). Zhang et al. reviewed the hypothesis for the generation mechanisms of central dimples due to the deformation occurring in the contact zone where the grinding wheel segment engages into wafer during grinding [14]. Via the kinematic analysis and experiments, Zhou et al. stated that the machine tool with higher stiffness and grinding conditions providing denser cutting path offer a better TTV [15, 16]. A grinding machine with high loop stiffness has been developed by Kusuyama et al. [17] and a rotary worktable with constant-flow hydrostatic water bearing by Okahata G., et al. [18] for 450 [mm] silicon wafers. They

15
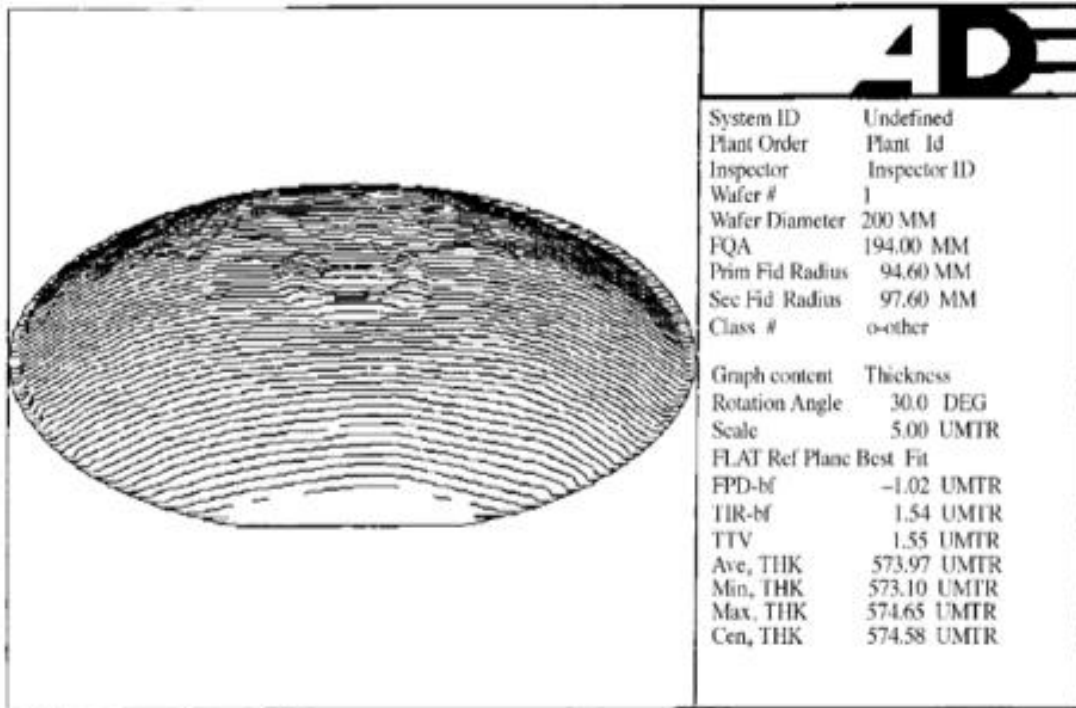
(a)
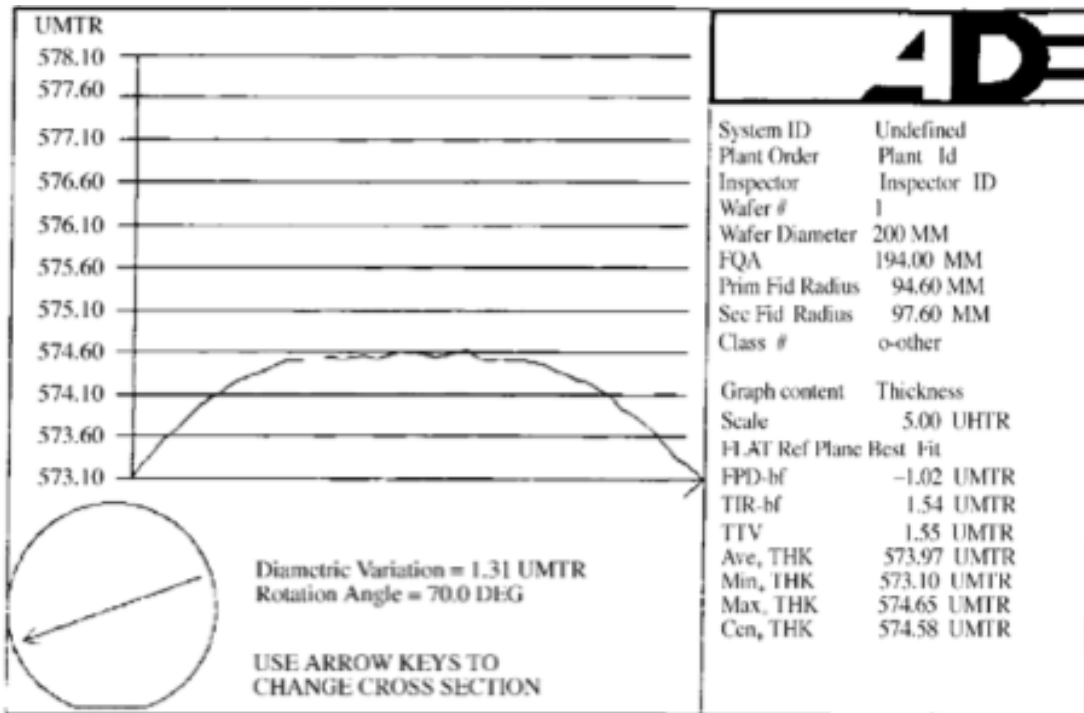
(b)

Fig. 2.5 Concave wafer profile (a) 3D graph; (b) 2D cross-sectional profile [13]
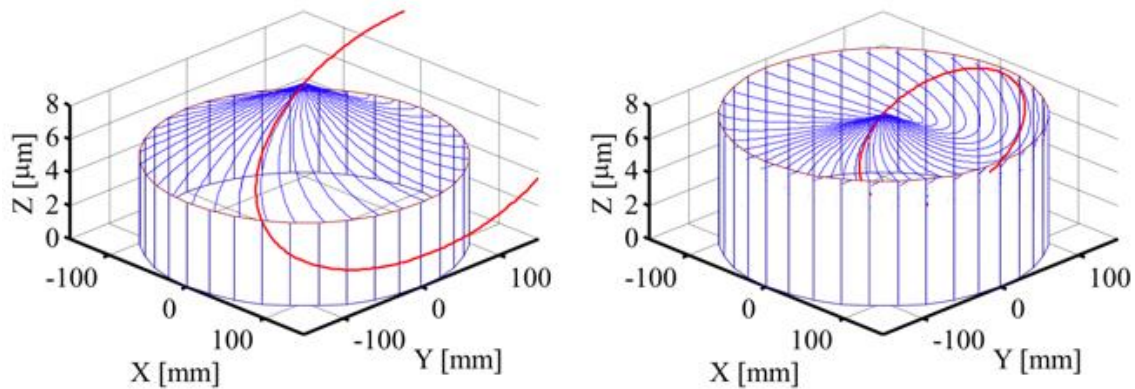
Fig. 2.6 Wafer shape produced by different wheel diameters [19]

claimed that the developed rotary in-feed grinding machine has sufficient static performances for the large scale silicon-wafer grinding. A recent study [19] also presented that the grinding wheel diameter influenced on the wafer profile, as shown in Fig. 2.6. A concentric zone was formed on the wafer when the wheel diameter is equal to the wafer radius.

According to the literature mentioned above, the grinding machine configuration and grinding conditions significantly influence on ground wafer shape and profile.

1) The tilt angle between grinding wheel rotation axis and wafer rotation axis is the main concern to the total thickness variation of ground wafers. By setting the appropriate inclination of grinding wheel rotation axis and wafer rotation axis, the TTV could be improved.

2) The kinematic analysis is able to address the wafer shape affected by wheel specifications and grinding conditions. It also provides a useful guidance for selection of grinding conditions for flat wafer manufacturing.

In order to associate the grinding conditions with the wafer shape and profile, kinematic and geometric study on rotary in-feed grinding is necessary. In chapter 3, a mathematical analysis and experiments are described as a guidance to obtain and optimize the grinding conditions for high wafer geometry.

17

2.2 Surface integrity

When compared with conventional face grinding process, rotary in-feed grinding process is becoming more and more attractive since it could generate the better surface integrity [20], due to its constant contact zone and stable grinding performance.

The surface integrity is the main cause to lead to low productivity in subsequent finishing process [21]. With increasing demand of high-quality wafers, the ductile mode machining with crack-free surface is a "must" for rotary in-feed grinding [22]. The surface roughness is a component of surface texture, and generally used to assess the surface integrity. Regrading to the surface roughness, Matsui presented an experimental result of surface roughness of ground wafer which showed that the surface roughness by the rotary in-feed grinding is better than that by the conventional face grinding and the creep-feed grinding, but co-related to the wafer radial distance. The experiment conditions are detailed listed in Table 2.1, and the part of results released in publication [2] was shown in Fig. 2.7. Tomita and Eda

Table 2.1 Experiment conditions in publication [2]

	Wafer rotation grinding (Rotary in-feed grinding)	Face grinding	
		Creep feed	Conventional
Workpiece	Silicon wafer, $\phi100, 10$ [mm]		
Grinding wheel	$\phi200$ Cup wheel, SD1200R100B		
Wheel speed	3000 [min^{-1}] (1884 [m/min])		
Table rotation speed	1000 [min^{-1}]	–	–
Table speed	–	200 [mm/min]	6 [m/min]
In-feed rate	0.1 [mm/min]	–	–
Depth of cut	(0.1 [μm/rev])	10 [μm]	1 [μm]
Grinding allowance	20 [μm]		
Coolant	Water		

developed a fixed abrasive grinding wheel for producing high quality surface on a magnetic disk substrate [3]. They showed that the roughness is affected by the size of the fixed abrasives. Pei et al. stated that both wafer rotational speed and in-feed rate significantly influenced on surface roughness [23]. Luo and Chen via an experiment demonstrated the effects of abrasive size and wheel rotational speed on surface roughness [24]. Liu et al. also presented a comprehensive kinematic simulation to study the effects of different abrasive shapes and dressing on the surface roughness [25]. Sun et al. considered the effects of wheel rotational speed and wafer rotational speed on the depth of the grinding grooves [26].

Since year 1986, intensive attentions have been paid to the rotary in-feed grinding process of monocrystalline wafer. Most of the literature works showed the relationship between the variables (including rotational speed ratio, wafer radial, in-feed rate, abrasive size and shape) and surface roughness via experiment at studies. However, theoretical prediction of surface roughness in rotary in-feed grinding is still under research because of its complexity. Therefore, a mathematical analyzation of surface roughness for deeper understanding to the rotary in-feed grinding process of monocrystalline wafer is necessary. The detailed study on
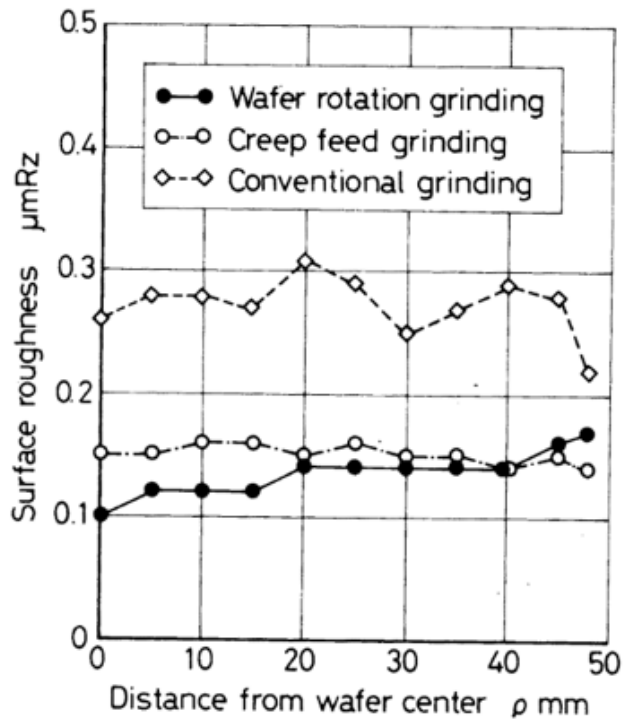

Fig. 2.7 Surface roughness along the wafer radial distance [2]

19

chip formation and resultant wafer surface roughness will be presented in chapter 4, by taking into the consideration of protrusion of each cutting edge in height-wise.

2.3 Subsurface damage

Finishing with SSD (subsurface damage) free is required for most wafer manufacturing [27]. Therefore, it is essential to achieve SSD as less as possible in rotary in-feed grinding, to reduce the process time and cost in the subsequent polishing process.

For the above purpose, numerous researches have been made from the viewpoints of optimizing grinding wheel specifications, grinding conditions according to wafer properties. Zhang and Howes proposed a model for predicting grinding induced SSD, in which damage depth is a function of brittleness of materials and the maximum abrasive depth of cut [28]. Lundt et al. stated that grinding of silicon wafer would cause unavoidable SSD [29]. Pei et al. investigated that the effects of abrasive size and sample position on the depth of SSD. Through the way of cross-sectional examination, they found that the depth of subsurface crack on ground silicon wafers is approximately equal to half of the diamond abrasive size used in grinding wheel [7]. Gao et al. also found quite similar phenomenon and discovered that the depth of SSD would be influenced by radial distance from the wafer center [30]. Yin et al. present a statistical method to study the formation of SSD induced during grinding process [31]. Zhang et al. analytically predicted that the less depth of SSD in silicon wafer could be achieved with lower in-feed rate, lower wafer rotation speed and higher grinding wheel speed in the rotary in-feed grinding process [32]. Yan et al. also obtained the similar phenomenon in experiment results of SiC wafer grinding, as shown in Fig. 2.8 [33].

SSD, including phase transformation, dislocation and micro crack, is closely associated with the material removal mechanism. In grinding of monocrystalline wafer, the material removal in either ductile or brittle mode is one of the most interested issues [22, 34]. The cutting depth of each abrasive must be controlled to be less than the critical depth of cut (short for DOC) of ground wafers for the ductile mode grinding. The experimental investigation of the critical DOC for silicon wafers has been derived by Younge et al. [35, 36]. If the abrasive cutting depth is less than the critical DOC, a better surface roughness can

be achieved. Zhou et al. in the publication [37] also reported that the transition between the ductile and brittle modes can be controlled by the wheel and wafer rotational speed and in-feed rate. In addition, Lin et al. proposed that the elastic-plastic behaviors in both wheel and
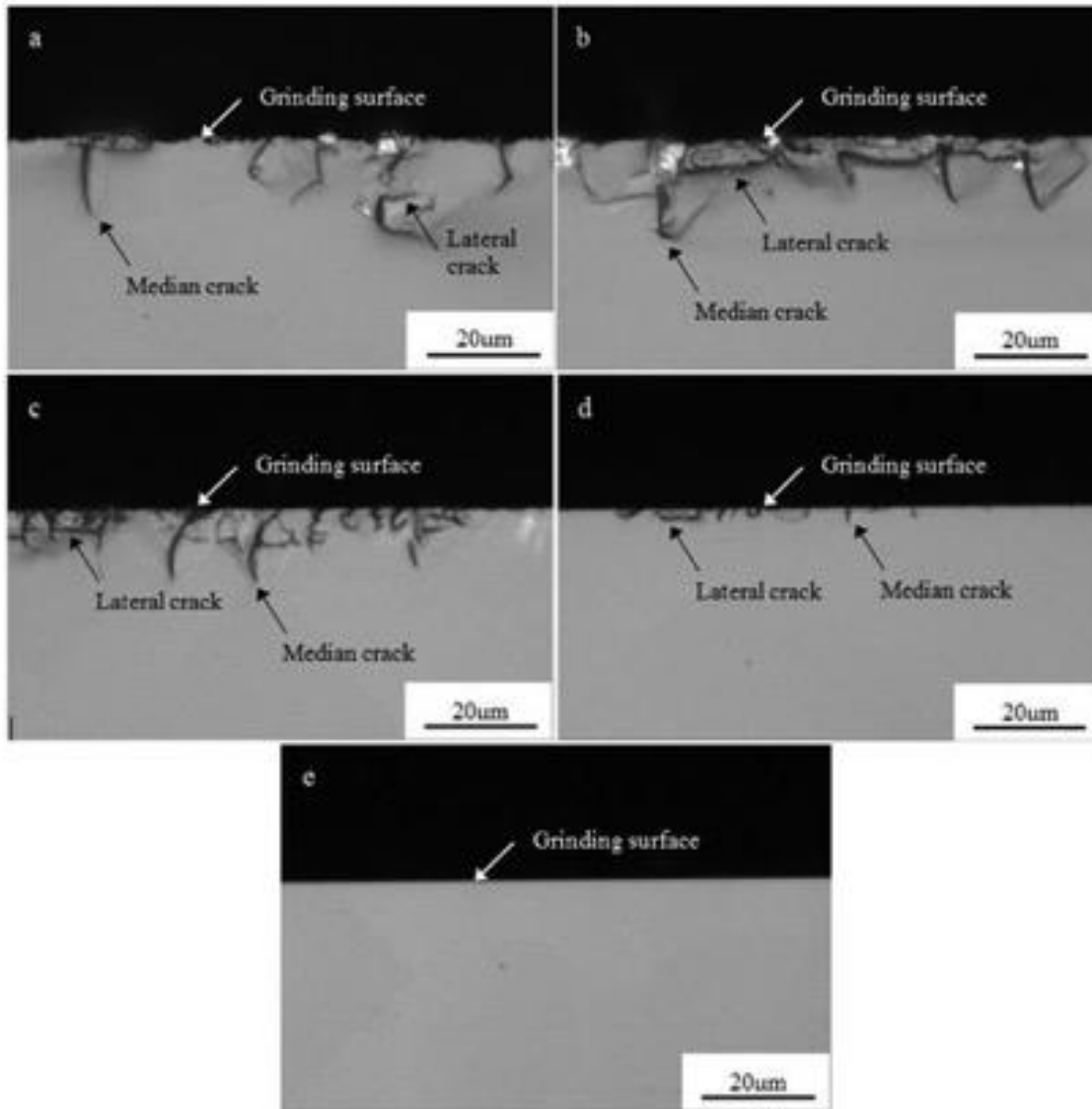
Fig. 2.8 Subsurface characteristics of ground SiC wafer for varying grinding conditions:

a) ground with #325 diamond wheel $f = 5$ [μm/s], $v_s = 19.1$ [m/s];

b) ground with #325 diamond wheel $f = 1$ [μm/s], $v_s = 19.1$ [m/s];

c) ground with #325 diamond wheel $f = 0.1$ [μm/s], $v_s = 19.1$ [m/s];

d) ground with #325 diamond wheel $f = 0.1$ [μm/s], $v_s = 31.84$ [m/s];

e) ground with #8000 diamond wheel $f = 0.1$ [μm/s], $v_s = 31.84$ [m/s] [33]

21

wafer should be taken into consideration for accurately predicting the abrasive depth of cut in rotary in-feed grinding [38].

In grinding, contact between an abrasive and wafer provides a local stress and strain concentration and temperature rise, which dominate the generation of SSD. The stress field is usually composed of a hydrostatic compressive stress that is superimposed by a shear stress and a tensile stress which is induced by frictional force at the interface of abrasive and wafer [39]. The complex stress field causes the material to deform through dislocation motions and cleavages. Therefore, the generation of SSD is closely related to the grinding force and grinding heat in the rotary in-feed grinding process. Couey et al. have developed a device for in-process force monitoring in precision grinding of silicon wafer, and thus indicated that the grinding force was mainly influenced by the in-feed rate [40]. Sun et al. provide a predictive model of grinding force in silicon wafer grinding, which correlated the grinding conditions to the grinding force and was validated by experimental results [41]. Ishibashi et al. found that the grinding force gradually grew up when the wheel segment started to engage from the wafer center, and rapidly dropped to zero when the wheel segment exits from the wafer periphery [42].

In order to associate not only the grinding conditions but also the wheel specifications with the grinding force and grinding heat, a dynamic and static analysis on the rotary in-feed grinding becomes necessary. Chapter 5 will report the grinding force exerted on an individual abrasive which is first correlated to the chip cross section and then extended to a single wheel segment and whole wafer.

Reference

[1]   Nishiguchi M., Sekiguchi T., Miyoshi I., Nishio K., (1991), Surface grinding machine, United States Patent, US5035087.

[2]   Matsui S., (1987), Some experimental studies on silicon wafer grinding -on the wafer rotation grinding method (1st report)-, Bulletin of the Japan Society of Precision Engineering, Vol. 53, No. 3, pp. 438-443 (in Japanese).

[3]   Tomita Y, Eda H., (1996), A study of the ultra precision grinding process on a magnetic disk substrate - Development of new bonding materials for fixed abrasives of grinding stone, Wear, Vol. 195, No. 1-2, pp. 74–80.

[4]   Pei Z.J., Strasbaugh A., (2001), Fine grinding of silicon wafers, International Journal of Machine Tools and Manufacture, Vol. 41, No. 5, pp. 659–672.

[5]   Shaw M., (1998), Principles of abrasive processing, Oxford.

[6]   Nishiguchi M., Goth N., (1992), Apparatus for grinding semiconductor wafer, United States Patent, US009120194B2.

[7]   Pei Z.J., Billingsley S.R., Miura S., (1999), Grinding induced subsurface cracks in silicon wafers, International Journal of Machine Tools and Manufacture, Vol. 39, No. 7, pp.1103-1116.

[8]   Tso P.L., Teng C.C., (2001), A study of the total thickness variation in the grinding of ultra-precision substrates, Journal of Materials Processing Technology, Vol. 116, No. 2-3, pp. 182-188.

[9]   Zhou L.B., Eda H., Shimizu J., (2002), State-of-the-art technologies and kinematical analysis for one-stop finishing of ϕ300 mm Si wafer, Journal of Materials Processing Technology, Vol. 129, No. 1-3, pp. 34-40.

[10]   Zhou L.B., Shinohara K., Shimizu J., Eda H., (2002), Kinematics of ultra precision grinding for large scale Si wafer, Precision Engineering, Vol. 68, No. 1, pp. 125-129 (in Japanese).

[11]   Zhou L.B., Shimizu J., Shinohara K., Eda H., (2003), Three-dimensional kinematical analyses for surface grinding of large scale substrate, Precision Engineering, Vol. 27, No. 2, pp. 175-184.

[12]   Sun W.P., Pei Z.J., Fisher G.R., (2004), Fine grinding of silicon wafers: a mathematical model for the wafer shape, International Journal of Machine Tools & Manufacture, Vol. 44, No. 7-8, pp. 707-716.

[13]   Sun W.P., Pei Z.J., Fisher G.R., (2005), Fine grinding of silicon wafers: machine configurations for spindle angle adjustments, International Journal of Machine Tools & Manufacture, Vol. 45, No. 1, pp. 51-61.

[14]   Zhang X.H., Pei Z.J., Fisher G.R., (2005), A grinding-based manufacturing method for silicon wafers: generation mechanisms of central dimples on ground wafers, International Journal of Machine Tools & Manufacture, Vol. 46, No. 3-4, pp. 397-403.

[15]   Zhou L.B., Mitsuta T., Shimizu J., Tian Y.B., Yamamoto T., (2010), Effects of machine tool stiffness and cutting path density on infeed face grinding of silicon wafer 1st Report: Modeling and analysis, Journal of the Japan Society for Abrasive Technology, Vol. 54, No. 1, pp. 45-49 (in Japanese).

[16]   Zhou L.B., Mitsuta T., Shimizu J., Tian Y.B., Yamamoto T., (2010), Effects of machine tool stiffness and cutting path density on infeed face grinding of silicon wafer 2nd Report: Empirical study, Journal of the Japan Society for Abrasive Technology, Vol. 54, No. 2, pp. 92-96 (in Japanese).

[17]   Kusuyama J., Iwahashi S., Kitajuma T., Ogasawara N., Yui A., Kitajima T., Saito H., Slocum A.H., (2015), Loop stiffness of grinding machine developed for 450 mm silicon wafers, Advanced Maerials Research, Vol. 1136, pp. 655-660.

[18]   Okahata G., Yui A., Kitajima T., Okuyama S., Saito H., Slocum A.H., (2014), Development of rotary work table with constant-flow hydrostatic water bearing for large scale silicon-wafer grinding machine, Advanced Maerials Research, Vol. 1017, pp. 604-609.

[19]   Ebina Y., Yoshimatsu T., Zhou L.B., Shimizu J., Onuki T., Ojima H., (2015), Process study on large-size silicon wafer grinding by using a small-dimeter wheel, Journal of Advanced Mechanical Design, Systems, and Manufacturing, Vol.9, No.5, pp. jamdsm0073.

[20]   Gao S., Dong Z., Kang R., Zhang B., Guo D.M., (2015), Warping of silicon wafers subjected to back-grinding process, Precision Engineering, Vol.40, pp. 87–93.

[21]   Kripesh V., Yoon S.W., Ganesh V.P., Khan N., Rotaru M.D., Fang W., et al., (2005), Three dimensional system in package using stacked silicon platform technology, IEEE Transactions on Advanced Packaging, Vol. 28, No.3, pp. 377–86.

[22]   Tönshoff H.K., Schmieden W.v., Inasaki I., König W., Spur G., (1990), Abrasive Machining of Silicon, Annals of the CIRP, Vol. 39, No. 2, pp. 621- 635.

[23]   Pei, Z. J., Strasbaugh A., (2002), Fine grinding of silicon wafers: Grinding marks, International Journal of Machine Tools and Manufacture, Vol. 42, No. 5, pp. 395-404.

[24]   Luo S.Y., Chen K.C., (2009), An experimental study of flat fixed abrasive grinding of silicon wafers using resin-bonded diamond pellets, Journal of Materials Processing Technology, Vol. 209, No. 2, pp. 686-694.

[25]   Liu Y.M., Warkentin A., Bauer R., Gong Y.D., (2013), Investigation of different grain shapes and dressing to predict surface roughness in grinding using kinematic simulations, Precision Engineering, Vol. 37, No. 3, pp. 758-764.

[26] Sun J.L., Chen P., Qin F., An T., Yu H.P., He B.F., (2018), Modelling and experimental study of roughness in silicon wafer self-rotating grinding, Precision Engineering, Vol. 51, pp. 625-637.

[27] Chen J. and Wolf I.D., (2003), Study of damage and stress induced by backgrinding in Si wafers, Semiconductor science and technology, Vol. 18. Vol. 4, pp. 261.

[28] Zhang B., Howes T.D., (1995), Subsurface evaluation of ground ceramics, Annals of the CIRP, Vol. 44, No. 1, pp. 263-266.

[29] Lundt H, Kerstan M, Huber A, Hahn PO., (1994), Subsurface damage of abraded silicon wafers, Semiconductor Silicon/1994: Proceedings of the 7th International Symposium on Silicon Materials Science and Technology, pp. 218–224.

[30] Gao S., Kang R., Guo D.M., Huang Q.S., (2010), Study on the subsurface damage distribution of the silicon wafer ground by diamond wheel, Advanced Materials Research, Vol. 126-128, pp. 113-118.

[31] Yin J.F., Bai Q., Li Y.N., Zhang B., (2018), Formation of subsurface cracks in silicon wafers by grinding, Nanotechnology and Precision Engineering, Vol. 1, pp. 172-179.

[32] Zhang L.X., Chen P., An T., Dai Y.W., Qin F., (2019), Analytical prediction for depth of subsurface damage in silicon wafer due to self-rotating grinding process, Current Applied Physics, Vol. 19., No. 5, pp. 570-581.

[33] Yan Q.S., Chen S.K., Pan J.S., Lu J.B., Liu Q., (2014), Surface and subsurface damage characteristics and material removal mechanism in 6H-SiC wafer grinding, Materials Research Innovations, Vol. 18, pp. S2-742.

[34] Marinescu I.D., Doi T.K., Uhlmann E., (2000), Handbook of ceramics grinding and polishing, Elsevier.

[35] Young HT, Liao HT, Huang HY., (2006), Surface integrity of silicon wafers in ultra precision machining, International Journal of Advanced Manufacturing Technology, Vol. 29, No. 3, pp. 372–378.

[36] Young HT, Liao HT, Huang HY., (2007), Novel method to investigate the critical depth of cut of ground silicon wafer, Journal of Materials Processing Technology, Vol. 182, No. 1-3, pp. 157–162.

[37] Zhou L, Tian YB, Huang H, Sato H, Shimizu J., (2012), A study on the diamond grinding of ultra-thin silicon wafers, Proceedings of the Institution of Mechanical Engineers, Part B: Journal of Engineering Manufacture, Vol. 226, No. 1,pp. 66–75.

[38] Lin B, Zhou P, Wang Z, Yan Y, Renke Kang DG., (2018), Analytical elastic plastic cutting model for predicting grain depth-of-cut in ultrafine grinding of silicon wafer, Journal of Manufacturing Science and Engineering, Vol. 140, No. 12, pp. 1118.

[39] Zhang B., Howes T.D., (1994), Material-removal mechanisms in grinding ceramics, Annals of the CIRP, Vol. 43, No. 1, pp. 305-308.

[40]   Couey JA, Marsh ER, Knapp BR, Ryan Vallance R., (2005), In-process force monitoring for precision grinding semiconductor silicon wafers, International Journal of Manufacturing Technology and Management, Vol. 7, No. 5/6, pp. 430–440.

[41]   Sun J, Qin F, Chen P, An T., (2016), A predictive model of grinding force in silicon wafer self-rotating grinding, International Journal of Machine Tools and Manufacture, Vol. 109, No. 10, pp. 74–86

[42]   Ishibashi K, Tsukii Y, Ebina Y, Zhou L, Shimizu J, Yamamoto T, et al., (2019), Study on mechanism of rotary in-feed face grinding: Development of wireless dynamometer for rotary infeed face grinding, Journal of the Japan Society for Abrasive Technology, Vol. 63, No. 1, pp. 31–35 (in Japanese).

Chapter 3 Wafer profile and geometry

According to the literature surveyed, wafer profile or geometry is one of most important indexes to evaluate the performance of rotary in-feed grinding. In this chapter, the motion and path of cutting edge in rotary in-feed grinding are kinematically analyzed in 3D. It is useful to address the behavior of each abrasive in generation of the wafer profile. The effects of both cutting path density and machine stiffness are also assessed. Therefore, the mathematical analysis and experiments are described in this chapter as a guidance to obtain and optimize the grinding conditions for achieving high wafer geometry.

3.1 Description of rotary in-feed grinding model

In chapter 2, a lot of literature works showed that the grinding machine configuration and grinding conditions significantly influence on ground wafer shape and profile. Thus, it is necessary to make a deeper insight view to the grinding dynamics of rotary in-feed grinding. In order to associate the grinding conditions with the wafer shape and profile generation, a mathematical analysis is made to address the behavior of each abrasive in wafer surface

(a) Overall view of rotary in-feed grinding   (b) Projection in $X - Y$ plane
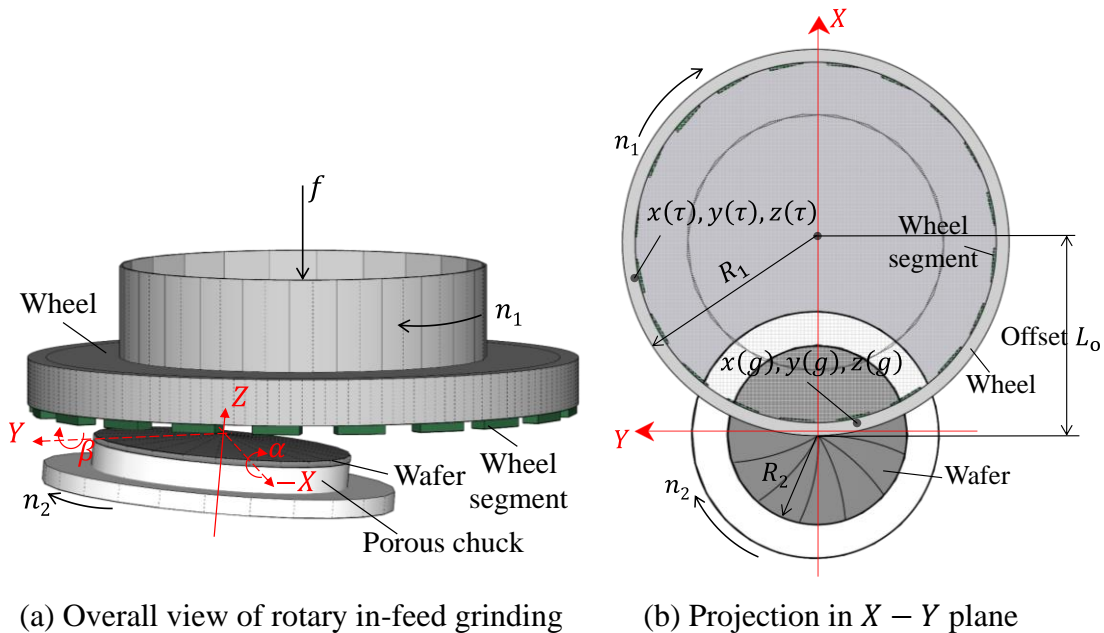
Fig. 3.1 Rotary in-feed grinding model

generation [1-7]. Fig. 3.1 illustrates a model of three-dimensional rotary in-feed grinding

Table 3.1 The symbols used for the rotary in-feed grinding dynamic model description
and the following analysis

	R_1	Wheel radius	[mm]
	l	Wheel segment length	[mm]
	w	Wheel segment width	[mm]
Wheel specifications	r_g	Abrasive radius	[μm]
	r_0	Average abrasive radius	[μm]
	V_g	Abrasive concentration	[vol%]
	j	The number of effective cutting edge	[pratical]
Wafer specifications	R_2	Wafer radius	[mm]
	r_2	Radial distance from the wafer center	[mm]
	L_o	Offset of wheel and wafer axes	[mm]
	n_1	Wheel rotational speed	[min^{-1}]
	n_2	Wafer rotational speed	[min^{-1}]
Grinding conditions	f	In-feed rate	[mm/min]
	τ	Grinding time	[min]
	α	Tilt angle around wafer X axis	[°]
	β	Tilt angle around wafer Y axis	[°]
	b	Individual abrasive cutting width	[μm]
	k_g	Machine tool stiffness	[N/μm]
	k_w	Wafer stiffness	[N/μm]
Symbol used for evaluations	K	Stiffness factor	—
	h	Actual cutting depth	[μm]
	Δ	Cutting depth	[μm]
	η	Cutting path density	—

28

and the principle of wheel/wafer engagement. The cup-type grinding wheel is down fed to the wafer with a constant in-feed rate f while both grinding wheel and wafer rotate around their own axes simultaneously during the grinding process. A wafer is mounted via a porous vacuum chuck and a cup-type grinding wheel is placed opposite with an offset equivalent to the wheel radius R_1. The porous vacuum chuck has tilt angles denoted as α and β, respectively around $X-$ and $Y-$axis, as shown in Fig. 3.1 (a). The projection in $X-Y$ plane is illustrated in Fig. 3.1 (b), where the relevant parameters are labeled. The symbols used in made description and the subsequent analysis are listed in Table 3.1.

3.2 Kinematical analysis of cutting path

In a cartesian coordinate system with the origin fixed at the wafer center, the mathematical description of the cutting path for an abrasive to travel across the wafer surface in two-dimensional space is described in the publication [4]. By taking the tilt angles α and β into the consideration, the cutting path description is then updated to three-dimensional space and given in a matrix form as Eq. (3-1).

$$\begin{bmatrix} x(\tau) \\ y(\tau) \\ z(\tau) \\ 1 \end{bmatrix} = A \cdot B \cdot C \cdot D \cdot E \cdot F \begin{bmatrix} x_g \\ y_g \\ z_g \\ 1 \end{bmatrix} \tag{3-1}$$

where (x_g, y_g, z_g) is the initial position of the corresponding abrasive and τ is the grinding time. The matrices A and E represent the rotations of wafer and wheel respectively and are specified as;

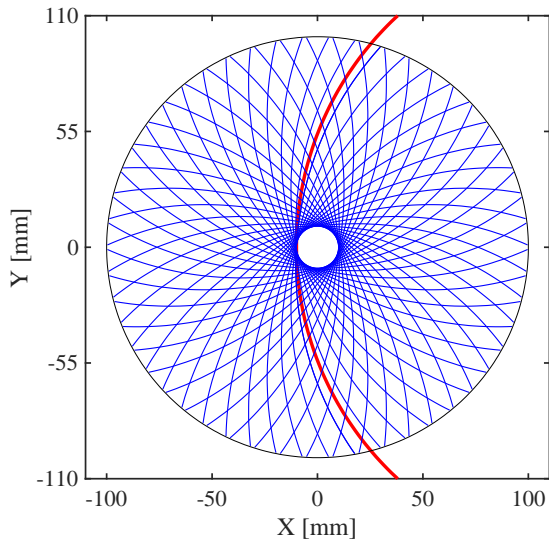$$A = \begin{bmatrix} \cos 2\pi n_2 \tau & \sin 2\pi n_2 \tau & 0 & 0 \\ -\sin 2\pi n_2 \tau & \cos 2\pi n_2 \tau & 0 & 0 \\ 0 & 0 & 1 & 0 \\ 0 & 0 & 0 & 1 \end{bmatrix} \tag{3-2}$$

$$E = \begin{bmatrix} \cos 2\pi n_1 \tau & -\sin 2\pi n_1 \tau & 0 & 0 \\ \sin 2\pi n_1 \tau & \cos 2\pi n_1 \tau & 0 & 0 \\ 0 & 0 & -f\tau & 0 \\ 0 & 0 & 0 & 1 \end{bmatrix} \tag{3-3}$$
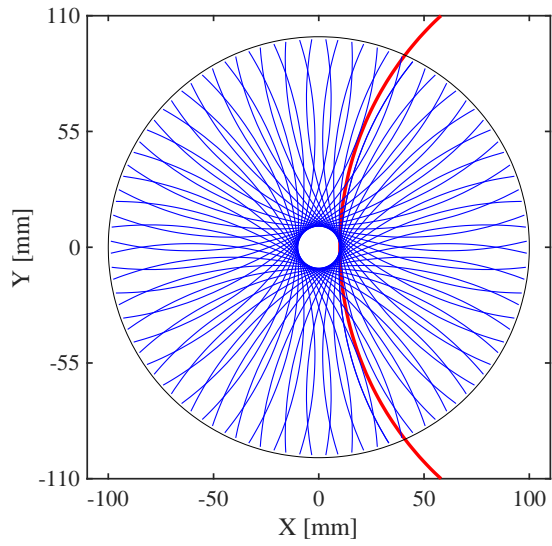
while, the matrices B and C respectively express the tilt angles of wafer α around X-axis and β around Y-axis, are given as;

$$\boldsymbol{B} = \begin{bmatrix} 1 & 0 & 0 & 0 \\ 0 & \cos\alpha & -\sin\alpha & 0 \\ 0 & \sin\alpha & \cos\alpha & 0 \\ 0 & 0 & 0 & 1 \end{bmatrix} \tag{3-4}$$

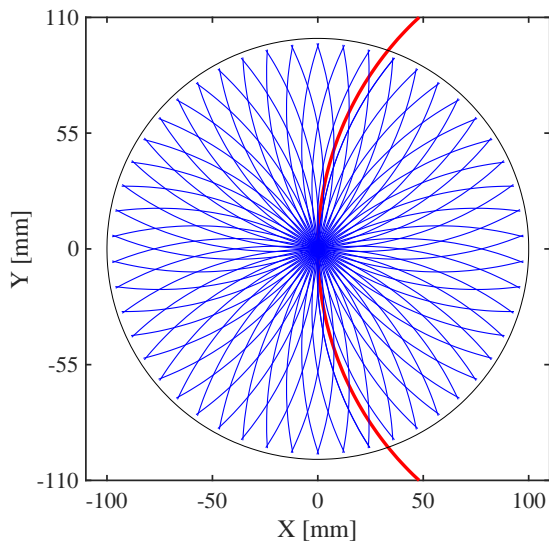$$\boldsymbol{C} = \begin{bmatrix} \cos\beta & 0 & \sin\beta & 0 \\ 0 & 1 & 0 & 0 \\ -\sin\beta & 0 & \cos\beta & 0 \\ 0 & 0 & 0 & 1 \end{bmatrix} \tag{3-5}$$
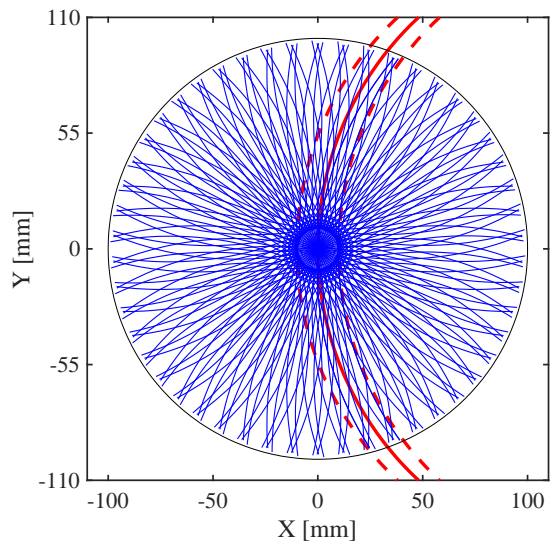

(a) $L_o < R_1$

(b) $L_o > R_1$

(c) $L_o = R_1$

(d) $L_o = R_1$

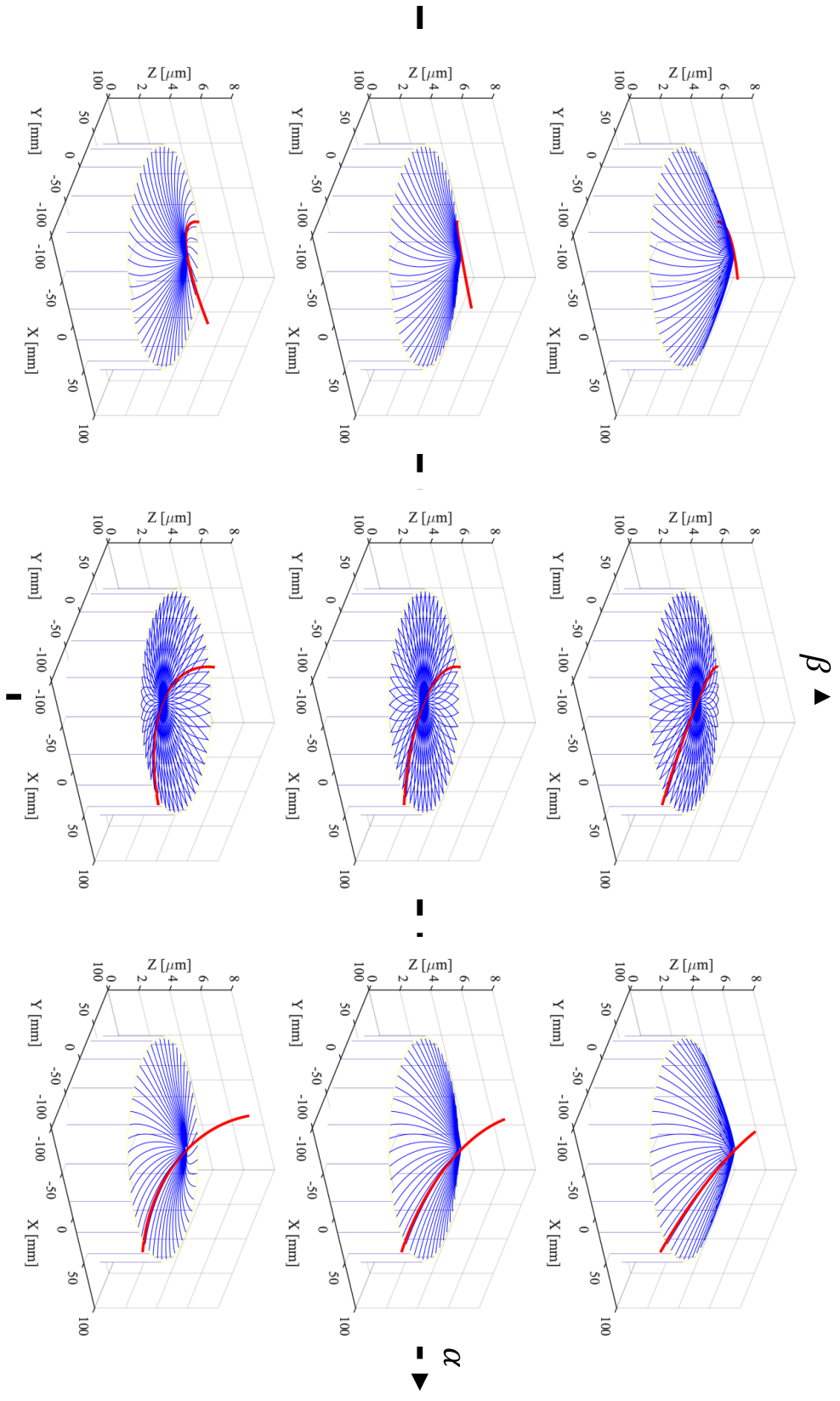Fig. 3.2 The effect of offset L_o ($< R_1$, $> R_1$, $= R_1$)
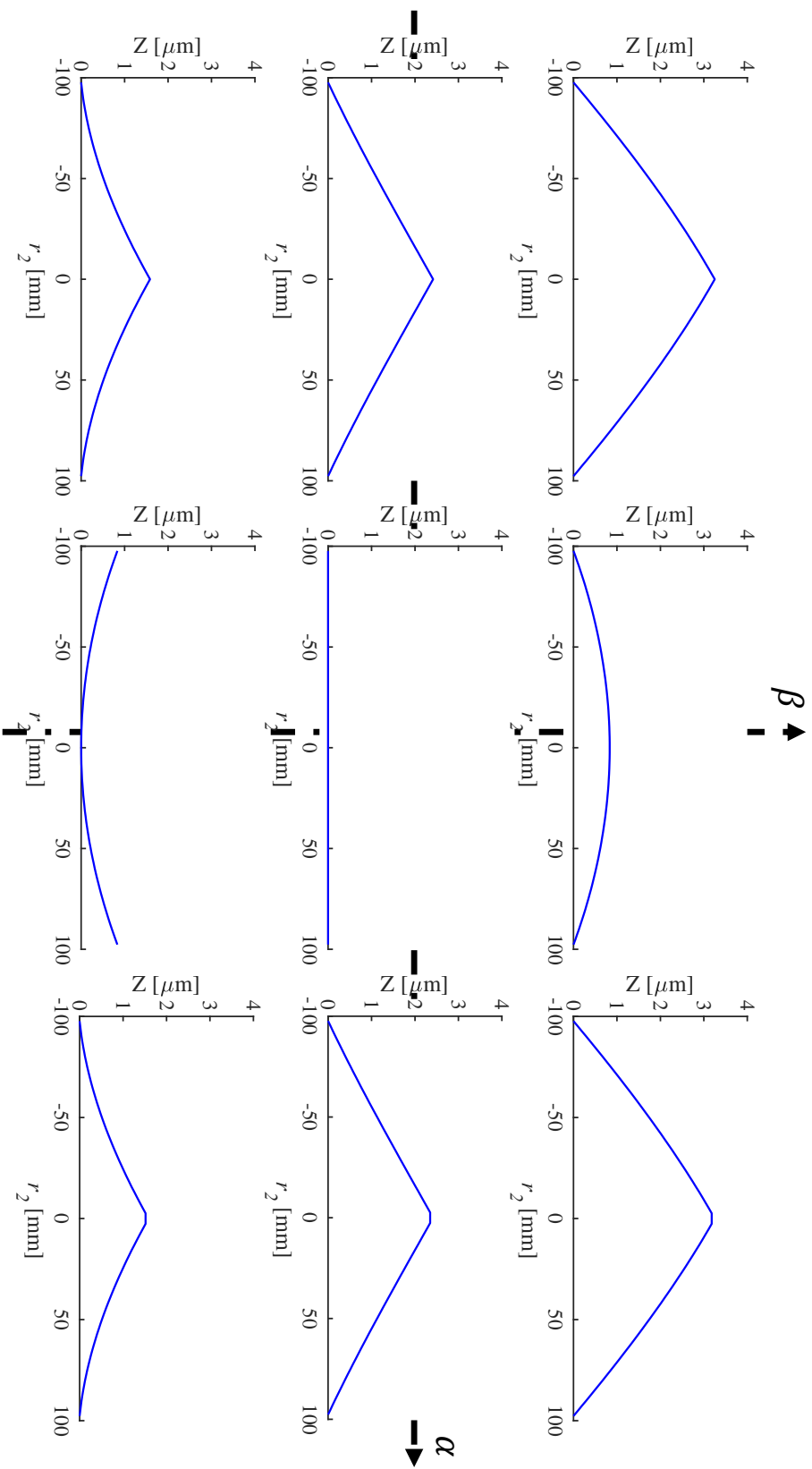
Fig. 3.3 The effect of tilt angle α and β

31

Fig. 3.4 Sectional view of wafer profile

and, the matrices D and F are the translations of the offset L_o.

$$D = \begin{bmatrix} 1 & 0 & 0 & L_o \\ 0 & 1 & 0 & 0 \\ 0 & 0 & 1 & 0 \\ 0 & 0 & 0 & 1 \end{bmatrix} \tag{3-6}$$

$$F = \begin{bmatrix} 1 & 0 & 0 & -L_o \\ 0 & 1 & 0 & 0 \\ 0 & 0 & 1 & 0 \\ 0 & 0 & 0 & 1 \end{bmatrix} \tag{3-7}$$

As an example, the cutting path calculated according to Eq. (3-1) at the conditions of the wheel radius $R_1 = 150$ [mm], the rotational speed ratios $n_1/n_2 = 50/1$ and the tilt angles of wafer axis $\alpha = \beta = 0[°]$, are shown in Fig. 3.2, where the red circles represent the position of the wheel, the blue lines represent the cutting path generated by a single abrasive. It is easily understood that the offset L_o determines the occurrence of uncut area. In the case of $L_o < R_1$ or $L_o > R_1$, the uncut area is left to the wafer center $r_2 = |R_1 - L_o|$, as shown in Fig. 3.2 (a) and (b). Therefore, the offset L_o must be set/equal to the wheel radius R_1 to grind the entire wafer surface as shown in Fig. 3.2 (c). Even in case of $L_o = R_1$, however, both edges of the wheel (dash red lines) could still leave unfavorable cutting marks on the wafer surface as shown in Fig. 3.2 (d) if the wheel is not dressed properly.

In order to quantitatively understand the effects of the combination of tilt angles of wafer rotational axis, the cutting paths are calculated according to the Eq. (3-1). When the wafer axis is unparallel to the wheel axis, the interference has to be discussed in 3D manner. Fig. 3.3 shows a series of wafer profiles, where the wafer profiles were formed by varying the tilt angles of α and β from 1.5×10^{-3} [°]~ 1.5×10^{-3}[°].

According to the results in Fig. 3.3, not matter the tilt angle α is either positive or negative, the wafer profile becomes a convex cone shape so that the wheel constantly makes a half-contact with the wafer surface during grinding. When $\alpha = 0[°]$, the wheel has a full contact with the wafer and the bidirectional cutting path is generated where a negative β leads to a concave profile, and a positive β makes a convex profile, as shown in the center column of Fig. 3.3. Therefore, the very intrinsic nature of combination of tilt angles leads to a fact that the tilt angle α is dominates the way of contact between the wheel and wafer, and the direction of cutting path.

On the other hand, tilt angle β effects on the wafer surface profile too. The results could also be found in the cross-sectional views as shown in Fig. 3.4, which presents the wafer profile obtainable at the corresponding tilt angles. Mathematically, it is possible to create a desirable axisymmetric profile on the wafer surface by properly aligning the tilt angles. The
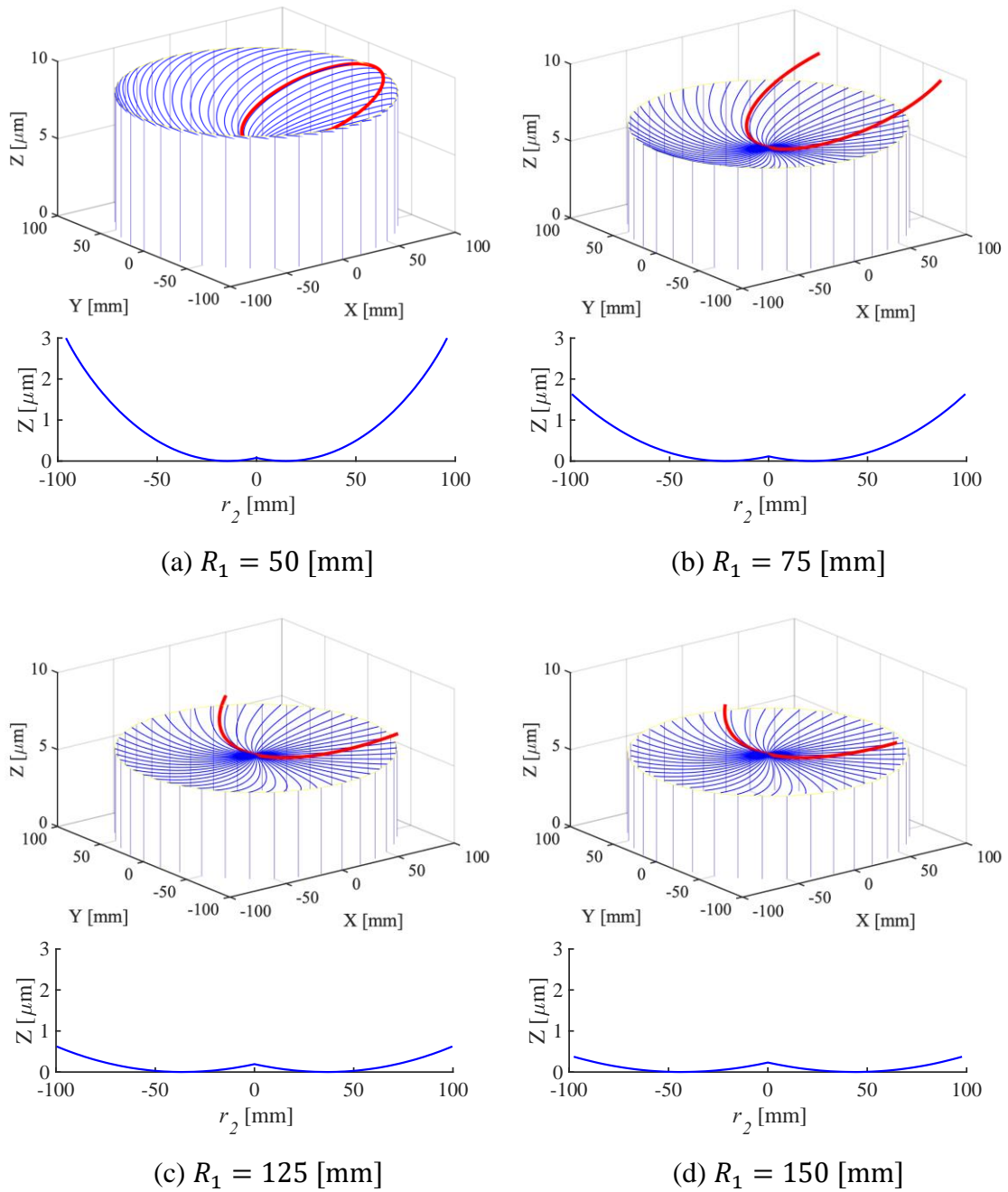

(a) $R_1 = 50$ [mm]

(b) $R_1 = 75$ [mm]

(c) $R_1 = 125$ [mm]

(d) $R_1 = 150$ [mm]

Fig. 3.5 The effect of wheel size R_1

ideal flat wafer (TTV=0) is achievable by paralleling wheel axis to the wafer axis ($\alpha = \beta = 0[°]$). However, tilt angle $\alpha = 0[°]$ is not favored from the viewpoints of reducing the contact length and grinding resistance in wafer grinding. Therefore, the tilt angle $\alpha \neq 0[°]$ is often presented in wafer manufacturing.

The effect of wheel radius R_1 on wafer profile is also studied, and a series of 3D view of wafer profiles and cross-sectional views are shown in Fig. 3.5, where the wafer profiles ($R_2 = 100$ [mm]) are calculated for a combination of the tilt angle $\alpha = -1 \times 10^{-5}[°]$ and $\beta = -3.5 \times 10^{-5}[°]$, by varying the wheel radius $R_1 = 50 \sim 150$ [mm]. First of all, the wheel diameter must be larger than the wafer radius ($2R_1 \geq R_2$), in order to remove the material from the entire wafer surface. Second, a larger wheel diameter leads to a better wafer flatness. The mathematical analysis and simulation results agreed quantitatively with the experimental results which are presented by Ebina et al. [6]. In other words, a particular attention needs to be paid when selecting grinding wheels ($R_1 > R_2$) in wafer manufacturing.

3.3 Effects of speed ratio on cutting path periodicity and density

Shown in Fig. 3.6 are the cutting path periodicitys made at different speed ratios n_1/n_2, and projected in $X - Y$ plane. The cutting path periodicity ω is obviousely determined by
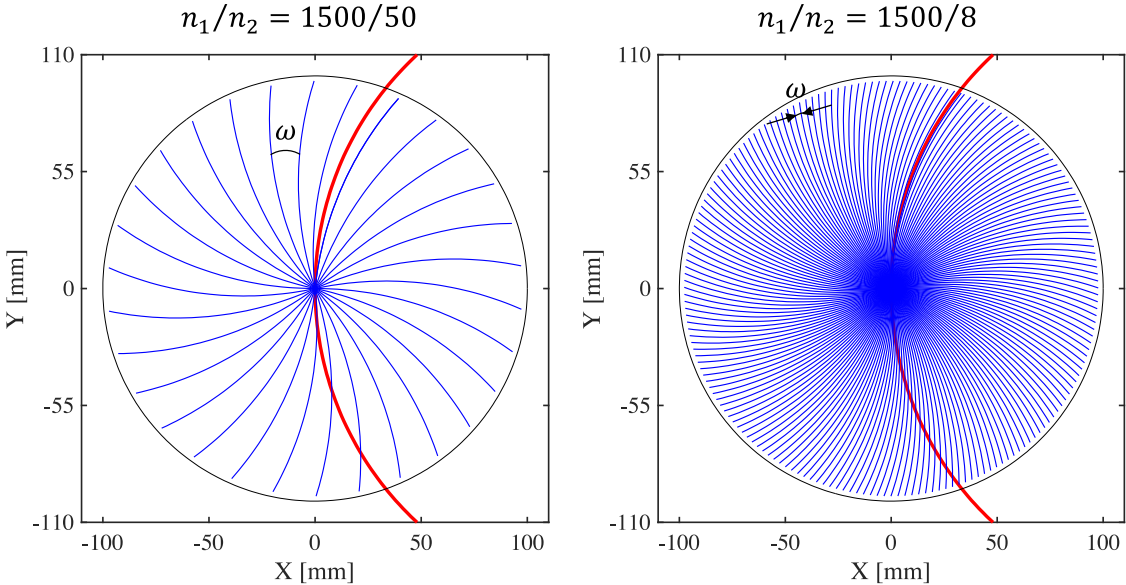

$$n_1/n_2 = 1500/50 \qquad n_1/n_2 = 1500/8$$

Fig. 3.6 Speed ratio effects on cutting path periodicity ($\omega = 2\pi / \frac{n_1}{n_2}$) and density
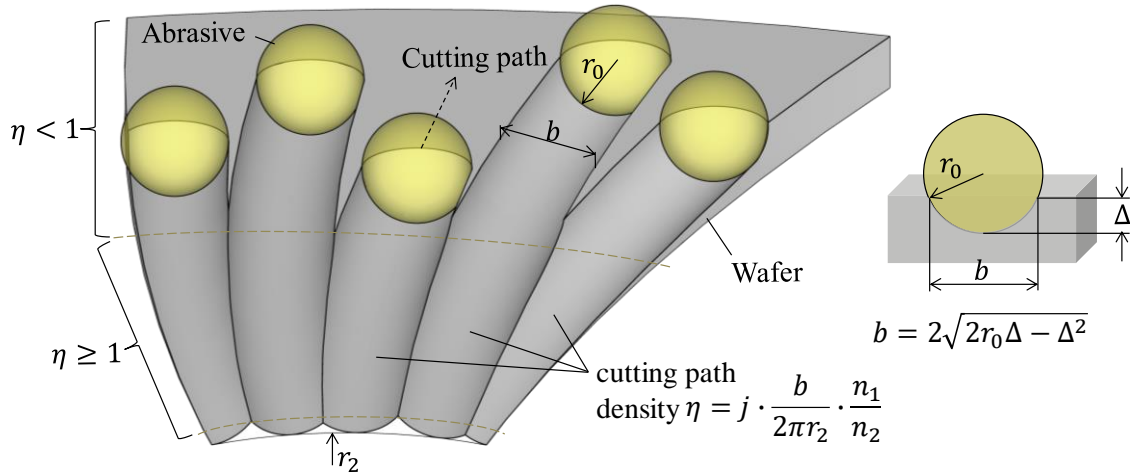
Fig. 3.7 Illustration of cutting path density

the speed ratio n_1/n_2 of the grinding wheel against the wafer. It is found that the number of cutting path made by an individual abrasive in one wafer rotation is equal to the numerator of reduced fraction in n_1/n_2. In other words, the path periodicity ω is inversely proportional to the speed ratio n_1/n_2. By increasing the speed ratio n_1/n_2, the phenomenon of overlap in cutting path increases and results in better surface roughness. In the meantime, the larger overlap ratio might leads to severe burn marks on the wafer surface. Thus, choosing an appropriate speed ratio is able to improve the performace of rotary in-feed grinding.

Obviously, Fig. 3.6 also showed that the speed ratio n_1/n_2 contributes great influence on the cutting path density. In addition, the cutting path density or overlap ratio in center is always higher than that in wafer periphery no matter how the speed ratio varies. Illustrated in Fig. 3.7 is the cutting path generated on a ground wafer surface. The cutting path density η at specific wafer radial distance r_2 is stated as:

$$\eta = j \cdot \frac{b}{2\pi r_2} \cdot \frac{n_1}{n_2} \tag{3-8}$$

where, j is the number of effective cutting edges on the entire wheel working surface. b is the cutting width generated by an individual abrasive and given by;

$$b \doteqdot 2\sqrt{2r_0\Delta - \Delta^2} \tag{3-9}$$

here, r_0 is and average of abrasive radius used in the wheel, Δ is the depth of cut given to the wafer in one rotation ($\Delta = f/n_2$).

By substituting Eq. (3-9) into Eq. (3-8), the expression of η can be obtained as;

$$\eta = j \cdot \frac{\sqrt{2r_0\Delta - \Delta^2}}{\pi r_2} \cdot \frac{n_1}{n_2} \qquad (3\text{-}10)$$

As shown in Fig. 3.7, the overlap of cutting path takes place when $\eta \geq 1$. It is noted that the cutting path density is inversely proportional to the wafer radial distance r_2. The cutting path density calculated at different speed ratio are shown in Fig. 3.8 as a function of r_2, where
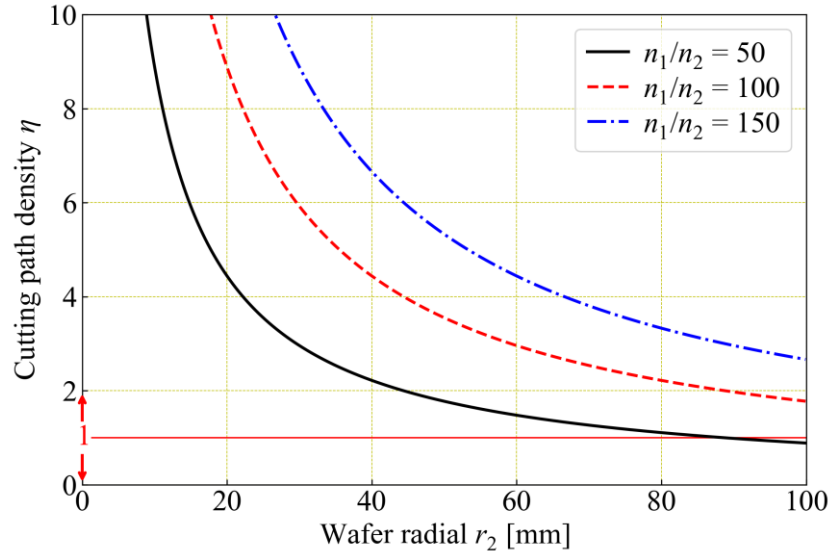

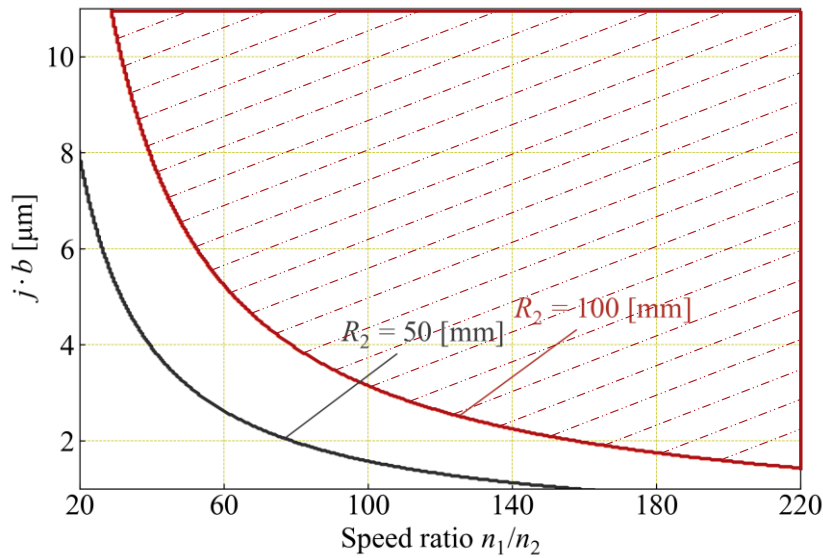Fig. 3.8 Cutting path density variation along wafer radial distance

Fig. 3.9 Critical conditions for cutting path density $\eta \geq 1$

37

the wafer rotational speed $n_2 = 20\,[\text{min}^{-1}]$, in-feed rate $f = 0.1\,[\text{mm/min}]$, average abrasive radius $r_0 = 6 \times 10^{-3}\,[\text{mm}]$ and the wheel rotational speed varying in $n_1 = 1000 \sim 3000\,[\text{min}^{-1}]$. In spite of the change in speed ratio n_1/n_2, the density sharply increases toward to the wafer center. Therefore, the phenomenon of overlap of cutting path $(\eta \geq 1)$ always occurs in wafer center. On the other hand, the cutting path density gradually becomes lower as increasing in the wafer radial distance r_2. Especially at low rotational speed ratio (an example given by $n_1/n_2 = 50$), the cutting path density η could be lower than 1 at the wafer outer circumference, which means the uncut area remaining in the periphery of the wafer. Therefore, in order to ensure $\eta \geq 1$ accross the entire wafer surface, it is important to optimize the grinding conditions according to the wafer size and wheel specifications. Fig. 3.9 shows the critical condition on the feature map of speed ratio n_1/n_2 and the wheel specifications for different wafer size R_2. The results suggest that the combination of the grinding conditions (n_1/n_2) and wheel specifications $(j \cdot b)$ must meet the criteria to ensure $\eta \geq 1$ in accordance with the wafer size R_2.

## 3.4 Effects of cutting path density and machine tool stiffness on wafer profile

From the mathematical analysis results above, it is easy to understand in the area of a wafer where the cutting path density $\eta < 1$, that part of the wafer surface remains uncut. Therefore, the actual cutting depth h is expected to be smaller than the given cutting depth Δ. Whereas for $\eta \geq 1$, the actual cutting depth h is equal to the given cutting depth Δ. They are described as below;

$$\begin{cases} h = \eta \cdot \Delta & (\eta < 1) \\ h = \Delta & (\eta \geq 1) \end{cases} \tag{3-11}$$

In the region of $\eta < 1$, the wafer profile presents the "sunken" like shape due to $h < \Delta$.

This still is the ideal case where the machine tool stiffness is considered as a rigid body while the ground wafer has no elastic deformation. However, the practical case becomes more complicate when the stiffnesses of machine tool, grinding wheel and wafer are taken into consideration. Fig. 3.10 (a) schematically shown the transition of actual cutting depth h

along with the wafer radial distance r_2. When the contact stiffness of grinding wheel is k_g and the dynamic rigidity of wafer is k_w, the stiffness factor K in Eq. (3-12) is used to describe
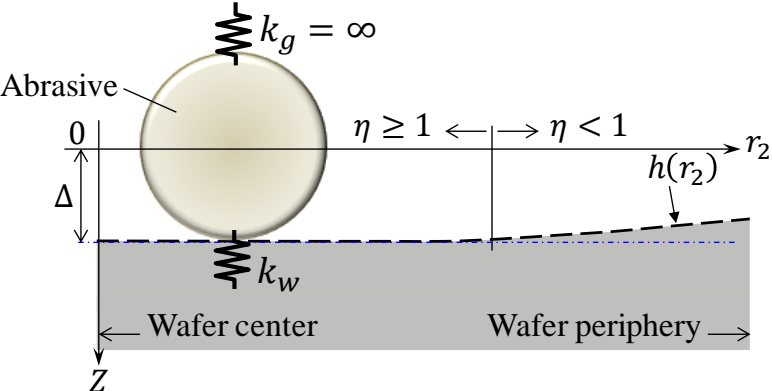
(a) Effect of cutting path density when stiffness factor $K = 1$
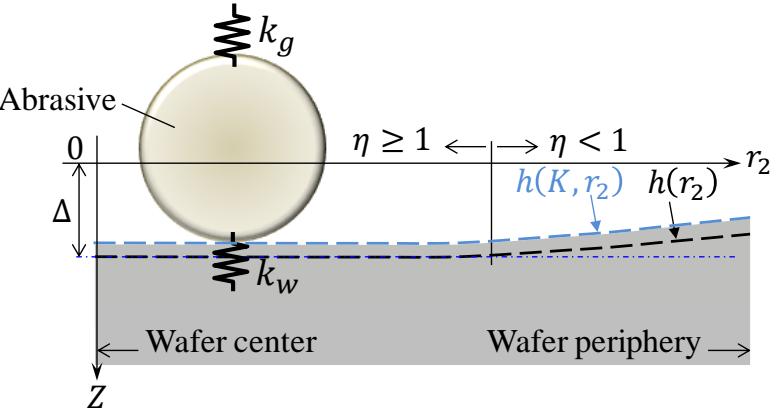
(b) Effect of cutting path density when stiffness factor $0 < K < 1$
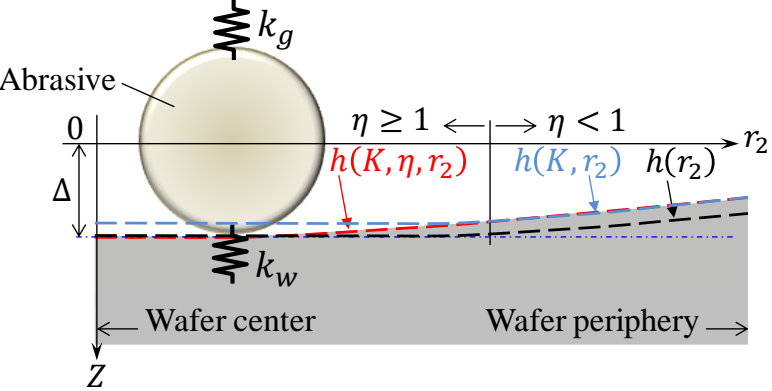
(c) Effect of cutting path density, spark-out and the stiffness factor $(1 - K)^{\eta}$

Fig. 3.10 Illustration of the effect of cutting path density and machine tool stiffness

the loop stiffness of the machine tool.

$$K = \frac{k_g}{k_g + k_w} \tag{3-12}$$

In the ideal case where the machine tool and the grinding wheel are rigid bodies or $k_g = \infty$ and $k_w = \infty$, $K = 1$, the actual cutting depth h follows Eq. (3-11) and appears in Fig. 3.10 (a). In actual case, K ranges in $0 < K < 1$, depending on the relative stiffness of machine tool against the hardness of the wafer. The actual cutting depth h can be obtained by multiplying the stiffness factor K, as expressed in Eq. (3-13).

$$\begin{cases} h = K \cdot \eta \cdot \Delta & (\eta < 1) \\ h = K \cdot \Delta & (\eta \geq 1) \end{cases} \tag{3-13}$$

The effect of stiffness factor K on actual removal depth of cut is schematically shown in Fig. 3.10 (b), where the black broken line represents the actual cutting depth h when the stiffness factor $K = 1$, the blue broken line represents the actual cutting depth h when the stiffness factor $0 < K < 1$.

In the region where $\eta \geq 1$, additionally, the wafer surface is supposed to be cut multiple (η) times. This is as same as "spark-out" grinding under a fixed depth of cut. According to Eq. (3-13), the residual height changes by $(1 - K) \cdot \Delta$, $(1 - K)^2 \cdot \Delta$, ... $(1 - K)^n \cdot \Delta$ after n times "spark-out" process. Therefore, depending on the relative stiffness of machine tool against the hardness of the wafer and cutting path density, the final form of actual cutting depth h can be expressed as Eq. (3-14).

$$\begin{cases} h = K \cdot \eta \cdot \Delta & (\eta < 1) \\ h = \{1 - (1 - K)^\eta\}\Delta & (\eta \geq 1) \end{cases} \tag{3-14}$$

The resultant actual cutting depth h from stiffness K and path density η on the radial distance is schematically shown by the red broken line in Fig. 3.10 (c). in the center of the wafer where $\eta \gg 1$, the actual cutting depth h gradually approaches to the given depth of cut Δ.

Fig. 3.11 shows a series of sectional view of wafer profiles calculated by Eq. (3-14) at the condition of the tilt angles $\alpha = 0[°]$ and $\beta = 0[°]$. The effect of stiffness factor on wafer profile is studied and shown in Fig. 3.11 (a), where the wafer profiles are calculated from a combination of the wheel rotational speed $n_1 = 2000 \, [\text{min}^{-1}]$, wafer rotational speed $n_2 = 50 \, [\text{min}^{-1}]$ and grinding wheel specification $j \cdot b = 5 \, [\text{mm}]$, by varying the stiffness factor
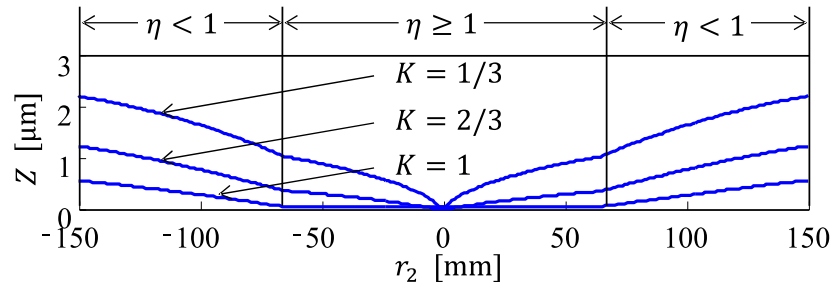
(a) Effect of stiffness factor
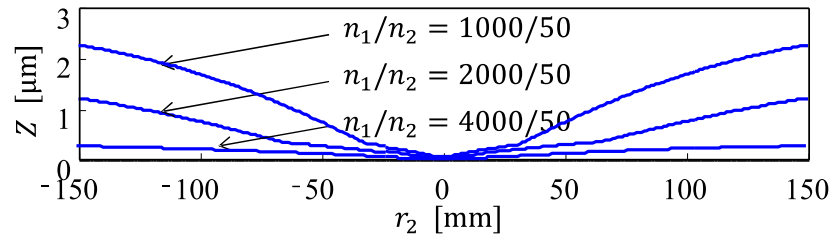
(b) Effect of rotational speed ratio
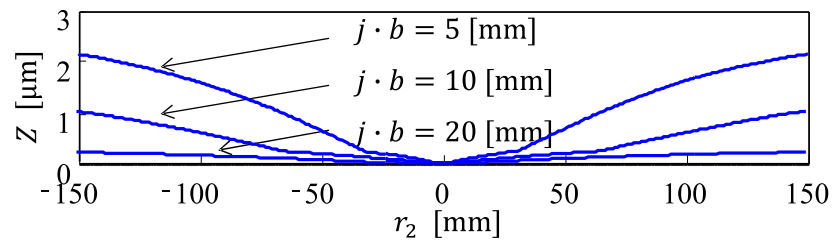
(c) Effect of grinding wheel specification

Fig. 3.11 Cutting path density and machine tool stiffness effects on wafer profile

$K = 1/3 \sim 1$. Obviously, the stiffness factor K has a great influence on the wafer profile. Higher stiffness of machine and tool gives a better wafer geometry accuracy, or TTV [8]. It is critical to use a grinding machine with high rigidity for high precision grinding [9-11].

Fig. 3.11 (b) shows the effect of rotational speed ratio on wafer profiles at the grinding wheel specification $j \cdot b = 5$ [mm], the stiffness factor $K = 2/3$. It reveals that a higher rotational speed ratio leads to a better wafer flatness.

Fig. 3.11 (c) shows the effect of wheel specifications j, b on wafer profiles at the conditions of the rotational speed ratio $n_1/n_2 = 2000/50$, the stiffness factor $K = 2/3$. Clearly, the grinding wheel specification $j \cdot b$ also greatly influences on the wafer profile.
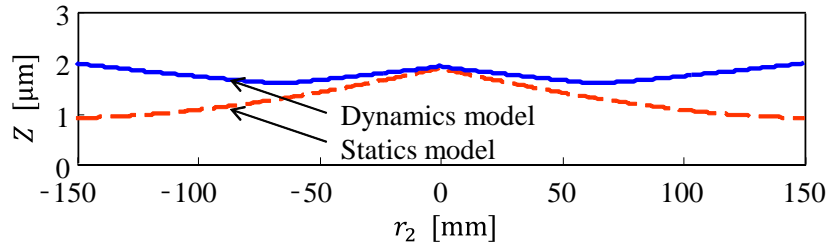
Fig. 3.12 Simulation results of wafer profile in proposed dynamics model

The number of effective cutting edge j is proportional to the abrasive concentration and increases inversely with the square of abrasive r_0 while the cutting width b is proportional to the square root of average abrasive radius r_0. Thus, it leads a fact that choosing a grinding wheel with high abrasive concentration and small average abrasive radius is able to produce a better wafer profile.

As mentioned above, the wafer profile can be improved through the optimization of grinding condition and wheel specification, but still presents in an axis symmetrical concave form as long as the stiffness of machine tool is limited. As a solution, tilt angle α and β is used to counterbalance this "concave" effect. An example is given in Fig. 3.12, where $\alpha = 6 \times 10^{-4}[°], \beta = -3 \times 10^{-3}[°]$. The TTV for $\emptyset 300$ [mm] wafer can be improved from 1.2 [μm] to 0.3 [μm] by the proposed dynamics model.

3.5 Experiments

Based on the analysis mentioned above, the experiments were carried out on a horizontal type rotary in-feed precision grinding machine (UPG-300H), which was developed by Eda and Zhou et al. [4], offers a less energy consumption and less environmental impact. Fig. 3.13 shows its external view and zoom-up of the rotary in-feed grinding machine, on which a diamond wheel (SD400N100DK100) and $\emptyset 200$ [mm] Si wafer is mounted. The machine has two-degree of freedom; the wafer spindle moves along $X-$ direction, while the wheel spindle along $Z-$ direction (in-feed direction). Each spindle comes with an aerostatic bearing and a built-in ac servomotor, which rotates at the range of $1.8 \sim 1800$ [min^{-1}] with the maximum run-out of 0.02 [μm]. A typical arrangement, in which the wheel was offset by a distance of R_1, was made. The eight-inch ($\emptyset 200$ [mm]) silicon wafer (with (100) plane)

was held by a vacuum chuck. The diamond grinding wheel moved towards the silicon wafer by a constant in-feed rate f. The tilt angles of wafer axis α, β are adjustable in range of
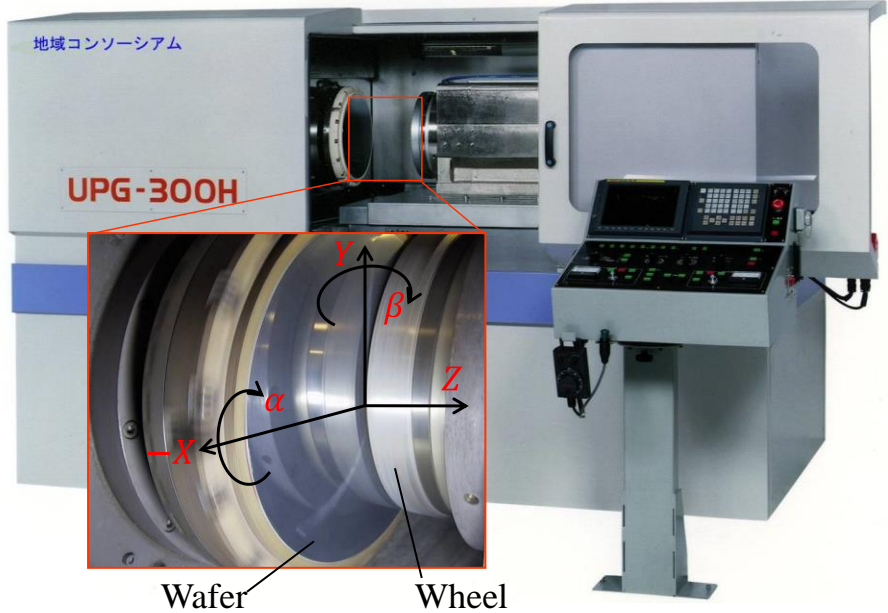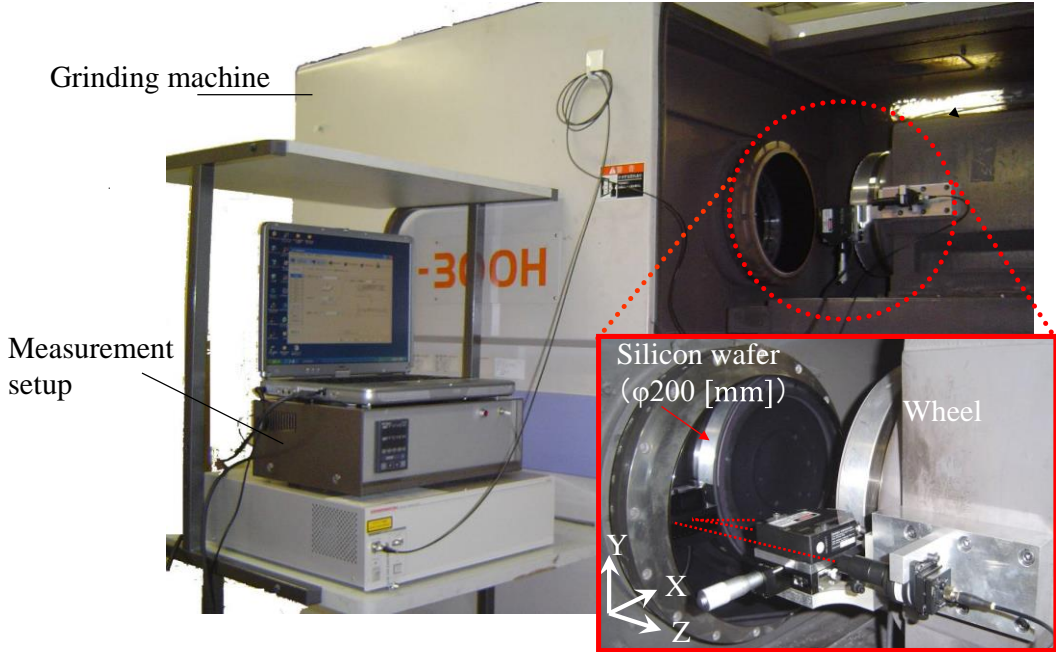

Fig. 3.13 UPG-300H rotary in-feed grinding machine

Fig. 3.14 On-machine measurement system

Table 3.2 Experiment conditions

Notations		Parameters	Unit
Tilt angle of wafer axis	α	$0\sim5\times10^{-3}$	[°]
Tilt angle of wheel axis	β	$-5\times10^{-3}\sim5\times10^{-3}$	[°]
Wheel rotational speed	n_1	1800	$[\text{min}^{-1}]$
Wafer rotational speed	n_2	100	$[\text{min}^{-1}]$
In-feed rate	f	10	[μm/min]
Wheel radius	R_1	150	[mm]
Wafer radius	R_2	100	[mm]
Wheel width	w	3	[mm]

$0[°]\sim-5\times10^{-3}[°]$ and the detailed experimental conditions are listed in Table 3.2. After the grinding process, the ground wafer profile was measured by an on-machine measurement system, which used a laser interferometer, as shown in Fig. 3.14 [12].

According to the SD400 resin bond grinding wheel specification, the average of abrasive radius $r_0 = 20$ [μm], the concentration $V_g = 25\%$, respectively. The number of effective cutting edge $j = 125$ [practical] for the SD400 resin bond grinding wheel is calculated by mathematical analysis reported in section 4.1 [12]. The machine and tool have the stiffness factor $K = 2/3$ [13].

The left panel of Fig. 3.15 shows the simulated TTV results and the right panel of Fig. 3.15 shows the experimental TTV results. At the conditions of the tilt angle $\alpha = 5\times10^{-3}[°], \beta = 0[°]$, the wafer profile becomes a convex cone shape. At the conditions of tilt angle $\alpha = 0[°], \beta = -5\times10^{-3}[°]$, the wafer profile becomes a concave profile. When the tilt angle $\alpha = 5\times10^{-3}[°], \beta = 5\times10^{-3}[°]$, the wafer profile shaped as convex profile. Fig. 3.15 clearly shows that experimental results are quite same as the mathematically analyzed results. It also reveals that our proposed grinding dynamics model could accurately

analyze wafer profile in rotary in-feed grinding and be used as a guidance to predict TTV and optimize grinding conditions for wafer manufacturing.

An example is shown in Fig. 3.16, where $\alpha = 6 \times 10^4 [°], \beta = 1 \times 10^3 [°]$ is preset to achieve the minimum TTV for the machine and wheel used in the experiment. According to
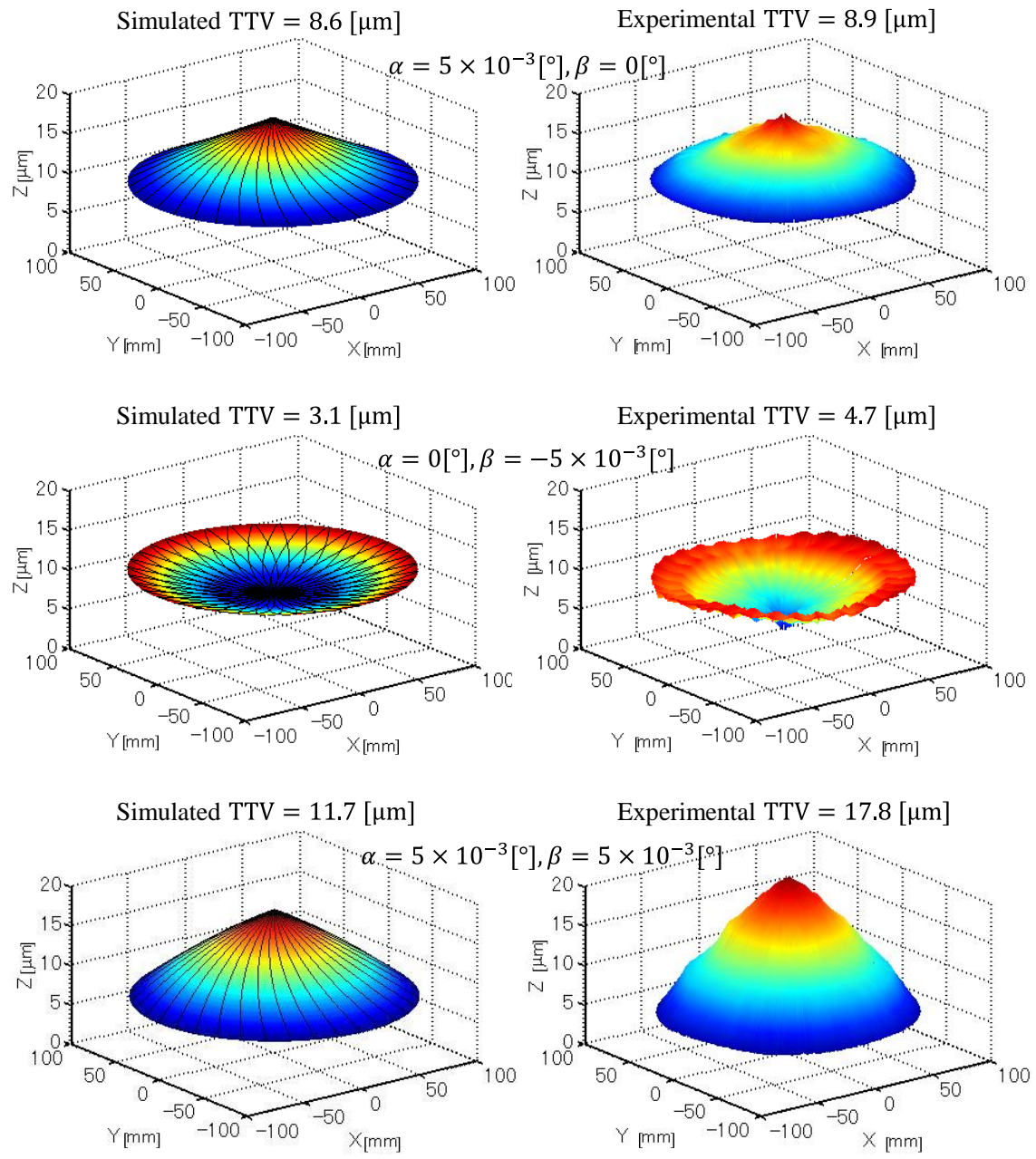

Fig. 3.15 The comparison of TTV in simulation and experimental results

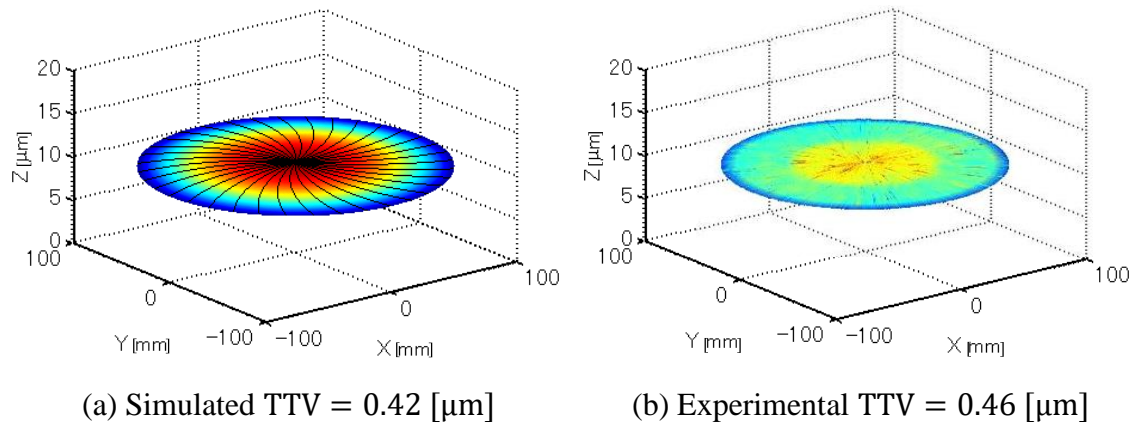(a) Simulated TTV = 0.42 [μm]   (b) Experimental TTV = 0.46 [μm]

Fig. 3.16 Wafer profile at optimal grinding conditions

tilt angles and experimental conditions mentioned above, TTV = 0.42 [μm] is suggested by
our dynamics model and resulted in 0.46 [μm] in our experiment.

3.6 Summary

In this chapter, efforts have been paid to kinematic analysis of cutting path and understand
the wafer profile generation in the rotary in-feed grinding dynamics. The influential factors
for rotary in-feed grinding have been mathematical studied and validated by experiment
results. The obtained results are able to be summarized as below:

1) The motion and path of cutting edge in rotary in-feed grinding are kinematically
   analyzed in three-dimensions, successfully to address the behavior of each abrasive
   in generation of the wafer profile.

2) The results mathematically reveal the effects of wheel specifications, grinding
   conditions and wheel/wafer configurations on the wafer geometry, particularly
   including the offset distance between the axes of wheel and wafer, the tilt angles of
   wafer axis and the diameter of the wheel.

3) The effects of both cutting path density and machine stiffness on the wafer profile are
   assessed. It is strongly recommended to use a grinding machine with a higher rigidity,
   a higher speed ratio, a finer abrasive to achieve a better wafer profile.

46

4) The grinding dynamic model also provides a solution using tilt angle α, β to counterbalance the effect of machine stiffness and cutting path density on the wafer geometry.

Reference

[1] Pei Z.J., Billingsley S.R., Miura S., (1999), Grinding induced subsurface cracks in silicon wafers, International Journal of Machine Tools and Manufacture, Vol.39, No. 7, pp. 1103-1116.

[2] Zhou L.B., Eda H., Shimizu J., (2002), State-of-the-art technologies and kinematical analysis for one-stop finishing of ϕ300 mm Si wafer, Journal of Materials Processing Technology, Vol. 129, No. 1-3, pp. 34-40.

[3] Zhou L.B., Shinohara K., Shimizu J., Eda H., (2002), Kinematics of ultra precision grinding for large scale Si wafer, Precision Engineering, Vol. 68, No. 1, pp. 125-129 (in Japanese).

[4] Zhou L.B., Shimizu J., Shinohara K., Eda H., (2003), Three-dimensional kinematical analyses for surface grinding of large scale substrate, Precision Engineering, Vol. 27, No. 2, pp. 175-184.

[5] Chen C.C.A., Hsu L.S., (2008), A process model of wafer thinning by diamond grinding, Journal of Materials Processing Technology, Vol. 201, No. 1, pp. 606-611.

[6] Ebina Y., Yoshimatsu T., Zhou L.B., Shimizu J., Onuki T., Ojima H., (2015), Process study on large-size silicon wafer grinding by using a small-dimeter wheel, Journal of Advanced Mechanical Design, Systems, and Manufacturing, Vol. 9, No. 5, pp. jamdsm0073.

[7] Lu W., Zhou L., Shimizu J., Onuki T., Ojima H., Yamamoto T., (2020), Material removal mechanism in rotary in-feed grinding - Modeling and analysis -, Journal of Advanced Mechanical Design, Systems, and Manufacturing, Vol. 14, No. 6, pp. jamdsm0095.

[8] Zhou L.B., Mitsuta T., Shimizu J., Tian Y.B., Yamamoto T., (2010), Effects of machine tool stiffness and cutting path density on infeed face grinding of silicon wafer 1st Report: Modeling and analysis, Journal of the Japan Society for Abrasive Technology, Vol. 54, No. 1, pp. 45–49 (in Japanese).

[9] Kusuyama J., Iwahashi S., Kitajuma T., Ogasawara N., Yui A., Kitajima T., Saito H., Slocum A.H., (2015), Loop stiffness of grinding machine developed for 450 mm silicon wafers, Advanced Maerials Research, Vol. 1136, pp. 655-660.

[10] Kusuyama J., Honda A., Kitajuma T., Okahata G., Yui A., Ito T., Slocum A.H., (2016), Development of rotary table grinding machine for large diameter Si wafers (1st report: Performance investigation of water hydrostatic rotary table), Transactions of the JSME, Vol. 82, No. 842, pp. transjsme.16-00190 (in Japanese).

[11] Kusuyama J., Honda A., Kitajuma T., Okahata G., Yui A., Ito T., Slocum A.H., (2017), Development of rotary table grinding machine for large diameter Si wafers (2nd report: Performance investigation of wheel spindle designed to govern infeed

motion), Transactions of the JSME, Vol. 83, No. 852, pp. transjsme.17-00102 (in Japanese).

[12]   Zhou L.B., Ebina Y., Wu K., Shimizu J., Onuki T., Ojima H., (2017), Theoretical analysis on effects of grain size variation, Precision Engineering, Vol. 50, pp. 27–31.

[13]   Zhou L.B., Mitsuta T., Shimizu J., Tian Y.B., Yamamoto T., (2010), Effects of machine tool stiffness and cutting path density on infeed face grinding of silicon wafer 2nd Report: Empirical study, Journal of the Japan Society for Abrasive Technology, Vol. 54, No. 2, pp. 92–96 (in Japanese).

Chapter 4 Wafer topography and surface roughness

In this chapter, attention has been paid to modelling and experimental study of the surface roughness in rotary in-feed grinding, where influential factors are categorized into grinding wheel specifications, wafer specifications and grinding conditions.

The surface topography on the wafer surface is associated with the chip formation which largely depends on distribution of abrasive protrusion in height-wise. The mathematical analysis results suggest that the depth of cut should be adequate to ensure sufficient cutting edge being effective for reducing the surface roughness. Moreover, both theoretical analysis and experiments results lead to a fact that the surface roughness becomes larger toward to the outer circumference of the wafer, but smaller as increasing in the speed ratio n_1/n_2.

4.1 Theoretical analysis of chip formation

As we known, the surface roughness is an important indicator for assessing the grinding

(a) Depth of cut and removed volume   (b) Side removal area in a ground annulus

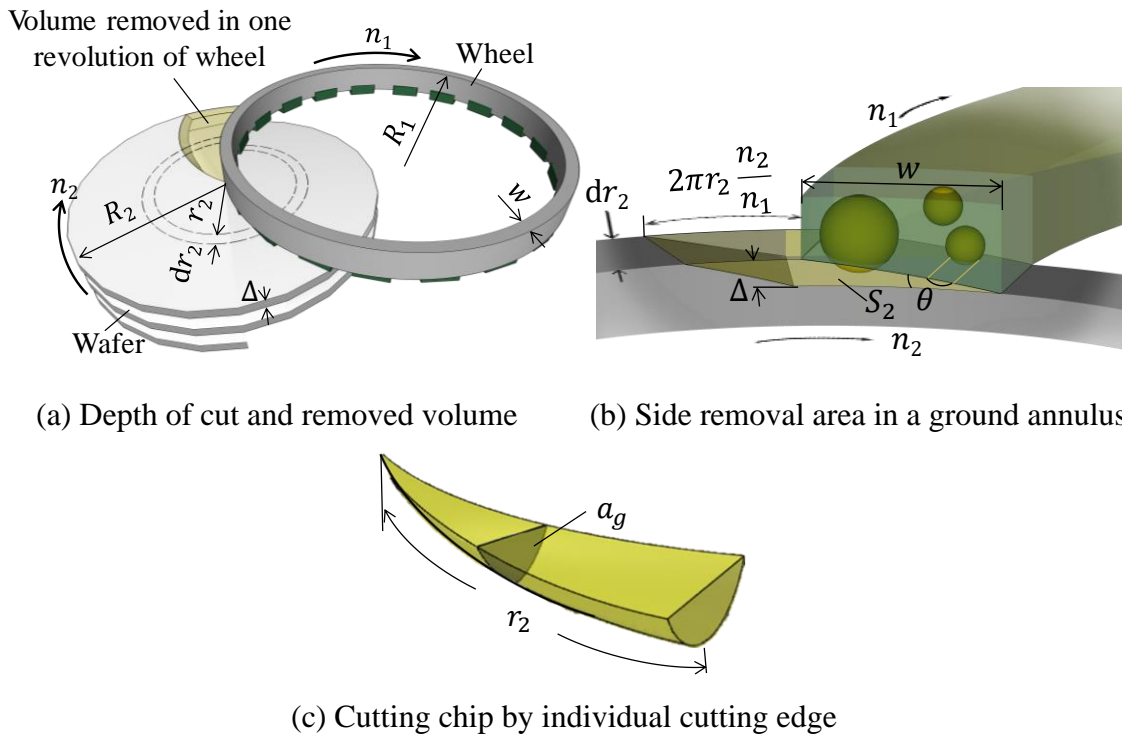(c) Cutting chip by individual cutting edge

Fig. 4.1 Chip generation

quality and performance which is used to characterize the material removal mode in the grinding process. In ductile-mode machining of mono-crystal materials, material is removed predominantly by the chip formation to generate a crack-free machined surface. The generation of chip formation in rotary in-feed grinding is schematically shown in Fig. 4.1, and the relevant parameters are labeled in Table 4.1. The shadow band illustrated in Fig. 4.1 (a) represents the volume removed in one rotation of the grinding wheel, where the depth of cut is $\Delta = f/n_2$ and the travel length is $L = 2\pi r_2 n_2/n_1$. It is clear that the depth of cut is kept constant once the grinding conditions are given. Here, the wafer is considered as a collected concentric annulus with different radius r_2. One annulus positioned at $[r_2, r_2 + dr_2]$ is zoomed up in Fig. 4.1 (b) for the detailed study. The side area of the annulus S_2 removed in one rotation of the wheel is expressed as Eq. (4-1).

$$S_2 = \Delta \cdot L = 2\pi \frac{f}{n_1} r_2 = 2\pi \cdot \frac{n_2}{n_1} \cdot \Delta \cdot r_2 \tag{4-1}$$

The side area S_2 is proportional to the wafer radial distance r_2, the depth of cut Δ and

Table 4.1 The symbols used for the rotary in-feed grinding dynamic model description and the following analysis

|			
Wheel specifications	ζ	Segment ratio	—
	σ	Standard deviation of the abrasive radius	[μm]
	m	Cut-off coefficient	—
	2γ	Abrasive vertex angle	[°]
Wafer specifications	Cp	Specific grinding energy	[MPa]
Symbols used for evaluations	N_0	Density of effective cutting edge exposed on the bond base	[practial/mm^2]
	N_e	Density of effective cutting edge	[practial/mm^2]
	S_2	Side area of ground wafer	[mm^2]
	a_g	Size of chip cross section	[μm^2]
	R_z	Maximum surface roughness	[nm]
	R_a	Mean surface roughness	[nm]
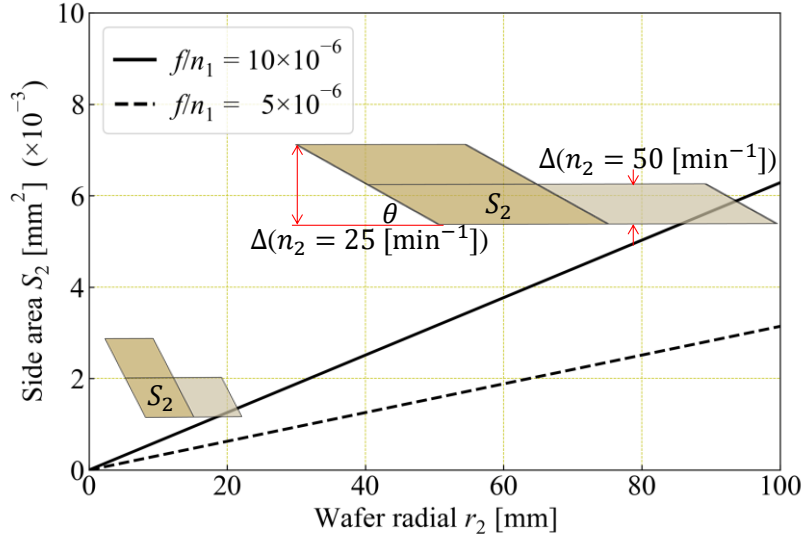
Fig. 4.2 Side area of material removed and depth of cut

n_2/n_1 (or reverse of speed ratio), as shown in Fig. 4.2. It should be noted that the wafer rotational speed n_2 does not affect the size of S_2, but does affect its geometric shape. As illustrated in Fig. 4.1 (b) and Fig. 4.2, increasing in n_2 leads to a long and thin shape of S_2 while keeps the area of S_2 unchanged. According to the principle of continuity, S_2 is shared by the number of effective cutting edges $j = 2\pi R_1 w \cdot N_e$ which are evenly distributed across the wheel working surface, where w is the width of wheel segment, N_e is the density of effective cutting edge. Therefore, the chip cross section removed by an individual abrasive cutting edge at the wafer radial distance r_2 is given below;

$$a_g = \frac{S_2}{j} = \frac{1}{R_1 w N_e} \frac{n_2}{n_1} \Delta \cdot r_2 \tag{4-2}$$

Also, the chip volume q_g and average chip cross section area $\bar{a}_g$ are then given below;

$$q_g = \int_0^{R_2} a_g \mathrm{d}r_2 = \frac{1}{2w N_e} \frac{R_2^2}{R_1} \cdot \frac{n_2}{n_1} \Delta \tag{4-3}$$

$$\bar{a}_g = \frac{1}{R_2} \int_0^{R_2} a_g \mathrm{d}r_2 = \frac{1}{2w N_e} \frac{R_2}{R_1} \cdot \frac{n_2}{n_1} \Delta \tag{4-4}$$

As shown in Eq. (4-2) and Fig. 4.1 (c), the chip cross section a_g proportionally increases with r_2 as the abrasive goes from the wafer center to its outer periphery. Here, the effective cutting edge density N_e is an important factor to determine the chip cross section a_g, which was predicable in a mathematic method proposed by Zhou et al. [1].
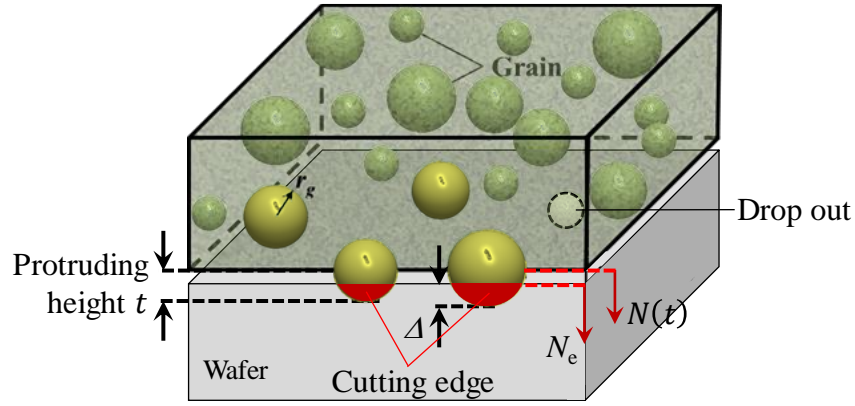
Fig. 4.3 Cutting edge exposed on the wheel working surface

For theoretical analysis of the number of cutting edge and its protrusion distribution on grinding wheel surface, as illustrated in Fig. 4.3, the modelling of wheel working surface is based on following assumptions:

1) The bond base is built in ideally flat.
2) Abrasives are uniformly distributed in the wheel segment within three-dimensional space.
3) Abrasives are approximated into spheres with radius r_g.
4) r_g varies in accordance with a normal distribution (r_0, σ), where r_0 is the mean abrasive radius, and σ is the standard deviation of the abrasive radius, respectively.
5) The abrasive drops out when its protrusion height t exceeds $2\kappa r_g$ from the bond base, where κ takes a value of $0 \leq \kappa < 1$ and stands for the protruding coefficient.

In this context, the abrasive variation is able to be expressed by a normal distribution as Eq. (4-5).

$$f(r_g) = \frac{1}{\sqrt{2\pi}\sigma} \exp\left[-\frac{(r_g - r_0)^2}{2\sigma^2}\right] \tag{4-5}$$

Practically, the size of abrasives is further filtrated within the range of $r_0 - m\sigma < r_g < r_0 + m\sigma$, where m is the cut-off coefficient and $m = 1$ is favored by most wheel manufacturers. Therefore, the abrasive size distribution is governed by two factors; the standard deviation σ and the cut-off coefficient m. The average volume $\bar{V}$ of an individual

spherical abrasive is expressed by Eq. (4-6).

$$\bar{V} = \frac{4}{3}\pi \frac{\int_{r_0-m\sigma}^{r_0+m\sigma} r_g^3 f(r_g) \mathrm{d}r_g}{\int_{r_0-m\sigma}^{r_0+m\sigma} f(r_g) \mathrm{d}r_g} = \frac{4}{3}\pi r_0^3 + 4\pi \left[1 - \frac{\frac{m}{\sqrt{2}}\exp\left(-\frac{m^2}{2}\right)}{1-\mathrm{erfc}\left(\frac{m}{\sqrt{2}}\right)} \right] \tag{4-6}$$

where the erfc( ) is the complementary error function.

When the position of bond base is set to $Z = 0$, an abrasive with radius r_g whose center is located within the range of $-r_g < Z < (2\kappa - 1)r_g$ is expected to be exposed above and remains on the bond base. Here, the protrusion coefficient κ is in fact the fraction of abrasive which possibly remains on the grinding wheel surface. Among those exposed abrasives, the number of abrasives having the radius $[r_g, r_g + \mathrm{d}r_g]$ is given as;

$$\mathrm{d}N_0 = \frac{2\kappa V_g}{\bar{V}} \cdot \frac{f(r_g)\mathrm{d}r_g}{\int f(r_g)\mathrm{d}r_g} \tag{4-7}$$

where V_g is the volume fraction of abrasive in a grinding wheel.

Thus, the total number N_0 of abrasives exposed and remaining on a specific working surface area (per unit area) is the integration of $\mathrm{d}N_0$ within the domain $r_0 - m\sigma < r_g < r_0 + m\sigma$ and expressed in Eq. (4-8).

$$N_0 = \frac{2\kappa V_g}{\bar{V}} \frac{\int_{r_0-m\sigma}^{r_0+m\sigma} r_g^3 f(r_g) \mathrm{d}r_g}{\int_{r_0-m\sigma}^{r_0+m\sigma} f(r_g) \mathrm{d}r_g} = \frac{3\kappa V_g}{2\pi r_0^2} \cdot \frac{1}{1+3\left[1 - \frac{\sqrt{\frac{2}{\pi}}m\cdot\exp\left(-\frac{m^2}{2}\right)}{1-\mathrm{erfc}\left(\frac{m}{\sqrt{2}}\right)}\right]\left(\frac{\sigma}{r_0}\right)^2} \tag{4-8}$$
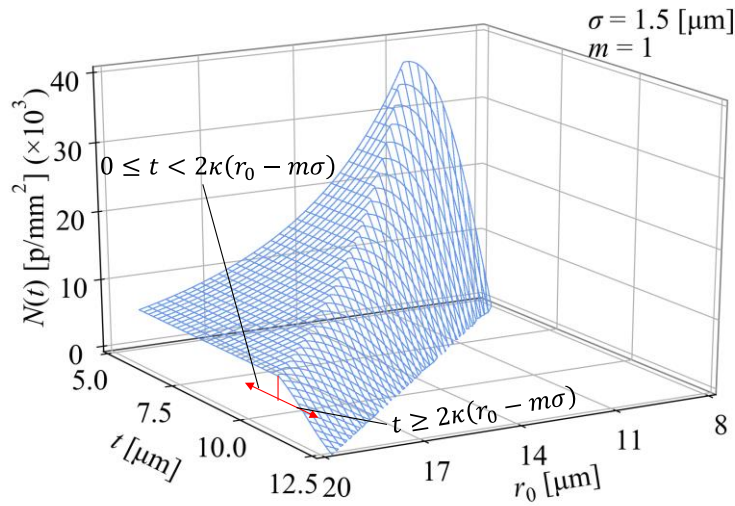

Fig. 4.4 Cutting edge density exposed on the wheel working surface

54

However, the abrasives remaining on the bond base vary not only in the radius r_g but also in the protrusion height t above wheel bond base. The codomain of abrasive radius is limited to $t/2\kappa < r_g < r_0 + m\sigma$ in order to satisfy the protrusion height t. Therefore, the probability of abrasives concurrently satisfying $r_g \sim r_g + \mathrm{d}r_g$ and $t \sim t + \mathrm{d}t$ are able to be calculated by Eq. (4-9).

$$P(r_g, t)\mathrm{d}r_g\mathrm{d}t = \frac{\mathrm{d}N_0}{N_0} \cdot \frac{\mathrm{d}t}{2\kappa r_g} = \frac{1}{2\kappa r_0}\frac{f(r_g)\mathrm{d}r_g}{\int f(r_g)\mathrm{d}r_g}\mathrm{d}r_g\mathrm{d}t \tag{4-9}$$

Therefore, the possibility $P(t)$ of protrusion height t for all sizes of abrasives is the integration of $P(r_g, t)$ within the codomain of r_g. The number of abrasives $N(t)$ which possess the protrusion height t is therefore the product of $P(t)$ and N_0, and can be written as Eq. (4.10).

$$N(t) = N_0 \cdot P(t) = N_0 \cdot \int_{t/2\kappa}^{r_0+m\sigma} P(r_g, t)\mathrm{d}r_g\mathrm{d}t =$$

$$\begin{cases} \dfrac{3V_g}{4\pi r_0^3}\dfrac{1}{1+3\left[1-\dfrac{\sqrt{\frac{2}{\pi}}m\cdot\exp\left(-\frac{m^2}{2}\right)}{1-\mathrm{erfc}\left(\frac{m}{\sqrt{2}}\right)}\right]\left(\frac{\sigma}{r_0}\right)^2} & \left(0 \le t < 2\kappa(r_0 - m\sigma)\right) \\[3em] \dfrac{3V_g}{8\pi r_0^3}\dfrac{1}{1+3\left[1-\dfrac{\sqrt{\frac{2}{\pi}}m\cdot\exp\left(-\frac{m^2}{2}\right)}{1-\mathrm{erfc}\left(\frac{m}{\sqrt{2}}\right)}\right]\left(\frac{\sigma}{r_0}\right)^2}\dfrac{\mathrm{erfc}\left(\frac{t-2\kappa r_0}{2\sqrt{2}\sigma\kappa}\right)-\mathrm{erfc}\left(\frac{m}{\sqrt{2}}\right)}{1-\mathrm{erfc}\left(\frac{m}{\sqrt{2}}\right)} & \left(t \ge 2\kappa(r_0 - m\sigma)\right) \end{cases} \tag{4-10}$$

Fig. 4.4 shows the effects of protrusion height t and abrasive radius on the number of total cutting edge $N(t)$ exposed on wheel working surface. Obviously, it is found out that the number of total cutting edges $N(t)$ is decreased as increasing in abrasive radius r_0. At a given r_0, the number of abrasives $N(t)$ is constant when the protrusion height t ranges $0 \le t < 2\kappa(r_0 - m\sigma)$, and rapidly dropped to zero when $t \ge 2\kappa(r_0 - m\sigma)$.

Fig. 4.5 shows the normalized variation of $N(t)$ for three kinds of wheels with different standard deviation σ in the distribution of protrusion height t. Clearly, only those abrasives which have top protrusion possibly become effective to engage into material. The amount of these effective cutting edges can be calculated by integration of $N(t)$ within the range of $t_{\max} - \Delta < t < t_{\max}$ which is illustrated by a light shade in Fig. 4.5 and expressed in Eq. (4-8).
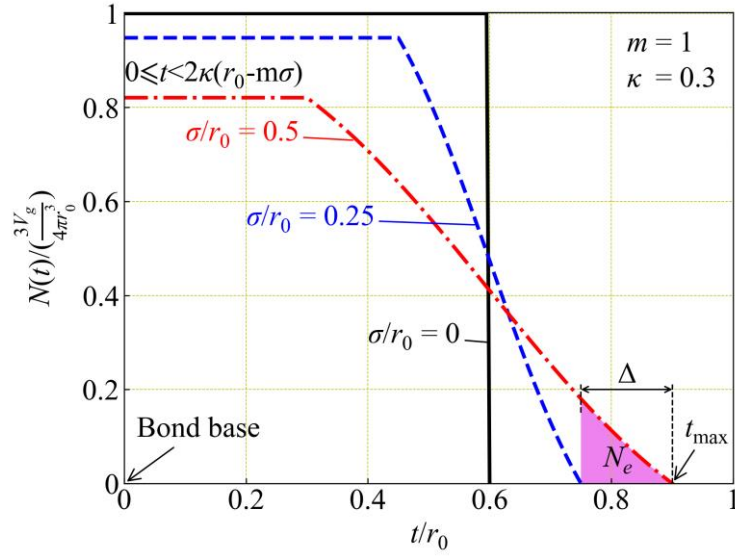
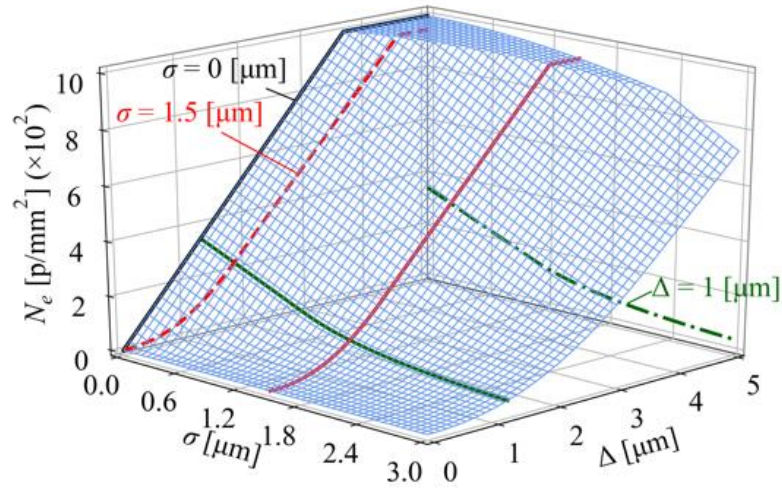Fig. 4.5 Protrusion height distribution and effective cutting edge

Fig. 4.6 Effective cutting edge density N_e

$$N_e(\Delta) = \int_{t_{\max}-\Delta}^{t_{\max}} N(t)\mathrm{d}t \tag{4-11}$$

where $t_{\max} = 2\kappa(r_0 + m\sigma)$ for a given protrusion coefficient κ and abrasive radius distribution $m\sigma$. For most rotary in-feed grinding as shown in Fig. 4.1, Δ ranges from submicron to several microns, depending on the in-feed rate f and the wafer rotational speed n_2. Therefore, only a fraction of abrasive at the top protrusions are possibly engaged in
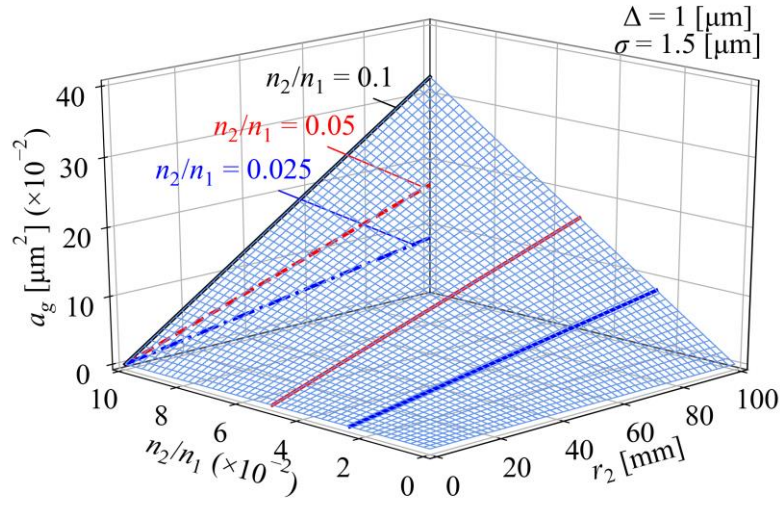
Fig. 4.7 Cross sectional area of individual chip

material removal and become effective cutting edges. For such a wheel $\big(R_1 = 150 \text{ [mm]}, w = 3 \text{ [mm]}, V_g = 25 \text{ vol\%}, r_0 = 6 \text{ [µm]}, \sigma = 1.5 \text{ [µm]}, \kappa = 0.3 \big)$, the total cutting edge exposed on the working surface N_0 is about $1000 \text{ [p/mm}^2]$. The effective cutting edge density N_e is calculated and shown in Fig. 4.6. Depending on the depth of cut $\Delta = f/n_2$ and standard deviation σ in the distribution of abrasive size, N_e ranges $20\sim200 \text{ [p/mm}^2]$, or about $2\%\sim20\%$ of the total.

Using the above N_e, the chip cross section area a_g is calculated as a function of $(r_2, n_2/n_1)$. The results for $\Delta = 1 \text{ [µm]}$ is shown in Fig. 4.7. The chip cross section by an individual abrasive cutting edge increases linearly with an increasing in both n_2/n_1 and wafer radial distance r_2. Choosing a large speed ratio n_1/n_2 effectively constrains the chip cross section.

4.2 Theoretical analysis for surface roughness

For evaluating the surface roughness, following assumptions are made:

1) The effect of brittle model on surface roughness is not considered, the depth of cut is always under the critical depth of cut [2-4].

2) The elastic recovery of the wafer is neglected [5].

A simplified model of surface topography generated on a ground wafer surface is illustrated in Fig. 4.8. Assuming the vertex angle of an abrasive is 2γ, the penetration depth of the abrasive into the wafer can be easily derived once the chip cross section a_g is known.
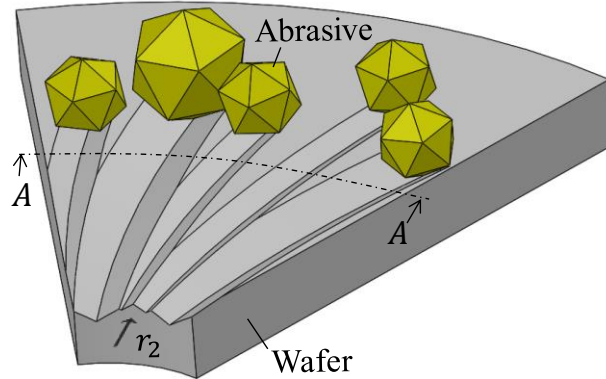
(a) The generated ground wafer surface
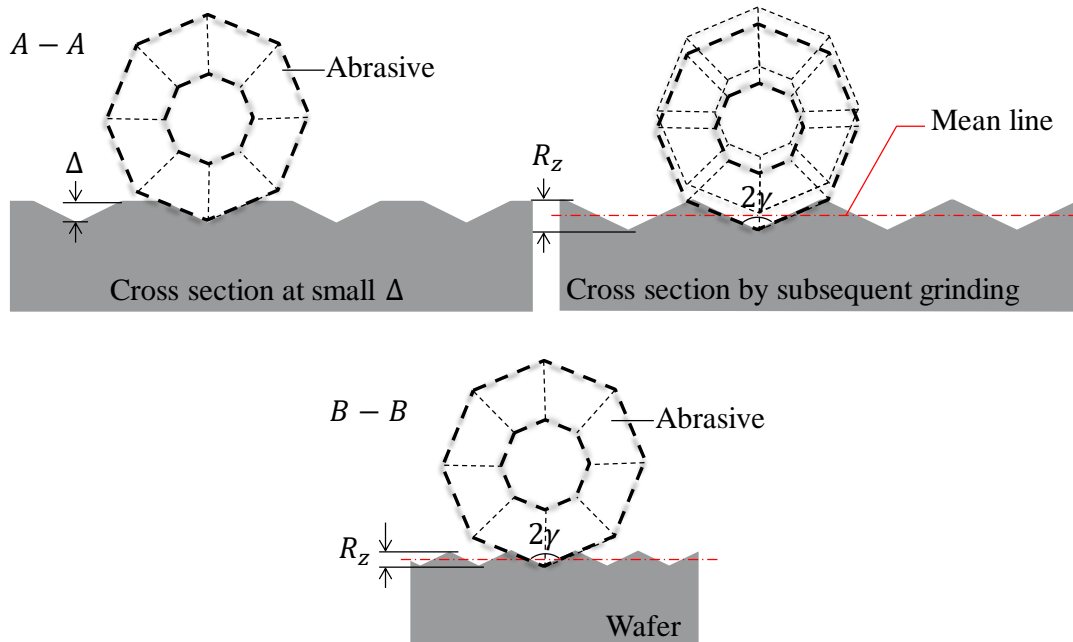
(b) The cross section of grinding path

Fig. 4.8 Illustration of the surface topography

$$\frac{1}{2}R_z \cdot 2R_z \tan\gamma = a_g \qquad\qquad (4\text{-}12)$$

Substituting Eq. (4-2) into Eq. (4.12), the surface roughness can be solved as;

$$R_z = \sqrt{\frac{1}{\tan\gamma R_1 w} \cdot \frac{n_2}{n_1} \cdot \frac{\Delta}{N_e} \cdot r_2} \qquad\qquad (4\text{-}13)$$

It must be pointed out that R_z in Eq. (4-12) is governed by the cross section a_g, while a_g in Eq. (4-2) is the averaged cross section at the radial distance r_2 without counting the
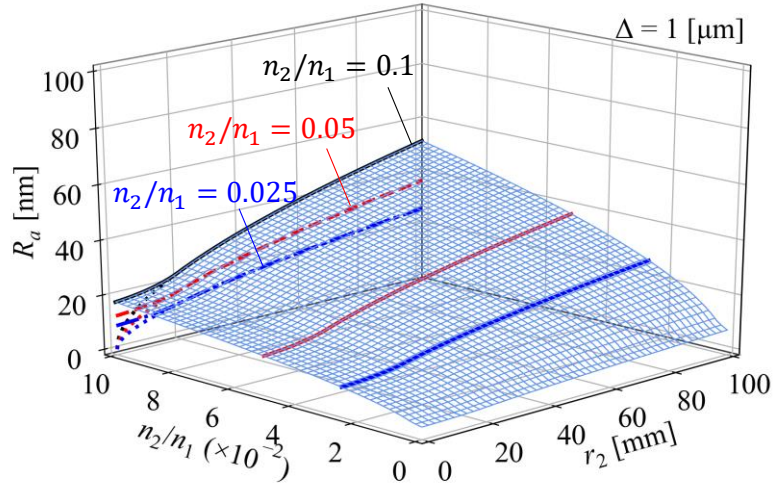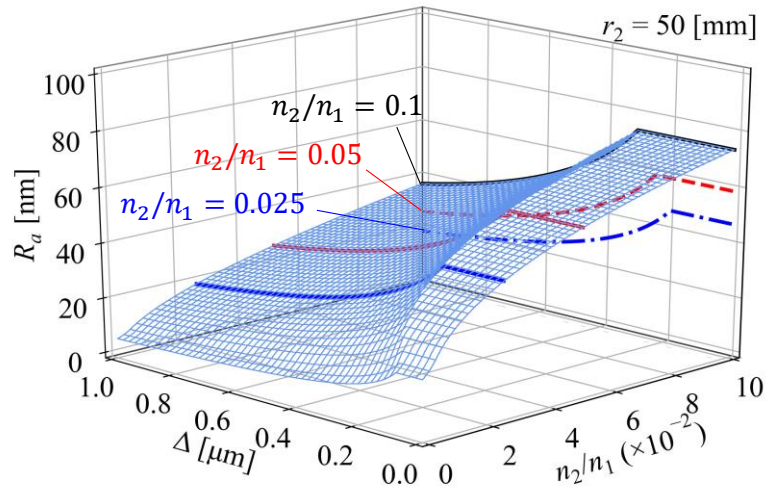

Fig. 4.9 Effect of n_2/n_1 and r_2 on R_z

Fig. 4.10 Effect of n_2/n_1 and Δ on R_z

59

variation in the abrasive radius and protrusion height. Therefor, R_z in Eq. (4-13) is a sort of equalized maximum surface roughness, slightly smaller than that defined by ISO.

For such triangularly waved topography, the mean line roughness average R_a is given as;

$$R_a = \frac{1}{L}\left(\frac{1}{2}L \cdot \frac{R_z}{2}\right) = \frac{1}{4}R_z \qquad (4\text{-}14)$$

where, L is the evaluation length. At the wafer center where the wafer radial distance $r_2 \rightarrow 0$, in addition, K. Ono suggested that the surface roughness should take its ultimate limit [6]. The surface roughness R_a calculated at $\Delta = 1$ [μm] is plotted in Fig. 4.9, as a function of $(r_2, n_2/n_1)$. The results suggest that the surface roughness becomes larger as increasing in the radial distance r_2 and takes the maximum value of $R_a = \Delta/4$ if the cutting path density $\eta < 1$ occurs at the outer circumference of the wafer, but smaller as decreasing in n_2/n_1. The surface roughness R_a calculated at $r_2 = 50$ [mm] while Δ and n_2/n_1 varies is shown in Fig. 4.10. The results tell that inadequate depth of cut Δ may not improve the surface roughness due to the insufficient effective cutting edge (Fig. 4.6). Especially when Δ is extremely small ($\Delta < 0.2$ [μm] for the current condition), as illustrated in Fig.4.8 (b), the wafer surface may not be completely removed in one rotation of the grinding wheel. The subsequent grinding still makes the surface roughness remain relatively high. Finally, it should also be noted that the Eq. (4-13) does not include the elastic recovery of the wafer after grinding, which could counter up to 40% ~ 60% of the depth of cut according to publication [5].

4.3 Experiments and results

Based on the analysis mentioned above, the experiments were carried out on a horizontal type rotary in-feed precision grinding machine (UPG-150) which is able to perform grinding process under either constant in-feed rate or constant pressure. Fig. 4.11 shows its external view together with the zoom-up of $\varnothing 200$ [mm] Si wafer and the diamond wheel (SD1500N75B) are mounted. SD1500N75B is potential to achieve ductile dominated removal. The detailed specifications of SD1500N75B and experiment conditions are listed in Table 4.2. After the grinding process, the ground Si wafer was cleaned by pure water in an ultrasonic cleaning machine (UT-305S, Sharp Co.) and then dried off for measurement.

The surface topography of Si wafers was measured and observed by white-light

Wafer-wheel alignment
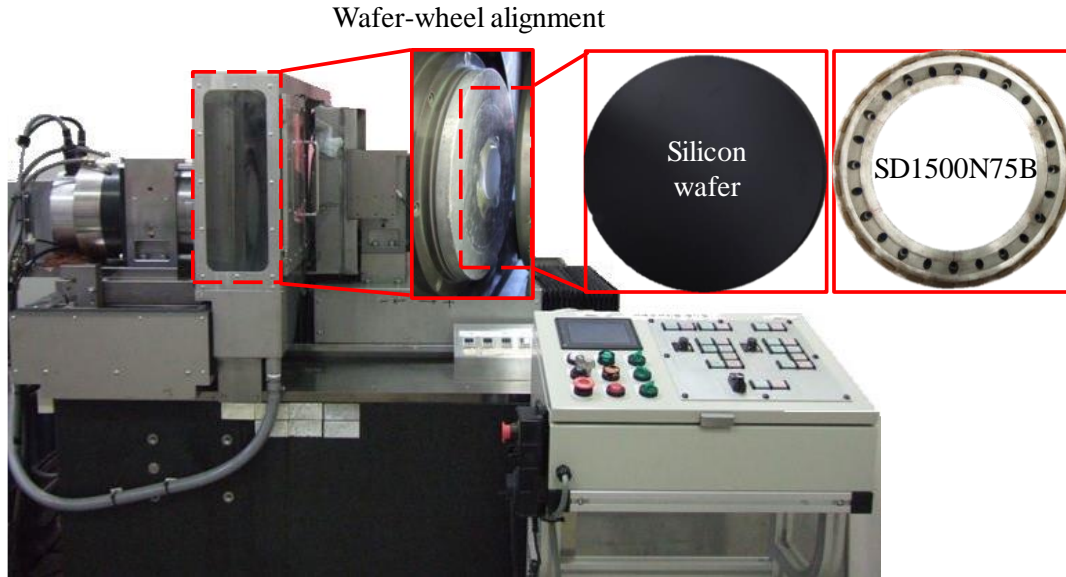
Fig. 4.11 Experiment tool and setup

Table 4.2 Detailed specifications of SD1500N75B and experiment conditions

Wheel specifications	Grinding wheel	−	SD1500N75B	−
	Wheel hardness	−	2	[GPa]
	Average abrasive radius	r_0	5	[μm]
	Number of segments	n	24	[pratical]
	Wheel size	$l \times w$	17×3	[mm^2]
	Wheel radius	R_1	150	[mm]
Wafer specifications	Wafer	−	Si	−
	Wafer radius	R_2	100	[mm]
Grinding conditions	Wheel speed	n_1	1500, 2000, 2500	[min^{-1}]
	Wafer speed	n_2	25	[min^{-1}]
	In-feed rate	f	10	[μm/min]
	Total in-feed depth	−	60	[μm]
	Coolant	−	6	[l/min]

interferometer (NewView-200, Zygo Co.). Six points were uniformly distributed from center to periphery for a Si wafer to study.

Fig. 4.12 shows surface roughness under conditions of $n_2 = 25$ [min^{-1}] and $f = 10$ [μm/min] when n_1 varying in $n_1 = 1500\sim2500$ [min^{-1}]. The surface roughness reveals that the surface topography produced by higher wheel rotational speed is much better

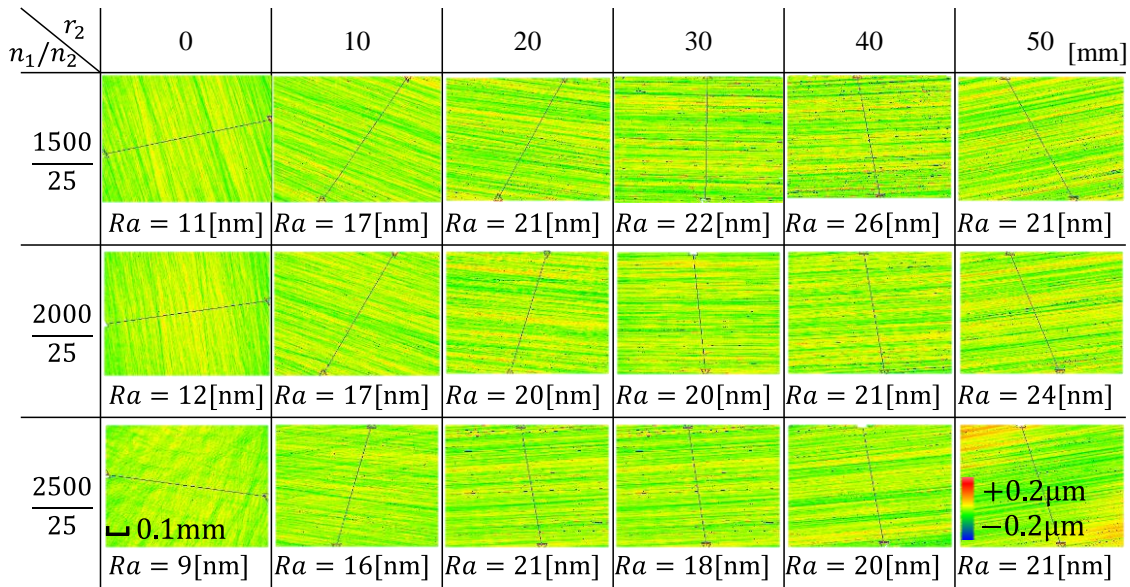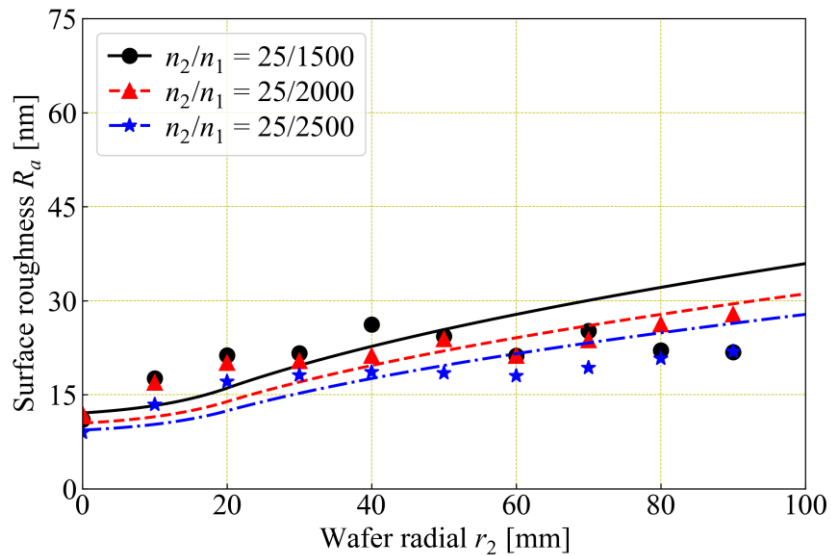| n_1/n_2 \ r_2	0	10	20	30	40	50 [mm]
$\frac{1500}{25}$	$Ra = 11$[nm]	$Ra = 17$[nm]	$Ra = 21$[nm]	$Ra = 22$[nm]	$Ra = 26$[nm]	$Ra = 21$[nm]
$\frac{2000}{25}$	$Ra = 12$[nm]	$Ra = 17$[nm]	$Ra = 20$[nm]	$Ra = 20$[nm]	$Ra = 21$[nm]	$Ra = 24$[nm]
$\frac{2500}{25}$	$Ra = 9$[nm]	$Ra = 16$[nm]	$Ra = 21$[nm]	$Ra = 18$[nm]	$Ra = 20$[nm]	$Ra = 21$[nm]

Fig. 4.12 Experimental results

Fig. 4.13 Comparison of experimental and theoretical results

than that of lower wheel rotational speed.

The comparison of experimental and theoretical results is shown in Fig. 4.13. Both experimental and theoretical results clearly show that the surface roughness is proportional to r_2 and n_2/n_1. It also reveals that our proposed grinding dynamics model could accurately analyze wafer topography in rotary in-feed grinding and be used to predict surface roughness and optimize grinding conditions for wafer manufacturing.

4.4 Summary

This chapter analyzes chip formation and associates chip cross section to surface roughness which principally depends on distribution of abrasive protrusion in height-wise. The influential factors of rotary in-feed grinding process for wafer topography have been mathematical studied and validated by experiment result. The obtained results could be summarized as below:

1) The side removal area and chip cross section are analyzed to understand the chip formation and associated with grinding conditions and wheel specifications.

2) The effective cutting edge density was estimated by taking into consideration of the distribution of abrasive protrusion in height-wise, which helps to precisely predict the chip cross section and surface roughness.

3) The surface roughness and its variation in a radial direction of the wafer were derived and discussed on varying grinding conditions. The depth of cut should be adequate to ensure sufficient cutting edge being effective.

4) The effect of n_2/n_1 on the surface roughness is assessed. It is suggested to use a high speed ratio n_1/n_2 to achieve a better wafer surface.

5) Inadequate depth of cut Δ does not help to improve the surface roughness due to the insufficient effective cutting edge.

Reference

[1] Zhou L.B., Ebina Y., Wu K., Shimizu J., Onuki T., Ojima H., (2017), Theoretical analysis on effects of grain size variation, Precision Engineering, Vol. 50, pp. 27–31.

[2] Tönshoff H.K., Schmieden W.v., Inasaki I., König W., Spur G., (1990), Abrasive Machining of Silicon, Annals of the CIRP, Vol. 39, No. 2, pp. 621- 635.

[3] Bifano T.G., Dow T.A., Scattergood R.O., (1991), Ductile-regime grinding: a new technology for machining brittle materials, Journal of engineering for industry, Vol. 113, No. 2, pp. 184-189.

[4] Zhang B., Dow T.A., (1994), Material-Removal Mechanisms in Grinding Ceramics, Annals of the ClRP, Vol. 43, No. 1, pp. 305-308.

[5] Huang Ning, Yan Ying, Zhou Ping, Kang Renke, Guo Dongming, Saurav Goel., (2020), Elastic recovery of monocrystalline silicon during ultra-fine rotational grinding, Precision Engineering Vol. 65, pp. 64-71.

[6] Ono K., (1962), Grinding finishing., Maki-syoten, pp. 80 (in Japanese).

Chapter 5 Static and dynamic analysis for rotary in-feed grinding

Both theoretical analysis and experiment results in previous chapter unveil that optimization in grinding conditions is of potential to efficiently improve the ground wafer surface quality. On the other hand, the subsurface quality or subsurface damage (SSD) induced in rotary in-feed grinding is the consequence of the grinding force and grinding heat in the material removal operation. Thus, static and dynamic analysis of rotary in-feed grinding is essential to understand the SSD formation.

A thorough analysis on the relationships between the chip formation and grinding forces will be analyzed in this chapter. The grinding force exerted on an individual abrasive is first correlated to the chip cross section and then extended to a single wheel segment and the whole wafer. Meanwhile, a wireless thermo/dynamo-meter is developed and applied to measure the grinding force and grinding temperature during the grinding process. Both mathematical and experimental results show that the grinding force on a wheel segment was proportional to the wheel segment length, gradually grew along the wafer radial distance, and rapidly dropped to zero when the wheel segment exited from the wafer periphery. Moreover, it should be point out that the rigidity and the spindle power of grinding machine were important when grinding large diameter wafers.

5.1 Static analysis

The grinding dynamic is schematically shown in Fig. 5.1, where the grinding force is composed of two components; the normal grinding force F_n and tangential force F_t when the wheel segment is engaged in material removal. The other symbols used are listed in Table 5.1. As per each individual abrasive (as zoomed in the right panel of Fig. 5.1), the grinding force f_t in the tangential direction (along cutting path) is the product of the specific removal energy Cp and chip cross-section a_g and shown as below.

$$f_t = Cp \cdot a_g \tag{5-1}$$

Substituting a_g which is obtained in the Eq. (4-2) in the previous chapter, the tangential

force f_t on an individual abrasive is written below;

$$f_t = Cp \cdot \frac{1}{R_1 \cdot w \cdot N_e} \cdot \frac{f}{n_1} \cdot r_2 = \frac{Cp}{R_1 w N_e} \frac{n_2}{n_1} \Delta \cdot r_2 \tag{5-2}$$

Here, Eq. (5-2) addresses that the tangential force f_t not only is affected by the grinding
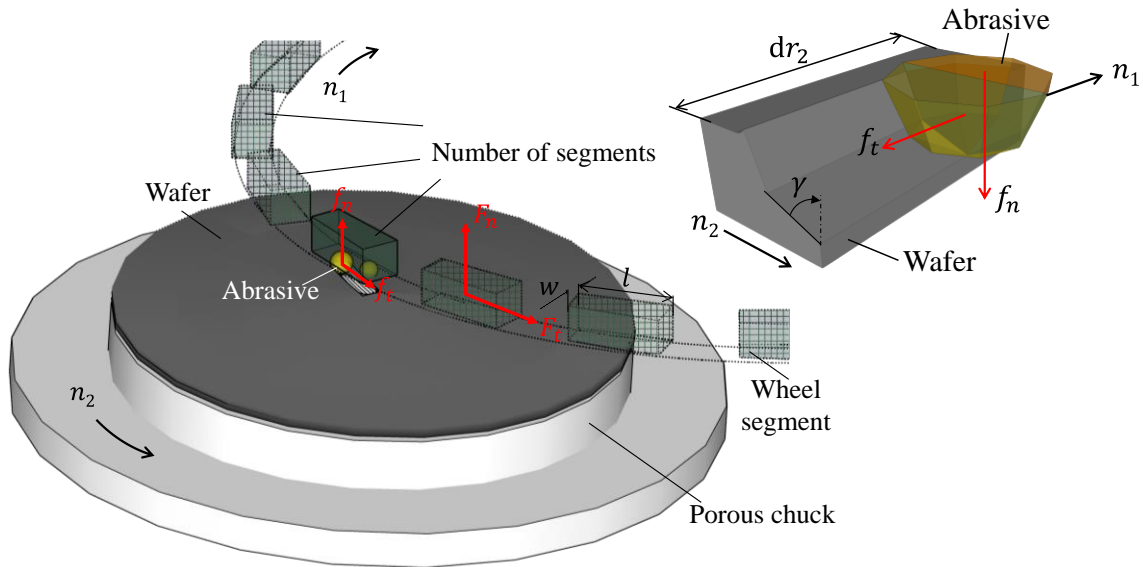

Fig. 5.1 Illustration of grinding force components

Table 5.1 The symbols used for the rotary in-feed grinding dynamic model description
and the static analysis

Symbol	Description	Unit
$\acute{\mu}$	Friction coefficient	—
2γ	Abrasive vertex angle	[°]
f_n	Normal force on an individual abrasive	[mN]
f_t	Tangential force on an individual abrasive	[mN]
F_n	Normal force on a wheel segment	[N]
F_t	Tangential force on a wheel segment	[N]
P	Grinding power	[W]
q	Power density	[W/mm^2]

conditions n_2/n_1, Δ, but also by the wheel specifications R_1, w, N_e, the wafer material property Cp and the cutting position r_2 as well. It should be point out that the friction force is neglected here and will be discussed at the end of this section for the actual grinding process. Fig. 5.2 plots two sets of tangential force f_t appearing at different wheel rotational speed n_1, as a function of the grinding time τ. It is found that f_t is halved when the wheel speed n_1 is doubled. The iteration of f_t is also doubled in frequency. It should be emphasized that the specific removal energy Cp depends on not only the property of wafer material but also the size of a_g. A smaller a_g normally results in relatively larger Cp because of the "size effect".

Within the wafer annulus positioned at $[r_2, r_2 + dr_2]$ mentioned in Section 4.1, the sum of number of abrasives totally engaged in wafer annulus the is given as $N_e \cdot w \cdot dr_2$. Thus, the tangential grinding force on a wheel segment in length of l is calculated as Eq. (5-3).

$$F_t = \int_{r_2-l/2}^{r_2+l/2} f_t \cdot N_e w dr_2 = Cp \cdot \frac{l}{R_1} \cdot \frac{n_2}{n_1} \cdot \Delta \cdot r_2 \tag{5-3}$$

F_t is found to be proportional to the segment length l, the depth of cut Δ and n_2/n_1, and reversely proportional to the wheel radius R_1. By taking the effect at the wafer center and fringe, where the wheel segment is not fully contacted with the wafer, into consideration,
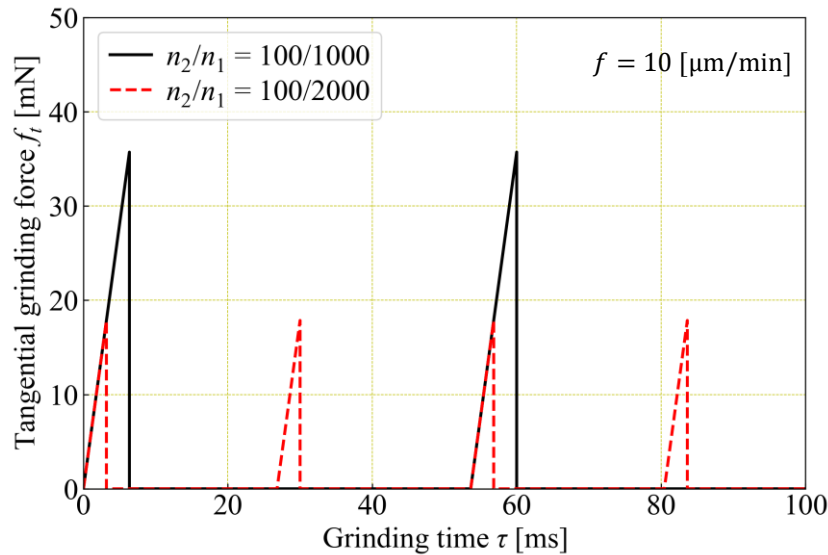

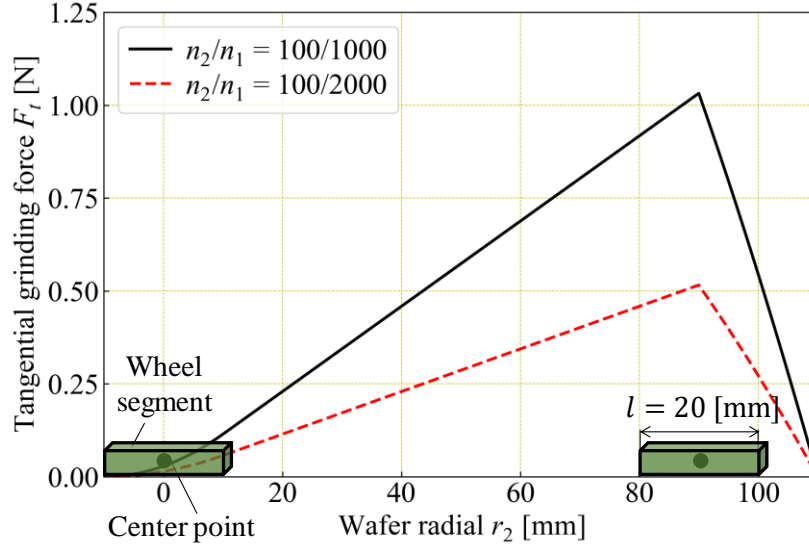Fig. 5.2 Grinding force variation on an individual abrasive

Fig. 5.3 Grinding force on a wheel segment

variation of the tangential grinding force on a wheel segment F_t is shown in Fig. 5.3. F_t gradually grows along the wafer radial distance r_2, and rapidly drops to zero when the wheel segment exits from the wafer fringe. This fact also suggests that the wheel rotational direction is important for wafer thinning process to ensure the wheel segment traveling from the wafer center toward its fringe. Otherwise, the wafer edge may encounter a sudden increase in grinding force and highly risk in edge cracking as published in [1, 2].

The total grinding force $\sum F_t$ generated on the entire wafer surface is calculated by integration of F_t within the range of $[0, R_2]$, and expressed in Eq. (5-4).

$$\sum F_t = \int_0^{R_2} f_t \cdot N_e w \mathrm{d}r_2 = \frac{Cp}{2} \cdot \frac{R_2^2}{R_1} \cdot \frac{n_2}{n_1} \Delta \qquad (5\text{-}4)$$

The consumed grinding power is then the product of $\sum F_t$ and the wheel rotational velocity and expressed as;

$$P = \sum F_t \cdot 2\pi R_1 n_1 = Cp \cdot \pi R_2^2 f \qquad (5\text{-}5)$$

The above equation well matches with the definition of grinding power which is the product of the specific energy Cp [J/mm^3] and the material removal rate ($MRR = \pi R_2^2 f$) [mm^3/s]. It can then be concluded that the consumed grinding power is determined once the wafer material and MRR are given. Both the total grinding force $\sum F_t$ (the solid line in Fig. 5.4) and the consumed grinding power P (the broken line in Fig. 5.4) are proportional to the
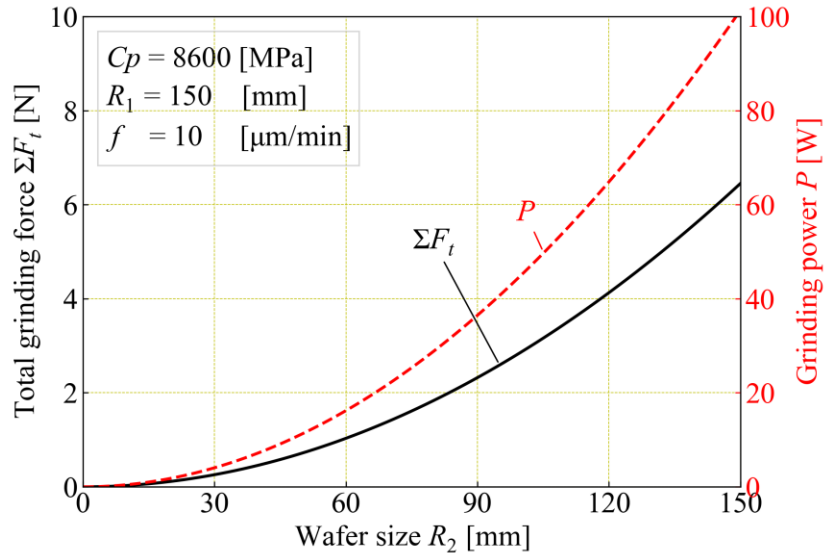
Fig. 5.4 Total grinding force and grinding power

square of the wafer size R_2. Hence, it is necessary to pay attention to the rigidity and the spindle power of the grinding machine when grinding large diameter wafers. Recent publications [3] and [4] by Kusuyama et al. who have designed and developed water hydrostatic rotary table and wheel spindle also share the same scope of interests for large diameter Si wafer grinding.

Back to the Fig. 4.1 (b), the grinding power consumed on the annulus positioned at $[r_2, r_2 + dr_2]$ is expressed as;

$$dP = 2\pi R_1 n_1 \cdot f_t \cdot N_e w dr_2 = 2\pi Cp \cdot f \cdot r_2 dr_2 \tag{5-6}$$

The corresponding surface area of the annulus is given as $2\pi r_2 \cdot dr_2$. The power density q (or, the energy consumed on a specific area of the wafer per unit time) is then resulted as;

$$q = \frac{dP}{2\pi r_2 \cdot dr_2 \cdot n_2} = Cp \cdot \frac{f}{n_2} = Cp \cdot \Delta \tag{5-7}$$

The power density is the source of the grinding heat and directly associated with the temperature rise in wafer grinding. It is found that the power density is consistent across the entire wafer, without depending on the radial distance r_2. The temperature distribution, however, may not be homogeneous due to the concentricity of round shape of the wafer. The details will be evaluated by use of FEM and reported in our subsequent study.

The grinding force f_n in the normal direction, on the other hand, is given in Eq. (5-8) by

Ref. [5] when assuming each individual abrasive is in a cone-shape with the vertex angle 2γ.

$$f_n = \frac{\pi}{2} \cdot Cp \cdot a_g \cdot \tan \gamma \tag{5-8}$$

Adding the friction force into the grinding force f_t, Eq. (5-2) is then updated as below;

$$f_t = Cp \cdot a_g + \frac{2}{\pi} \cdot \frac{\mu'}{\sin \gamma} f_n = \left(1 + \frac{\mu'}{\cos \gamma}\right) \frac{Cp}{R_1 w N_e} \frac{n_2}{n_1} \Delta \cdot r_2 \tag{5-9}$$

where the μ' is the friction coefficient. As the consequence, the grinding force F_t, $\sum F_t$, the grinding power P and the power density q addressed in Eq. (5-3) ~ (5-7) are all needed to be multiplied by a factor of $\left(1 + \frac{\mu'}{\cos \gamma}\right)$ in order to yield the effect of frication.

5.2 Wireless thermo/dynamo-meter development

Just as mentioned in chapter 3, the rotary in-feed dynamic, in which both grinding wheel and wafer rotate around their own axes, is different from that of the conventional reciprocating surface grinding. Therefore, the conventional wired measuring instruments are not applicable to rotary in-feed grinding because of the rotational motions of both the grinding wheel and wafer [6]. Thus, a wireless thermo/dynamo-meter has been developed for measuring the grinding force and temperature during the grinding process to understand the material removal mechanism [7-9].

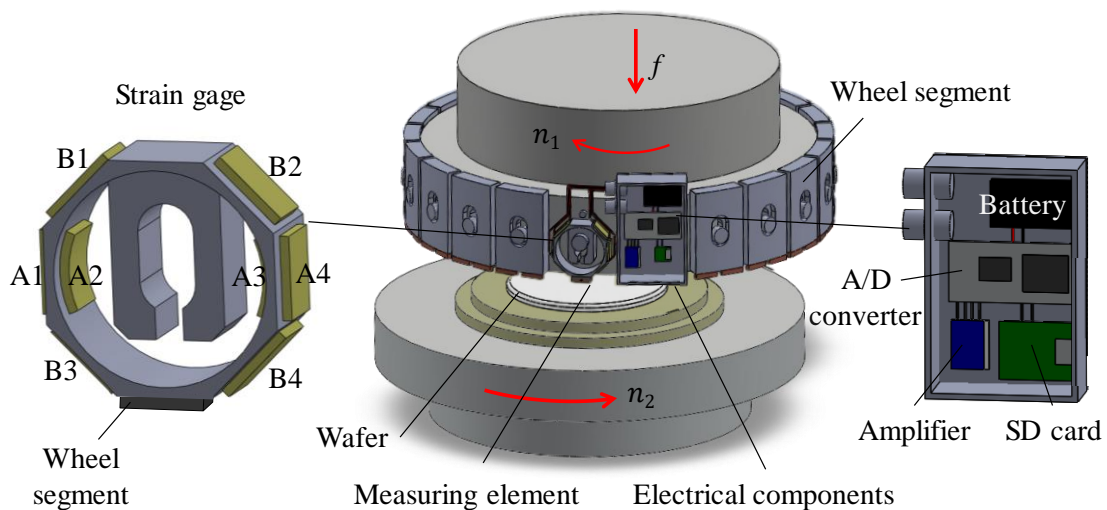The overview of the system of wireless thermo/dynamo-meter is illustrated in Fig. 5.5.

Fig. 5.5 Overview of wireless thermo/dynamo-meter

The wireless thermo/dynamo-meter consists of a wheel segment embedded with a K-type thermocouple, an aluminum octagonal ring with 2×4 strain gages, the Wheatstone bridge circuits, amplifiers, a 12-bit A/D converter, a Bluetooth transmitter and internal data storage. When the grinding wheel contacts the wafer, the thermocouple and strain gages output signals corresponding to the temperature and forces. These signals are amplified and then converted to digital signals by the A/D converter. The digitized signals can be either sent out by the Bluetooth transmitter or saved into the internal data storage. The detailed electrical diagram of wireless thermo/dynamo-meter is shown in Fig. 5.6, and the specifications are listed in Table 5.2.

Thermocouple leads are wrapped with aluminum foil and runs through a hole in the grinding wheel to reach the wheel working surface. There is no conduction between the thermocouple leads before grinding process. When the wheel made contact with the wafer, the thermocouple is bridged and conducted with the help of deformation flow in aluminum foil, to output a signal corresponding to the temperature in the contact zone.

The octagonal ring has two sets of four strain gages affixed, in which A1~A4 strain gages constitute Wheatstone bridge circuit to measure normal grinding force F_n while B1~B4 strain gages constitute Wheatstone bridge circuit to measure the tangential grinding force F_t. The
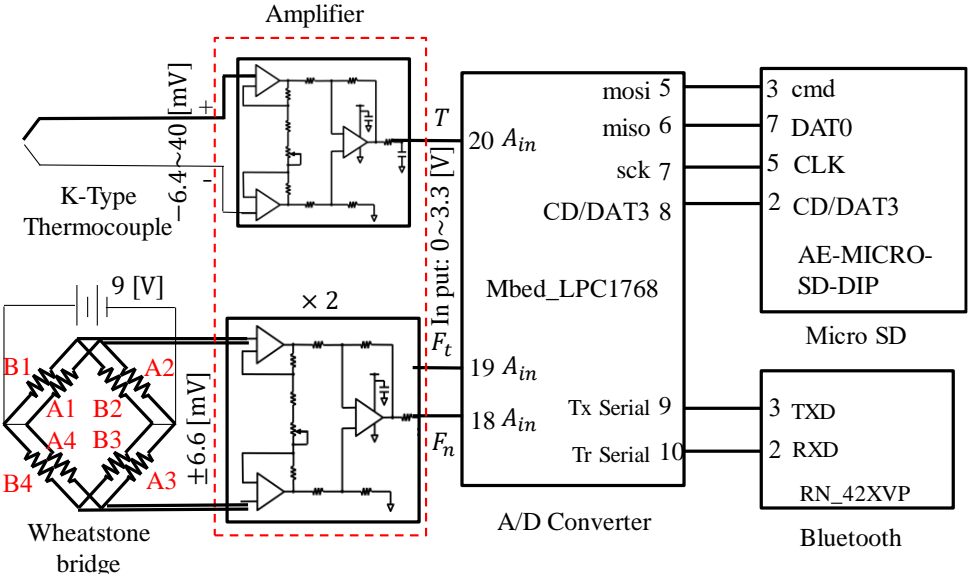

Fig. 5.6 Electrical diagram of wireless thermo/dynamo-meter

octagonal ring is deformed once it is involved in contact with the wafer. Two Wheatstone bridge circuits will then output signals corresponding to the force components F_t and F_n in the contact zone.

The wireless thermo/dynamo-meter was calibrated before measurements. Fig. 5.7 shows the calibration results. As shown in the left panel, calibration was performed from 30 [°C]

Table 5.2 Specifications of wireless thermo/dynamo-meter

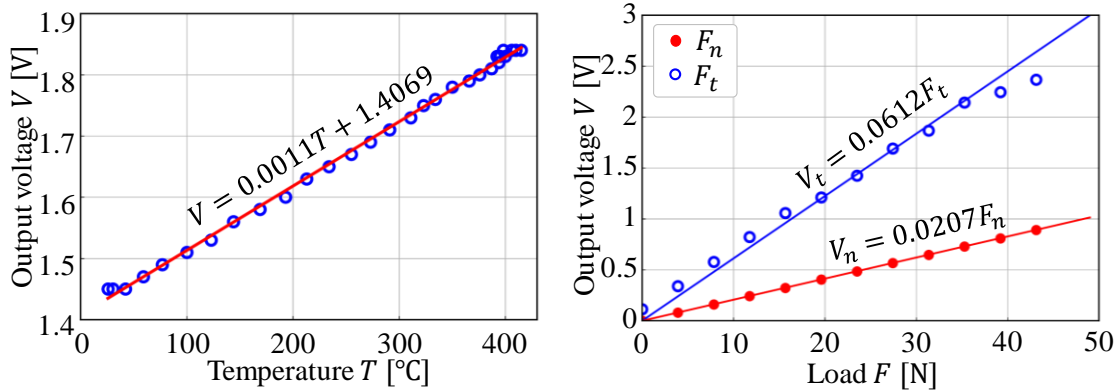|	Thermometer	Dynamometer
Measuring element	K-type thermocouple	Strain gage
Measurement range	0~1370 [°C]	−80~80 [N]
Resolution	1 [°C]	0.4 [N]
Channel count	1	2
Amplification factor	50	500
A/D converter	12 bit (LPC1768)	
Sampling frequency	40 [KHz] (≈ 13 [KHz/ch.])	
Data storage	Micro SD	

Fig. 5.7 Calibration of thermo/dynamo-meter [8]

to 550 [°C] for the thermometer. The response voltage is linearly proportional to the temperature in this range. The calibration results of dynamometer are shown in the right panel. Both response voltages are linearly proportional to the grinding force F_n and F_t. These calibration results guarantee the accuracy of wireless thermo/dynamo-meter.

5.3 Experiments and results

The experiments on grinding force evaluation was carried out on a vertical type rotary in-feed precision grinding machine (SGR-700) which is able to perform grinding process under constant in-feed rate. Fig. 5.8 shows its external view, on which a $\emptyset 200$ [mm] silicon wafer and diamond wheel (SD1000J100M) are mounted. The developed thermo/dynamo-meter was installed as one of wheel segments, as shown in the right panel of Fig. 5.8. During the grinding process, both grinding force and grinding temperature were measured simultaneously when the wireless thermo/dynamo-meter mounted segment was engaged into the wafer. The experiment conditions are given in Table 5.3.

Recorded in Fig. 5.9 are the grinding forces under conditions of (a) $n_1 = 160$ [min^{-1}] and (b) $n_1 = 320$ [min^{-1}], while $n_2 = 25$ [min^{-1}] and $f = 15$ [μm/min] are kept

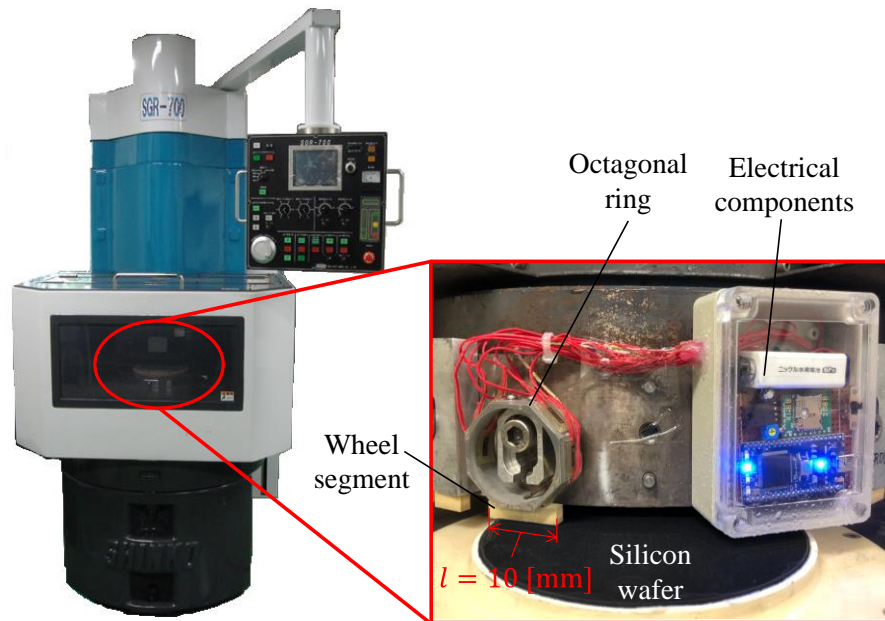Fig. 5.8 Vertical grinding machine and experiment setup

Table 5.3 Experiment conditions

|				
Wheel specifications	Grinding wheel	—	SD1000J100M	—
	Wheel size	$l \times w$	10×3	$[mm^2]$
	Number of segments	n	35	[pratical]
	Wheel radius	R_1	150	[mm]
Wafer specifications	Wafer	—	Si	—
	Specific energy	Cp	8600 [5]	[MPa]
	Wafer radius	R_2	100	[mm]
Grinding conditions	Wheel speed	n_1	160, 320	$[min^{-1}]$
	Wafer speed	n_2	25	$[min^{-1}]$
	In-feed rate	f	15	$[\mu m/min]$
	Total in-feed depth	—	60	$[\mu m]$
	Coolant	—	—	$[l/min]$

unchanged. The signals corresponding to the normal force component F_n and the tangential force component F_t appear periodically according to the frequency of wheel rotation $1/n_1$. When the wheel rotation speed is doubled from $n_1 = 160$ $[min^{-1}]$ to 320 $[min^{-1}]$, the grinding forces become halved. This result well matches with the prediction by Eq. (5-3).

The measured grinding forces were re-plotted as a function of the wafer redial distance r_2 for the further detailed study. The results were shown in Fig. 5.10, together with theoretical analysis by Eq. (5-3). It is found that the grinding forces on a wheel segment gradually grew along the wafer radial distance and rapidly dropped to zero when the wheel segment exited from the wafer periphery. The experimental results agree well with the theoretical results quantitively and qualitatively, strongly supports analysis in the previous section.

On the other hand, the actually measured grinding forces are still 20% ~ 40% larger than the theoretical prediction, especially in the wafer center. This might attribute to two reasons. One is the "size effect" which is closely related to the chip cross section a_g. According to

the Eq. (4-2), a_g is linearly proportional to the wafer radial distance r_2. In the wafer center, therefore, a_g is extremely small, results in a relatively larger Cp. The second reason comes from the spacing between the wheel segments, which leads to a fact the accumulated length wheel segment is always less than the circumferential length of the wheel $2\pi R_1$. The detail
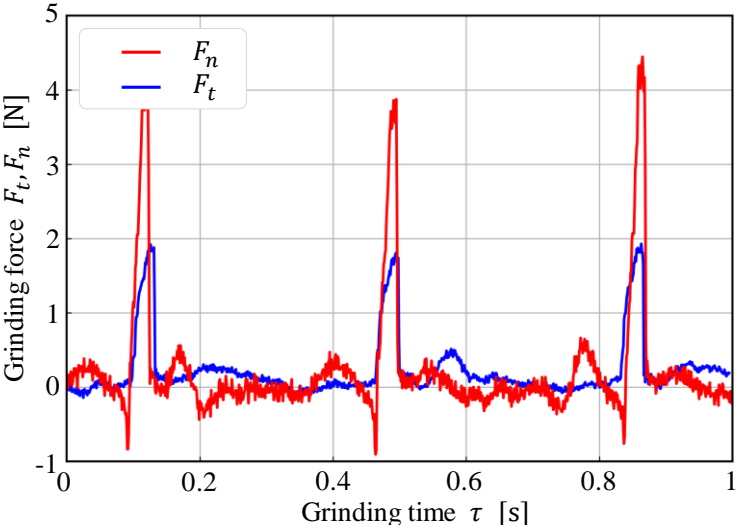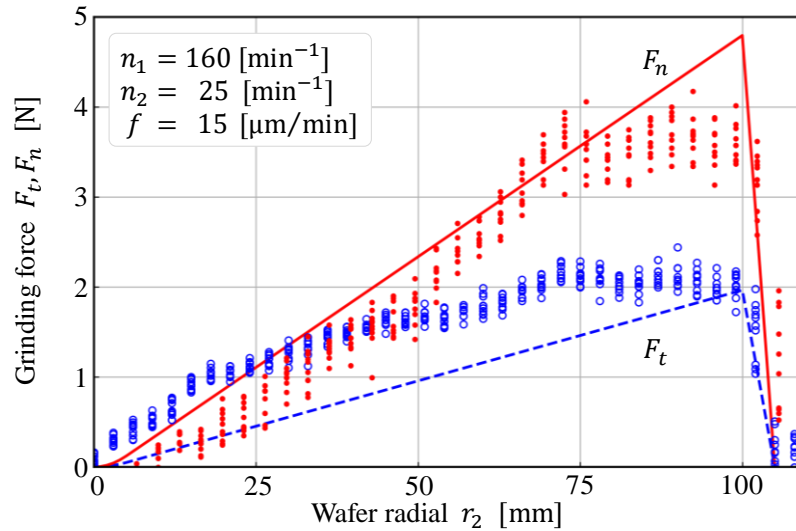

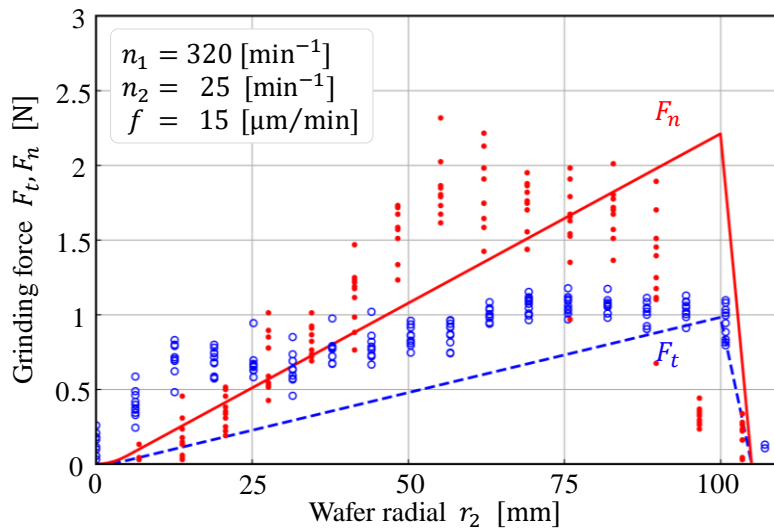(a) $n_1 = 160 \ [\text{min}^{-1}]$
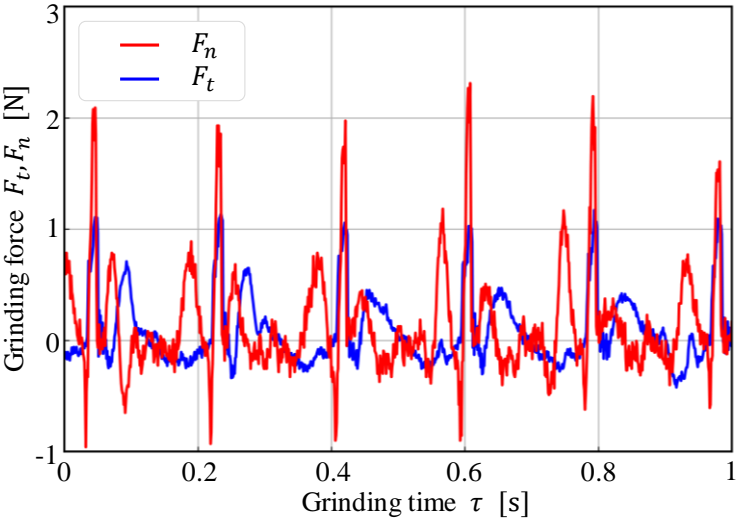
(b) $n_1 = 320 \ [\text{min}^{-1}]$

Fig. 5.9 Periodical appearance of the grinding forces under conditions of (a) $n_1 = 160$ $[\text{min}^{-1}]$ and (b) $n_1 = 320 \ [\text{min}^{-1}]$ [7]

will be evaluated in the subsequent discussion for the grinding power.

Recorded in Fig. 5.11 is the periodical appearance of the grinding temperature at $n_1 = 320$ [min^{-1}]. The results are also replotted in Fig. 5.12 as a function of the wafer radial distance r_2. It is found that the temperature variation in the contact zone was similar to that of the grinding force, which gradually grew along the wafer radial distance and rapidly

(a) $n_1 = 160$ [min^{-1}]

(b) $n_1 = 320$ [min^{-1}]

Fig. 5.10 Experimental results of grinding forces correlate to the wafer radial r_2 [7]

dropped at the wafer periphery. Due to the concentricity of round shape of the wafer, the temperature distribution across the wafer may not exactly follow this temperature profile. The details are now under evaluation by use of FEM and will be reported in our future study.

The above experimental results lead to a conclusion that our proposed grinding dynamics
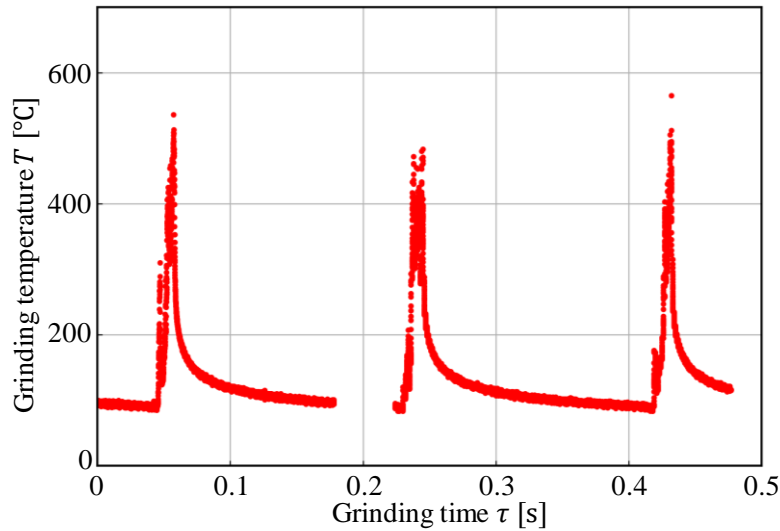

Fig.5.11 Periodical appearance of the grinding temperature under conditions of $n_1 = 320 \, [\text{min}^{-1}]$
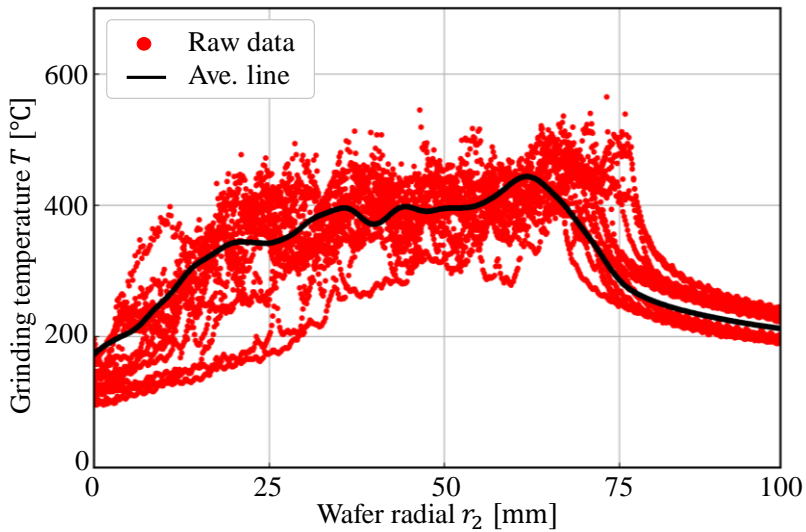

Fig. 5.12 Experimental result for grinding temperature

77

model is highly accurate in analyzing grinding force for rotary in-feed grinding and validate in optimizing grinding conditions for reduction in the subsurface damage.

5.4 Further discussion on dynamic behavior of grinding power

According to Eq. (5-5), the consumed grinding power is determinable once the wafer material and MRR are given, seems to be independent from other grinding conditions like n_1 and n_2. In this section, we will further discuss on the effects of abrasive wear through monitoring the consumed grinding power in actual grinding of two kinds of wafers: silicon and sapphire.

The experiment was carried out on a horizontal type rotary in-feed precision grinding machine (UPG-150), as shown in Fig. 5.13. During the grinding process, the power of wheel driving motor can be monitored and recorded by a data acquisition system. The detailed experiment conditions are listed in Table 5.4.

First, three sets of grinding experiments were performed on silicon wafer at different in-feed rate f. The grinding power are recorded as Fig. 5.14, where the consumed power is about 500 [W] during air-cut, rapidly increased as the wheel was engaged into the wafer.
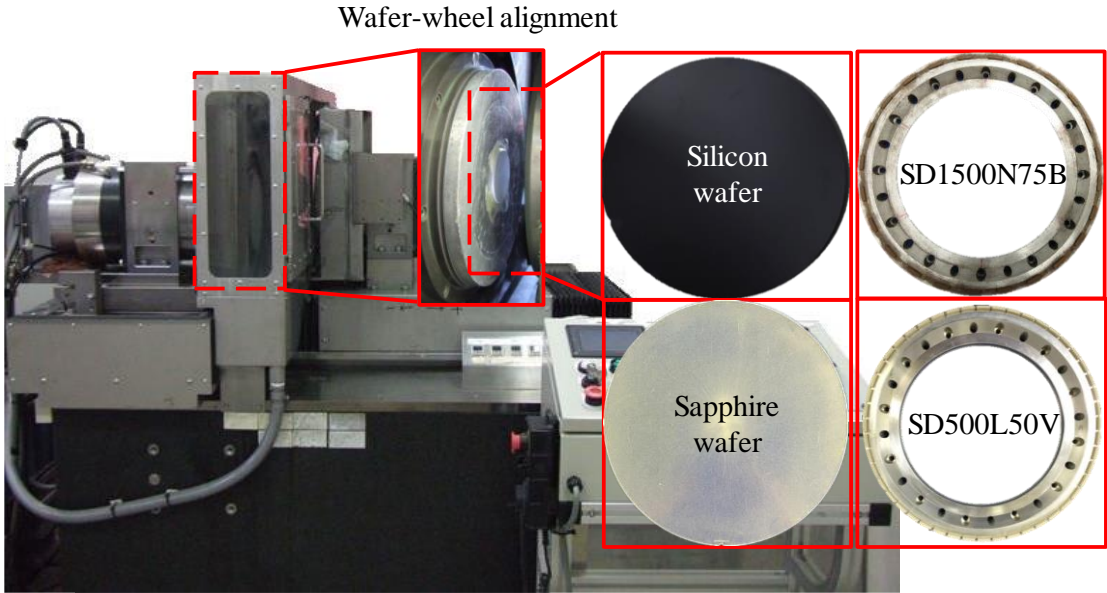

Fig. 5.13 Horizontal grinding machine and experimental setup

After the wheel fully in contact with the wafer, the power was then kept stable until the end of grinding process. Here, the increment in the grinding power from the air-cut is defined as the consumed power for grinding.

The consumed grinding is plot in Fig. 5.15 as a function of the in-feed rate f, together

Table 5.4 Experiment conditions

|			SD1500N75B	SD500L40V	
	Grinding wheel	—	SD1500N75B	SD500L40V	—
Wheel specifications	Number of segments	n	24	48	[pratical]
	Wheel size	$l \times w$	17×3	17×3	$[\text{mm}^2]$
	Wheel radius	R_1	150	150	[mm]
Wafer specifications	Wafer	—	Si	Sapphire	—
	Specific energy	Cp	8600	22500 [10]	[MPa]
	Wafer radius	R_2	100	75	[mm]
Grinding conditions	Wheel speed	n_1	2000	500	$[\text{min}^{-1}]$
	Wafer speed	n_2	25	100	$[\text{min}^{-1}]$
	In-feed rate	f	$10, 15, 20$	$10, 20, 30$	$[\mu\text{m/min}]$
	Total in-feed depth	—	40	40	$[\mu\text{m}]$
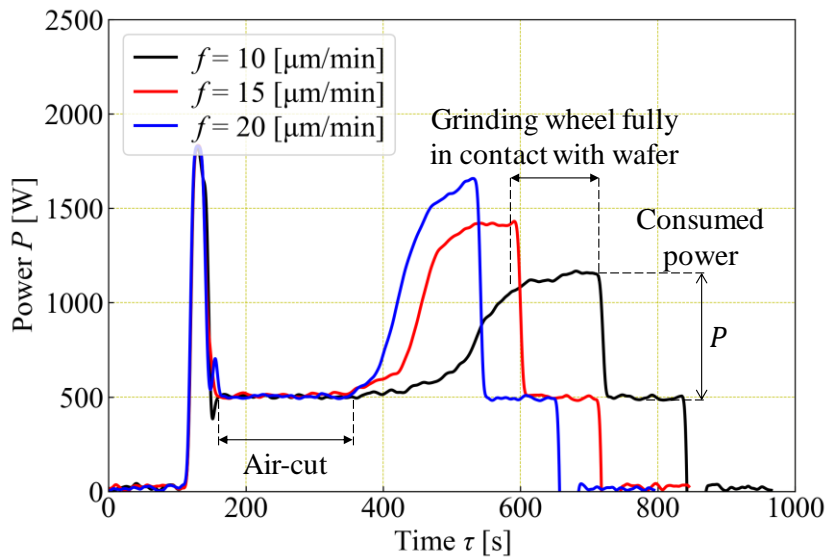
Fig. 5.14 Experimental results in silicon wafer grinding

with the result (broken line) calculated by Eq. (5-5). The consumed grinding power is found to be much larger than the theoretical predication. This is because Eq. (5-5) countered either the friction force mentioned in Eq. (5-9), nor the spacing between the wheel segments. Hence, we update the Eq. (5-5) to the modified grinding power as follows;

$$P_{\text{mod}} = \frac{1}{\zeta}\left(1 + \frac{\mu'}{\cos\gamma}\right) \sum F_t \cdot 2\pi R_1 n_1 = \frac{1}{\zeta}\left(1 + \frac{\mu'}{\cos\gamma}\right) Cp \cdot \pi R_2^2 f \tag{5-10}$$

where, $\zeta = nl/2\pi R_1$ is the ratio of accumulated length segments against the circumferential length of the wheel, takes a value less than 1. $\left(1 + \frac{\mu'}{\cos\gamma}\right)$ is the factor to yield the effect of frication force, takes a value larger than 1 as described in section 5.1.

Substituting $\zeta = 0.43$, $\mu' = 0.4$ [11], $\gamma = 82.5[°]$ [5] into Eq. (5-10), the modified grinding power P_{mod} is plotted using a solid line in Fig. 5.15, which is found to be much closer to the experimental results. Both experiments and theoretical results clearly show that the grinding consumed power is linearly proportional to the in-feed rate f. It must be pointed out that the vertex angle 2γ of abrasives in Eq. (5-10) remains unchanged for grinding at different in-feed rate, which means that the abrasives hardly wear in the silicon wafer grinding.

Now, we changed the wafer from the silicon to sapphire ($\emptyset 150$ [mm], C-plane), conduct the same in-feed grinding at the same horizontal grinding machine and investigate changes
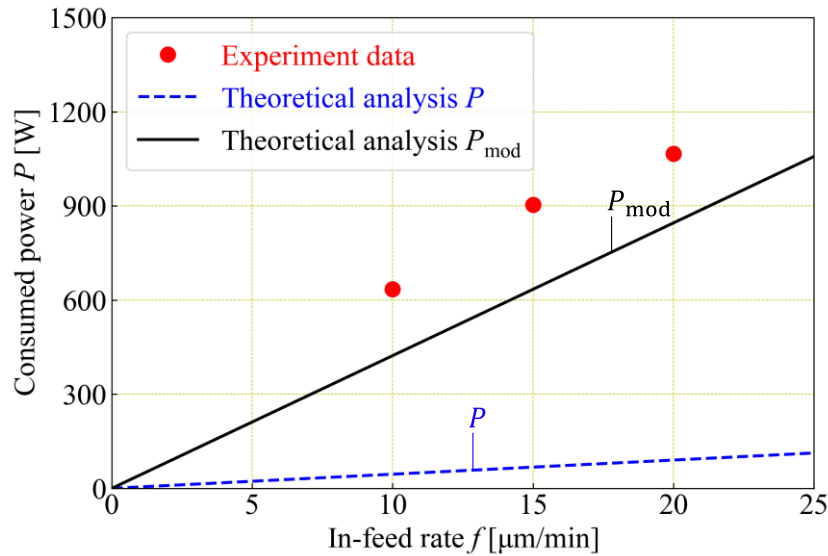

Fig 5.15 Grinding power for silicon wafer

in the consumed grinding power. The detailed grinding conditions are listed in the right column in Table 5.4. As compared in Table 5.5 [11-18], sapphire (α-Al$_2$O$_3$) crystal tends to be much harder and tougher than silicon crystal, thus, much more difficult to be ground. In other words, the abrasive wear is no longer negligible.

Fig. 5.16 is the consumed power recorded at three different in-feed rates varying from $10 \sim 30$ [μm/min], where the consumed power is about 200 [W] for the air cut at wheel rotational speed $n_1 = 500$ [min^{-1}]. Unlike grinding silicon wafer, the grinding power keeps increasing even after the wheel fully in contact with the wafer. For such circumstance, the abrasive wear must be considered when evaluating the grinding power. According to the

Table 5.5 The comparison of silicon and sapphire material properties

Notation	Si	Sapphire	Diamond	Unit
Friction coefficient	0.31~0.48	0.16~0.22	0.02~0.1	—
Density	2.33	3.97	3.51	[g/cm^2]
Vickers hardness	10.2	22.5	45	[GPa]
Young's modulus	193	470	1050	[GPa]
Fracture toughness	1.27~2.17	4.6	3.5	[MPa/$\sqrt{m}$]
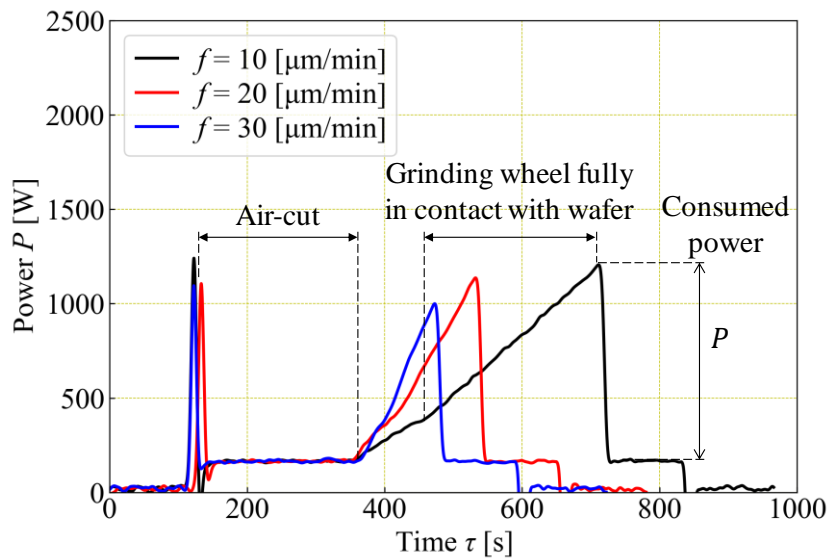
Fig. 5.16 Experimental results in sapphire wafer grinding
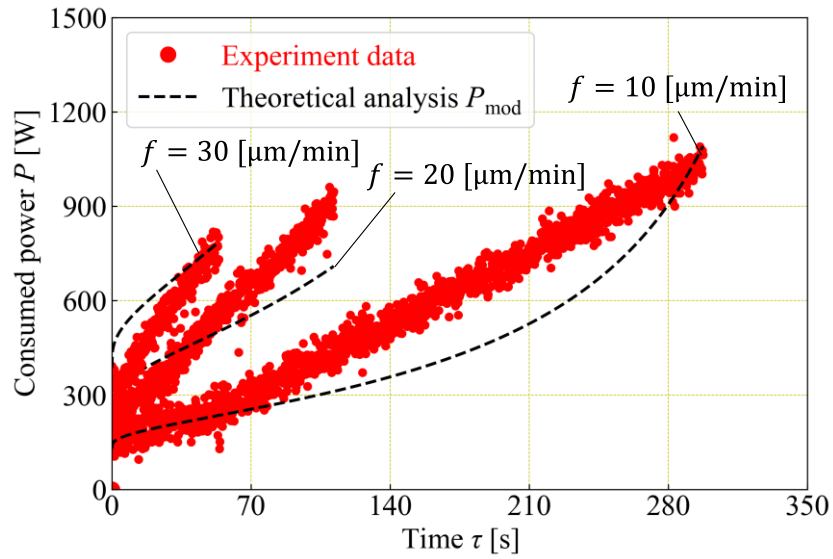
Fig. 5.17 The comparison of experimental and theoretical grinding power for sapphire wafer
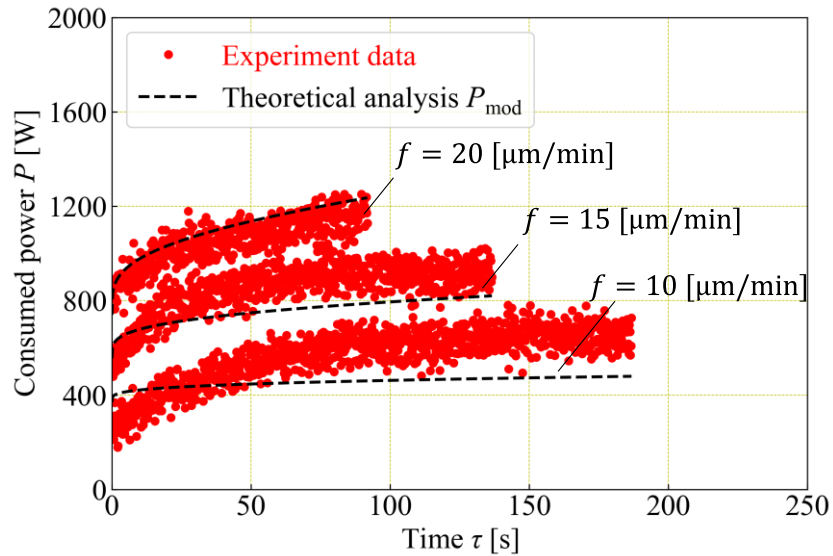

Fig. 5.18 The comparison of experimental and theoretical grinding power for silicon wafer

Taylor's tool life equation [19-21], the wear on vertex angle can be expressed as below;

$$\Delta \gamma = \chi \cdot MRR^{\psi} \cdot \tau^{\lambda} \qquad (5\text{-}11)$$

here, χ, ψ and λ are constants and depend on the abrasive property and the MRR $(= \pi R_2^2 f)$

is the material removal rate. Eq. (5-11) correlates the change in the vertex angle to the grinding time τ. The vertex angle at a specific grinding time is then given as $\gamma = \gamma_0 + \chi \cdot MRR^\psi \cdot \tau^\lambda$ where the γ_0 is the initial vertex angle of abrasive. Substituting Eq. (5-11) into Eq. (5-10) gives the modified grinding power as;

$$P_{\text{mod}} = \frac{1}{\zeta}\left[1 + \frac{\mu'}{\cos(\gamma_0 + \chi \cdot MRR^\psi \cdot \tau^\lambda)}\right] Cp \cdot \pi R_2^2 f \qquad (5\text{-}12)$$

Via the best fitting Eq. (5-12) to the experimental results shown in Fig. 5.17 and Fig. 5.18, we are able to solve three variables to be $\gamma_0 = 73[°], \chi = 8.5, \psi = 0.062$, and $\lambda = 0.2$ for the sapphire grinding, $\gamma_0 = 81[°], \chi = 0.01, \psi = 0.93$, and $\lambda = 0.2$ for the silicon grinding, respectively. Using this procedure, not only the abrasive wear along the grinding time but also the initial sharpness of the abrasive immediately after dressing can be appropriately evaluated. The values of χ, ψ and λ can be used as indicators to tell whether the current wheel specifications and grinding conditions fit the grinding process or not. For those relatively "easy-to-cut" materials like silicon, the wear on abrasive is negligible so that $\chi \approx 0$.

5.5 Summary

In this chapter, a detailed discussion concerning statics and dynamics in rotary in-feed grinding has been made based on theoretical analysis and experimental results. The obtained results could be summarized as below:

1) The grinding forces, grinding temperature and consumed grinding power were theoretically extended from the chip formation which is correlated to grinding conditions and wheel specifications.

2) The grinding force on a wheel segment is proportional to the segment length, gradually grows along the wafer radial distance, and rapidly drops to zero when the wheel segment exited from the wafer periphery.

3) The wheel rotational direction is important for wafer thinning process to ensure the wheel segment traveling from the wafer center toward its fringe. Otherwise, the wafer

may encounter a sudden increase in grinding force and highly risk in edge cracking.

4) The grinding power is determinable once the wafer material property and the material removal rate is given.

5) The power density is consistent across the entire wafer, without depending on the radial distance r_2.

6) The wireless thermo/dynamo-meter has been developed, which is able to measure the grinding forces and the grinding temperature simultaneously in rotary in-feed grinding.

7) Our proposed grinding dynamics model is highly accurate in analyzing grinding force for rotary in-feed grinding and validate in optimizing grinding conditions for reduction in the subsurface damage.

8) Using the modified grinding power model, not only the abrasive wear along the grinding time but also the initial sharpness of the abrasive immediately after dressing can be appropriately evaluated. The variables of χ and λ can be used as indicators to tell whether the current wheel specifications and grinding conditions fit the grinding process or not.

Reference

[1] Zhou L., Hosseini B.S., Tsuruga T., Shimizu J., Eda H., Kamiya S., Iwase H., Tashiro Y., (2007), Fabrication and evaluation for extremely thin Si wafer, International Journal of Abrasive Technology, Vol. 1, No. 1, pp. 94-105.

[2] Zhou L, Tian YB, Huang H, Sato H, Shimizu J., (2012), A study on the diamond grinding of ultra-thin silicon wafers, Proceedings of the Institution of Mechanical Engineers, Part B: Journal of Engineering Manufacture, Vol. 226, No. 1,pp. 66–75.

[3] Kusuyama J., Honda A., Kitajuma T., Okahata G., Yui A., Ito T., Slocum A.H., (2016), Development of rotary table grinding machine for large diameter Si wafers (1st report: Performance investigation of water hydrostatic rotary table), Transactions of the JSME, Vol. 82, No. 842, pp. transjsme.16-00190 (in Japanese).

[4] Kusuyama J., Honda A., Kitajuma T., Okahata G., Yui A., Ito T., Slocum A.H., (2017), Development of rotary table grinding machine for large diameter Si wafers (2nd report: Performance investigation of wheel spindle designed to govern infeed motion), Transactions of the JSME, Vol. 83, No. 852, pp. transjsme.17-00102 (in Japanese).

[5] Syoji K, (2004), Grinding Engineering, Yokendo Co., Ltd., pp. 69-96 (in Japanese).

[6] Couey JA, Marsh ER, Knapp BR, Ryan Vallance R., (2005), In-process force monitoring for precision grinding semiconductor silicon wafers, International Journal of Manufacturing Technology and Management, Vol. 7, No. 5/6 pp. 430–440.

[7] Ishibashi K, Tsukii Y, Ebina Y, Zhou L, Shimizu J, Yamamoto T, et al., (2019), Study on mechanism of rotary in-feed face grinding : Development of wireless dynamometer for rotary infeed face grinding, Journal of the Japan Society for Abrasive Technology, Vol. 63, No. 1, pp. 31–35 (in Japanese).

[8] Ishibashi K., Ichikawa Y., Lu W., Zhou L., Shimizu J., Onuki T., Ojima H., Yamamoto T., (2019), Development of wireless thermo/dynamo meter for rotary infeed grinding, The 22nd International Symposium on Advances in Abrasive Technology, A33.

[9] Fukuhara Y., Suzuki S., Sasahara H., (2018), Real-time grinding state discrimination strategy by use of monitor-embedded grinding wheels, Precision Engineering, Vol. 51, pp. 128-136.

[10] https://www.kyocera.co.jp/prdct/fc/product/pdf/tankessho.pdf

[11] Information on: https://www.azom.com/properties.aspx?ArticleID=599.

[12] Akamatsu K., Nakamura T., Arakawa N., (1989), Mirror Effect of Temperature Polishing of Si Wafers (1st Report) - Rise of Polisher Surface upon Stock Removal

Rate -, Journal of the Japan Society for Precision Engineering, Vol. 55, No. 6, pp. 1085-1090 (in Japanese).

[13] Morita N. and Yoshida Y., (1994), Brittle-Ductile transition and its control in machining of monocrystal silicon – Analysis of transition mechanism by sliding contact model –, Journal of the Ceramic Society of Japan, Vol. 102, No. 12, pp. 1137-1141 (in Japanese).

[14] Information on: https://www.guildoptics.com/sapphire-properties/sapphire-properties/.

[15] Enomoto Y., (1987), Shear deformation of brittle materials under sliding contact (The MgO and Sapphire pair as a main model material), Transactions of the Japan Society of Mechanical Engineers Series C, Vol. 53, No. 491, pp. 1519-1525 (in Japanese).

[16] Qiu W., Mizuno Y., Nakamura K., (2016), Tribological performance of ceramics in lubricated ultrasonic motors, Wear, Vol. 352-253, pp. 188-195.

[17] Information on: https://www.azom.com/properties.aspx?ArticleID=262.

[18] Gobet J., Volpe P.N., Dubois M.A., (2016), Friction coefficient of diamond under conditions compatible with microelectromechanical systems applications, Applied Physics Letters, Vol. 108, pp. 124103.

[19] Taylor F.W., (1907), On the art of cutting metals, The American Society of Mechanical Engineers, Vol. 28, pp. 31–58.

[20] Kitagawa T., Sakei Y., (1972), Influence of nose radius on tool life, Kitami Institute of Technology Repository, Vol. 3, No. 2, pp. 291-297 (in Japanese).

[21] Takeyama H., Murata R., (1964), Study on tool life in Turning Carbon steels, Journal of the Japan Society of Precision Engineering, Vol. 30, No. 2, pp.206-214 (in Japanese).

Chapter 6 Conclusion

As the most the promising process for wafer machining, rotary in-feed grinding has been widely applied in manufacturing of monocrystals, such as silicon, silicon carbide, sapphire, lithium tantalate and etc. In this thesis, I conducted a systematic and comprehensive study on its material removal mechanism from three aspects; 1) wafer profile generation and geometry control, 2) wafer topography generation and surface roughness and 3) grinding statics and dynamics assessments. The main conclusions obtained from each objective are summarized as follows:

1) Theoretical and experimental investigations on the wafer profile generation.

The motion and path of cutting edge in rotary in-feed grinding are kinematically analyzed in three-dimensions, successfully to address the behavior of each abrasive in generation of the wafer profile. The results mathematically reveal the effects of wheel specifications, grinding conditions and wheel/wafer configurations on the wafer geometry, particularly including the offset distance between the axes of wheel and wafer, the tilt angles of wafer axis and the diameter of the wheel. The effects of both cutting path density and machine stiffness on the wafer profile are also assessed. It is strongly recommended to use a grinding machine with a higher rigidity, a higher speed ratio, a finer abrasive to ensure the wafer geometry accuracy. The grinding dynamic model also provides a solution using tilt angle α, β to counterbalance the effect of machine stiffness and cutting path density on the wafer profile generation.

2) Theoretical and experimental investigations on the wafer topography generation.

The side removal area and chip cross section in rotary in-feed grinding has been analyzed to understand the chip formation and associated with grinding conditions and wheel specifications. The effective cutting edge density was estimated by taking into consideration of the distribution of abrasive protrusion in height-wise, which in turn precisely predicted the chip cross section and surface roughness. The surface roughness and its variation in a radial direction of the wafer were derived and discussed on varying grinding conditions. It is found

87

that the surface roughness becomes larger toward to the outer circumference of the wafer, but smaller as increasing in the speed ration of n_1/n_2.

3) Theoretical and experimental investigations on the grinding force and heat assessments.

The grinding forces, grinding temperature and consumed grinding power were theoretically extended from the chip formation which is correlated to grinding conditions and wheel specifications. The grinding force on a wheel segment is proportional to the segment length, gradually grows along the wafer radial distance, and rapidly drops to zero when the wheel segment exited from the wafer periphery. The grinding power is determinable once the wafer material property and the material removal rate is given. The power density is consistent across the entire wafer, without depending on the radial distance r_2. Meanwhile, the wireless thermo/dynamo-meter has been developed, which is able to measure the grinding forces and the grinding temperature simultaneously in rotary in-feed grinding. Our proposed grinding dynamics model is highly accurate in analyzing grinding force for rotary in-feed grinding and validate for optimizing grinding conditions for reduction in the subsurface damage. Further using the modified grinding power model, not only the abrasive wear along the grinding time but also the initial sharpness of the abrasive immediately after dressing can be appropriately evaluated.

Acknowledgement

This PhD thesis represents not only the work at the writing paper by typing on the keyboard, but it is also a milestone in more than half decade of work at Nano-engineering Laboratory of Ibaraki University where is a tremendous experience at academic research, involved in data analysis and precision manufacturing. My experience at Nano-engineering Laboratory (nLab) has been nothing short of amazing. Since I left my hometown Shenzhen in China and flew over 1785-mile distances on Jan 5th, 2013, I have been given unique opportunities to jump into my academic career in Japan. I starting as a postgraduate student in spring of 2014 at nLab of Ibaraki University. During experience over 5 years as a researcher, I have encountered at nLab from dozens of remarkable individuals who I wish to acknowledge.

First and foremost, look over my tough PhD journey, I wish to thank my advisor Professor Libo Zhou who has a passion for scientific research technically in data analysis, precision manufacturing, device development and innovation, and also is a prudent and rigorous mentor. It is a laurel and privilege for me to study under his supervision. Thanks for your responsiveness that give me an opportunity to work in the Nano-engineering Laboratory and study the high-end precision manufacturing, as well as for inspiring and guiding my way through this unpredictable PhD program. I have learned so much from my supervisors and sincerely grateful for you always giving me instruction no matter how busy life is. Hope to be able to work with you in the near future.

I am also profoundly grateful for the Prof. Jun Shimizu and Associate Prof. Teppei Onuki provide inestimable suggestions in time of my PhD program. I very much appreciate that they present the insightful comments on my research.

I am deeply indebted to Prof. Akinori Yui for his discerning comments on my PhD thesis and suggestions on my oral defense committee.

My heartfelt thanks to Associate Prof. Hirotaka Ojima and Mr. Takeyuki Yamamoto who give me the grateful help during these years. I am also deeply appreciative of the Japan Student Services Organization and Ibaraki University for generously offering me finance support in the past 5 years.

The work presented in this thesis has been critically assessed and approved by an outstanding committee to whom I am more than grateful: Mr. Kosuke Hasegawa, Mr. Ken Ishibashi, Mr. Yuki Ichikawa, Mr. Wangpiao Lin and Mr. Yutaro Ebina. I also would like to extend huge and warm thanks to them for assisting this project specially in regard to the measurements.

Finally, I would like to express my sincere gratitude to my family and friends who had a fundamental role in getting me through the PhD program successfully. At every stage in my life could not without their encouragement to make this achievement come true. I could not have imagined that this PhD journey without these amazing and lovely people mentioned above. Wish all the best wishes for you.

<div align="right">

Wentong Lu

2021.02.09

</div>